

UNCLASSIFIED

AD NUMBER

AD847275

LIMITATION CHANGES

TO:

Approved for public release; distribution is unlimited.

FROM:

Distribution authorized to U.S. Gov't. agencies and their contractors; Critical Technology; SEP 1968. Other requests shall be referred to Army Engineering Topographic Laboratory, Attn: ETL-GS, Fort Belvoir, VA 22060. This document contains export-controlled technical data.

AUTHORITY

usaetl ltr, 1 oct 1970

THIS PAGE IS UNCLASSIFIED

AD847275

THE FREQUENCY DEPENDENCE OF BACKSCATTER FROM ROUGH SURFACES

by

John W. Rouse, Jr.

CRES Technical Report No. 133-4

Sponsored by

**Advanced Research Projects Agency, Department of Defense,
Work Order No. 1079**

NASA Manned Spacecraft Center, Contract No. NAS 9-7175

National Science Foundation, Grant GK 1153

Monitored for Advanced Research Projects Agency

STATEMENT NO. UNCLASSIFIED

by

U.S. Army Engineering Topographic Laboratories

Geographic Information Systems Branch

Geographic System Division

Ft. Belvoir, Virginia

attn: ETL-GS

Contract No. DAAK02-68-C-0089

FEB 5 1969

CRES



THE UNIVERSITY OF KANSAS • CENTER FOR RESEARCH INC
ENGINEERING SCIENCE DIVISION • LAWRENCE, KANSAS

162

AD _____

THE FREQUENCY DEPENDENCE OF BACKSCATTER
FROM ROUGH SURFACES

by
John W. Rouse, Jr.

CRES Technical Report No. 133-4

September 1968

Sponsored by

Advanced Research Projects Agency, Department of Defense,
Work Order No. 1079

(Issued as a Special Interim Technical Report
under USAETL Contract DAAK02-68-C-0089)

NASA Manned Spacecraft Center, Contract No. NAS 9-7175

National Science Foundation, Grant GK 1153

Monitored for Advanced Research Projects Agency
by

U.S. Army Engineering Topographic Laboratories
Geographic Information Systems Branch
Geographic System Division
Ft. Belvoir, Virginia

BLANK PAGE

THE FREQUENCY DEPENDENCE OF BACKSCATTER FROM ROUGH SURFACES

An Experiment with Broad-spectrum Acoustic Waves

John Wilson Rouse, Jr., Ph. D.
University of Kansas

ABSTRACT

An experiment was performed with broad spectrum acoustic waves. Continuous broad-spectrum illumination was employed to examine the frequency dependence of backscatter from statistically rough surfaces. In addition, the operation of a panchromatic radar system was simulated.

The frequency dependence of backscatter was measured for an undulating surface appropriate for application of the Kirchhoff-Huygen's Principle, and for a very rough surface. The frequency dependence of the very rough surface was found to be in agreement with experimental results of other programs. The frequency dependence of the undulating surface was compared with the theory based on the Kirchhoff Method and was found to agree only in certain frequency regions. The results support the contention that the effective surface statistics are both frequency and angle dependent and that the dependences are interrelated. However, theoretical treatment was found that incorporated the correct dependences to predict the frequency dependence measured in this experiment.

In recent years the use of imaging radar systems for both military reconnaissance and geoscience investigations has expanded rapidly. Associated with this expanding demand has been the growing realization that the monochromatic nature of such system handicaps their utility, especially in military reconnaissance applications. This work is an experiment with a panchromatic system.

A system has been designed and constructed to implement a panchromatic technique using acoustic waves in water. The validity of using acoustic simulation of electromagnetic waves has been well established, and the advantages of doing so are clearly evident in this study. An evalua-

tion of the panchromatic system and verification of its utility are presented.

Images were obtained of object targets using monochromatic and swept-frequency illumination. The images clearly illustrate the effects of scintillation and/or glint on monochromatic images, and the elimination of the effect gained by using panchromatic illumination. The techniques proved extremely effective for averaging the lobes of complex reradiation patterns and, hence improving the target definition. This improvement was gained by employing less than $\pm 6\%$ frequency bandwidth. The results indicate that panchromatic systems should offer significant advantages over monochromatic systems in applications such as terrain imaging, altimetry, and tracking systems.

TABLE OF CONTENTS

<u>Chapter</u>	<u>Page</u>
ACKNOWLEDGEMENT	i
1. INTRODUCTION	1
2. BACKGROUND	5
2.1 Theoretical Analyses	6
2.2 Experimental Analyses	11
3. SYSTEM INSTRUMENTATION	21
3.1 System Function	21
3.2 System Description	21
3.3 Data Handling	30
3.4 System Limitations	31
3.5 System Imaging Capability	41
4. SCATTERING EXPERIMENT	41
4.1 Measurement Technique	41
4.2 Measurement Set-up and System Parameters	44
4.3 Description of the Rough Surfaces	48
4.4 Fading and Broad-Spectrum Illumination	55
4.5 Acoustic-Electromagnetic Analogy	61
5. RESULTS OF SCATTERING EXPERIMENT	64
5.1 Measurement Results of Fundamental Surface	64
5.2 Measurement Results of Sanded Surface	65
5.3 Comparison of Results with Experiments	80
5.4 Comparison of Results with Theory	84
6. IMAGING EXPERIMENT	93
6.1 Measurement Techniques	93
6.2 Targets	99
6.3 Analysis of Results	102
7. CONCLUSION	111
APPENDIX A GENERAL KIRCHHOFF METHOD	115
APPENDIX B GENERAL AUTOCORRELATION FUNCTIONS	133
BIBLIOGRAPHY	138

BLANK PAGE

LIST OF FIGURES

<u>Figure</u>	<u>Page</u>
Figure 2.1 Wavelength dependence of normalized radar cross section. (random scatter model). (after Spetner and Katz)	8
Figure 2.2 Wavelength dependence of normalized radar cross section (specular point model). (after Spetner and Katz)	8
Figure 2.3 Ohio State University Measurements (May, 1960).	13
Figure 2.4 Naval Research Laboratories Measurements - New Jersey Woods	14
Figure 2.5 NRL ground-based backscatter measurements (after Grant and Yapplee).	15
Figure 2.6 Waterways Experiment Station measurements.	18
Figure 2.7 Sandia Corp. Experiment results	19
Figure 2.8 Frequency dependence of radar return from the sea. (After Wiltse, Schlesinger, and Johnson)	20
Figure 3.1 Slow-sweep mode sampling technique	23
Figure 3.2 Block Diagram of System	22
Figure 3.3 Power amplifier termination	25
Figure 3.4	27
Figure 3.5 Single Transducer Test	34
Figure 3.6 Transducer pair measurement.	34
Figure 4.1 Signal return spectra recorded at three different receiver gain settings (a-c) and reference signal record (d)	46

<u>Figure</u>	<u>Page</u>
Figure 4.2 Ratio of average received power to transmitted power for different receiver gain settings to obtain composite.	47
Figure 4.4 Sample auto correlation functions for fundamental surface (Parkins 1965).	51
Figure 4.5 Sample probability distribution function for fundamental surface run #1 (Parkins 1965).	53
Figure 4.6 Sample probability distribution function for fundamental surface run #2 (Parkins 1965).	54
Figure 4.7 Positional fading probability distributions recorded at different receiver gain settings	57
Figure 4.8 Frequency fading probability distributions for four ranges of transmitted spectrum width.	58
Figure 4.9 Frequency fading probability distributions recorded at different positions	59
Figure 4.10 Positional fading probability distributions (a) and frequency-plus-positional fading probability distribution (b)	60
Figure 5.1 Frequency dependence of scattering coefficient, 0 Degree incidence angle, fundamental surface	66
Figure 5.2 Frequency dependence of scattering coefficient, 15 degree incidence angle, fundamental surface	67
Figure 5.3 Frequency dependence of scattering coefficient, 30 degree incidence angles, fundamental surface	68

<u>Figure</u>	<u>Page</u>
Figure 5.4 Frequency dependence of scattering coefficient, 45 degree incidence angle, fundamental surface	69
Figure 5.5 Frequency dependence of scattering coefficient, 60 degree incidence angle, fundamental surface	70
Figure 5.6 Frequency dependence of scattering coefficient, funda- mental surface	71
Figure 5.7 Variation of scattering coefficient with angle and frequency - fundamental surface	72
Figure 5.8 Frequency dependence of scattering coefficient, 0 degree indicence angle, fundamental surface (Covered with sand particles).	73
Figure 5.9 Frequency dependence of scattering coefficient, 15 degree incidence angle, fundamental surface (Covered with sand particles).	74
Figure 5.10 Frequency dependence of scattering coefficient, 30 degree incidence angle, fundamental surface (Covered with sand particles).	75
Figure 5.11 Frequency dependence of scattering coefficient, 45 degree incidence angle, fundamental surface (Covered with sand particles).	76
Figure 5.12 Frequency dependence of scattering coefficient, 60 degree incidence angle, fundamental surface (Covered with sand particles).	77

<u>Figure</u>	<u>Page</u>
Figure 5.13 Frequency dependence of scattering coefficient, fundamental surface (Covered with sand parti- cles.	78
Figure 5.14 Variation of scattering co- efficient with angle and frequency - sanded surface	79
Figure 5.15 Variation of slope for funda- mental surface data below 1.25 MHz.	81
Figure 5.16 Variation of slope for funda- mental surface data above 1.25 MHz.	81
Figure 5.17 Variation of slope for sanded surface data below 1.25 MHz	82
Figure 5.18 Variation of slope for sanded surface data above 1.25 MHz	82
Figure 5.19 Variation of slopes for natural surfaces (after Katz 1966)	83
Figure 5.20 Predicted frequency dependence, exponential autocorrelation function, $\tau/\sigma^2 = 35.317/\text{mm}$	87
Figure 5.21 Comparison of results with theory, $0^\circ, 15^\circ, 30^\circ, T/\sigma^2 = 29.660/\text{mm}$	88
Figure 5.22 Comparison of results with theory, $0^\circ, 15^\circ, 30^\circ, T/\sigma^2 = 20.967/\text{mm}$	89
Figure 5.23 Comparison of results with theory, using effective parameter, $T_e/\sigma^2 =$ $32.282 \lambda^{0.4}/\text{mm}$	91
Figure 6.1 Effect of frequency average on image of sphere targets	95
Figure 6.2 Positioning for acoustic imaging	97
Figure 6.3 Image recording of target return	97
Figure 6.4 8-element array	97

<u>Figure</u>	<u>Page</u>
Figure 6.5 Acoustic images of rubber sphere target103
Figure 6.6 Comparison of different frequency images of styrofoam sphere target105
Figure 6.7 Comparison of monochromatic and swept frequency images of styrofoam sphere target106
Figure 6.9 Image of major lobes of 8-element array for three monochromatic frequencies108
Figure 6.8 Effect of receiver gain variations on images of 8-element array at three monochromatic frequencies109
Figure 6.10 Effect of swept frequency on image of 8-element array110
 APPENDIX	
Figure A1115
Figure A2116
Figure A3120
 Figure B1 Predicted frequency dependence, varying slope method, fundamental surface137

LIST OF ILLUSTRATIONS

<u>Illustration</u>	<u>Page</u>
Illustration 3.1 Acoustic test facility	23
Illustration 3.2 View of acoustic test facility, Showing pulse-height analyzer (left).	29
Illustration 3.3 Single transducer gain	35
Illustration 3.4 Comparison of transmitting gain of 3.0 MHz (12°) transducer measured by single and two-transducer methods.	38
Illustration 3.5 Comparison of receiving gain of 3.0 MHz (6°) transducer measured by single and two-transducer methods.	39
Illustration 4.1 Acoustic tank arrangement used for recording of backscatter measurements	45
Illustration 4.2 Rubber target — fundamental surface	50
Illustration 4.3 Height gauge for measuring surface profile	50
Illustration 6.1 Acoustic test facility in imaging mode	94
Illustration 6.2 Linear motion carriage	98
Illustration 6.3 Imaging experiment object targets	100

LIST OF TABLES

<u>Table</u>	<u>Page</u>
Table B.1136

ACKNOWLEDGEMENT

It is inadequate to merely acknowledge the advice and direction of my advisor, Professor R. K. Moore, for without his support and understanding none of this would have been possible.

The financial support of the National Aeronautics and Space Administration under contract NAS 9-7175, the Department of Defense under contract DAAK02-68-C-0089, the National Science Foundation under grant GK 1153, the University of Kansas Computation Center, and the Center for Research, Inc., University of Kansas is gratefully acknowledged.

The efforts of the Remote Sensing Laboratory personnel, especially the secretaries; Mrs. Hird, Mrs. Opperman, and Mrs. Williams, is deeply appreciated. A special thank you is due my wife and son, for encouragement; my colleague, W. P. Waite, for consultation; and the four walls of CRES office no. 6, for companionship.

CHAPTER 1

INTRODUCTION

An experiment was performed with broad-spectrum acoustic waves. Continuous broad-spectrum illumination was employed to examine the frequency dependence of backscatter from statistically rough surfaces. In addition, the operation of a panchromatic radar system was simulated.

Theoretical investigations of electromagnetic and acoustic wave scattering have been conducted for many years (Beckmann and Spizzichino, 1963; Fung, 1966; Daniels, 1963; Parkins, 1966; Rayleigh, 1896; Rice, 1951; Bass, 1961; Ament, et al. 1959). Unfortunately the extent of experimental verification available for carefully measured surfaces is extremely limited (Earing and Smith, 1966). In this work comparison has been made between experimental and theoretical descriptions of the frequency dependence of backscatter from randomly rough surfaces.

Radar has been employed for many years in detection and ranging applications (Skolnik, 1962; Barton, 1964; Kerr, 1951). More recently, attempts have been made to utilize radar in geoscience applications that require much more information from the return signal than the existence and range of a target (Simonett, 1966; Pierson, et al., 1965; Moore, 1962; MacDonald, et al. 1968). Much of the desired information is believed to be obtainable by observing the angle, polarization, and frequency dependence of the illuminated surface (Rouse, et al., 1966; Ellermeier, et al., 1966; Peake, 1958). Some experimental radar systems have been used to measure angular dependence of backscatter (Ament, et al., 1959; Ohio State University, 1963). Likewise some limited applications of the polarization dependence have been employed (Moore and Dellwig, 1967; Katz and Spetner, 1960). Polychromatic (multi-frequency) systems are also not new (Grant and Yaplee, 1957). Unfortunately, most experimental results presently available are inadequate for use in verifying the theoretical predictions of these dependencies.

Polychromatic systems have been used for measurements of backscatter from object targets and terrain (Ohio State University, 1963; Ament,

et al., 1959; Grant and Yaplee, 1957; Wiltse, et al., 1957). However, their fundamental purposes have been to provide data for either determination of an appropriate design frequency for monochromatic radar systems used for particular applications or design information needed to determine necessary loop gain for particular monochromatic radar systems. The added information about the target characteristics intuitively believed to be present in the behavior of the return at different frequencies has not been extracted except to an extremely limited extent (Katz, 1966).

Radar systems incorporating some degree of frequency agility have been constructed for applications requiring anti-jamming capability or a reduction of the effects of fading or scintillation (Skolnik, 1962). These systems are not appropriately described as panchromatic since the frequency spread is usually very small, however, as is discussed in Chapter 4 and 6, the primary utility of panchromatic systems is the reduction of the effect of positional fading or scintillation. In general the frequency dependence of backscatter, at least from terrain targets, is sufficiently broad that the panchromatic system does not acquire frequency "signature" information as such (Katz, 1966).

Polychromatic and polypanchromatic (multi-panchromatic) systems should permit determining frequency "signatures" for object targets and terrain. The discussion of polychromatic radar experiments in Chapter 2 and the results of the acoustic experiment presented in Chapter 5 indicate the information expected from such systems.

The experiments were conducted using acoustic waves in water. It is important that the reader appreciate the analogy between acoustic waves and electromagnetic waves, and understands that the results obtained by this research are applicable to broad-spectrum radar systems. Specific cases where the electromagnetic wave and acoustic wave analogy is imperfect, such as scattering involving polarization effects, are pointed out in the text; however in general one can assume that the results obtained by measurements of acoustic wave returns from a target may just as well have been obtained by flying a radar over a particular terrain region having the same statistical properties.

Acoustic simulation of electromagnetic problems is well developed and documented. Even so its value as an analog computer is either not

understood or not appreciated by many radar engineers. An acoustic simulator makes it possible to perform in the laboratory many of the experiments normally reserved for flight testing, and to adjust parameters of the radar system in a highly controlled and repeatable manner. The simulator is advantageous because both distance and time are scaled by a factor containing the ratio of acoustic propagation in water to the electromagnetic propagation in air; a factor of 2×10^5 . Therefore, the radar problem is compressed to a size easily accommodated in a water tank, and the electronic system operates in the region near 1 MHz, rather than at microwavelengths. The flexibility is further enhanced by the option to scale distance in a non-linear manner. Hence, model experiments can be performed rapidly, repeatably, and at much lower cost than full scale radar experiments, and can provide results completely analogous to a large number of electromagnetic problems (Edison, 1961). A detailed discussion of the analogy and its validity is contained in Chapter 4.

The design and construction of a system providing broad-spectrum illumination occupied much of the effort in this program. Of particular concern is the behavior of the ultrasonic transducers used as the transmitter and receiver antennas. These devices are piezoelectric crystals which are resonant at particular discrete frequencies. Operation of these devices off-resonance, as is necessary in the broad-spectrum mode, poses special problems because of the sharp skirts of the transducer response and spurious resonances due to the transducer mountings. Overcoming these problems and defining the transducer effects on the data are significant achievements of the system effort. A thorough discussion of the transmission and reception methods, data processing, and calibration is necessary for interpretation of the experimental results and establishing their validity. This discussion is Chapter 3.

This research program is divided into two sections: 1) scattering experiment and 2) image experiment. The scattering experiment consisted of the measurement of backscattering from randomly rough surfaces; the determination of the frequency dependence predicted by scattering theory; and the comparison of experimental and theoretical results. Measurements of backscatter power from randomly rough surfaces were recorded for incidence angles

from vertical to 60 degrees across a frequency range of about 30:1 ($\lambda = 15\text{mm}$ to 0.5mm in water). A scattering surface was used that is gently undulating, with slopes large relative to the incident wavelengths. In addition measurements were made using the basic surface with small scatterers superimposed. The scattering experiment procedure and results are presented in Chapters 4 and 5 respectively.

The image experiment consisted of recording in image form (B-scan) the return from particular object and area extensive targets. The principal objective was to examine the effect of broad-spectrum illumination on the return. The monochromatic reradiation lobing structure of the targets was recorded and the "blending" characteristic of the broad-spectrum illumination was introduced and recorded. The image experiment results are presented in Chapter 6.

CHAPTER 2

BACKGROUND

The study of waves scattered from rough surfaces has been active for several decades because of the need of solutions to application problems. The problems of primary concern have been associated with radar, but the studies relate to line-of-sight radio communication, radar astronomy, and sonar among others (Beckmann and Spizzichino 1963). Although a general and exact solution to this problem is yet lacking, considerable progress has been made in developing various special methods that are valid in many situations.

In recent years radar has found utility as a sensor for geoscience investigations (Pierson, et al. 1965). Such applications require that the radar return provide information concerning the nature of the illuminated surface; for example, its topography, moisture content, surface cover, etc. The radar parameters of use in describing the desired terrain properties are incidence angle, polarization, and frequency (Rouse, et al. 1966). Therefore, at least for radar problems, expressions derived for average backscatter power must correctly incorporate the dependence of the amplitude on these parameters.

Many authors have treated the rough surface scattering problems by statistical methods (Fung, 1966). Expressions have been derived which attempt to incorporate the angle, polarization, and frequency dependence of the mean return power (Ohio State University, 1963). The Kirchhoff method is especially popular for this effort. The expressions obtained by this approach incorporate terms representing the statistics of the surface. Attempts have been made to obtain the statistical parameters of a surface, the moon surface for example, by fitting the equations to the backscatter data at different incidence angles and wavelengths (Evans, 1957; Hayre, 1964). It has been found that the values for the correlation distance and the standard deviation are different for different wavelength incident signals (Fung, 1965).

The conclusion has been that such parameters are wavelength dependent and that the incident wavelength acts as a "size filter".

2.1 Theoretical Analyses

A direct attempt to explain the wavelength dependence of scatter was made by Spetner and Katz (1960) using two different scattering models. Their results are presented below. Chapter 5 offers another explanation employing expressions obtained by the Kirchhoff method, which is summarized below and detailed in Appendix A.

2.1.1 Spetner and Katz Random Scatterer Model

The surface being considered is assumed to be composed of a large number of incoherent independent scatterers. The normalized radar cross section of the surface is the product of the density of scatterers per unit area and the average cross section of a single scatterer. For a sufficiently short incident wavelength the individual scatterers are distinct. However, as λ increases adjacent scatterers tend to merge and appear as a single scatterer, hence the effective density of scatterers decreases. This is expressed as

$$p_s = \begin{cases} p_0 & \lambda < \lambda_c \\ C_1 / \lambda^2 & \lambda > \lambda_c \end{cases} \quad (2.1)$$

where p_s = density of scatterers per unit area
 λ_c = wavelength above which scatterers become coherent
 λ = incident wavelength
 p_0, C_1 = constants

The average scatterer cross section for small wavelengths (but not necessarily as small as λ_c), is

$$\sigma_s = \rho \frac{4\pi A^2}{\lambda^2} \quad (2.2)$$

where ρ = power reflection coefficient
 A = effective area of the scatterer

For large wavelengths a Rayleigh-type scattering is assumed and the scattering cross section is

$$\sigma_r = \frac{C_2 V^2}{\lambda^4} \quad (2.3)$$

where V = volume of the scatterer
 C_2 = constant

The transition wavelength between the application of (2.2) and (2.3) is denoted λ_0 . The results of this approach are summarized in figure 2.1.

2.1.2 Spetner and Katz Specular Point Model

The surface being considered is reflecting, is of irregular shape but continuous, and has continuous derivatives. The contributions to the radar return are assumed to come predominantly from two sources: the energy which is reflected from large facets of the surface which are oriented perpendicular to the line-of-sight, and the energy which is scattered isotropically by the small scatterers.

The scattering coefficient is assumed to be of the form

$$\sigma^o = \rho_s \sigma_{is} + \rho_L \sigma_{iL} \quad (2.4)$$

where ρ_s, ρ_L = scatterer densities for small and large scatterers respectively.
 σ_{is}, σ_{iL} = scattering cross sections for small and large scatterers respectively.

The dependence of ρ_s on λ is the same as shown in equation (2.1). The function ρ_L expresses the density of facets oriented normal to the incident energy. Therefore it is related to the slope spectrum of the surface;

	$\lambda < \lambda_0$	$\lambda > \lambda_0$
$\lambda < \lambda_1$	$\sigma^\circ = \frac{4\pi p_0 \rho A^2}{\lambda^2}$	$\sigma^\circ = \frac{C_2 p_0 v^2}{\lambda^4}$
$\lambda > \lambda_1$	$\sigma^\circ = \frac{4\pi C_1 \rho A^2}{\lambda^4}$	$\sigma^\circ = \frac{C_1 C_2 v^2}{\lambda^6}$

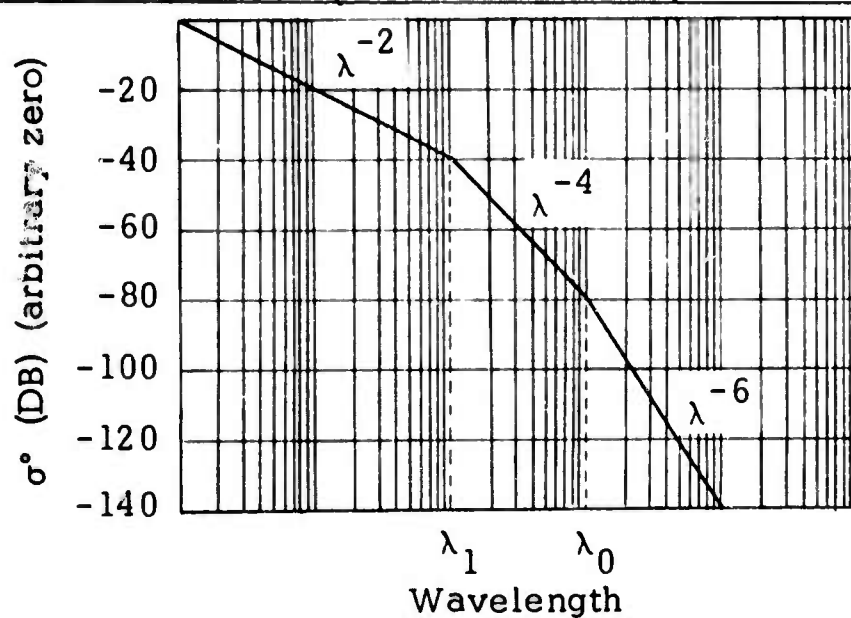


Figure 2.1 Wavelength dependence of normalized radar cross section. (random scatterer model). (after Spetner and Katz)

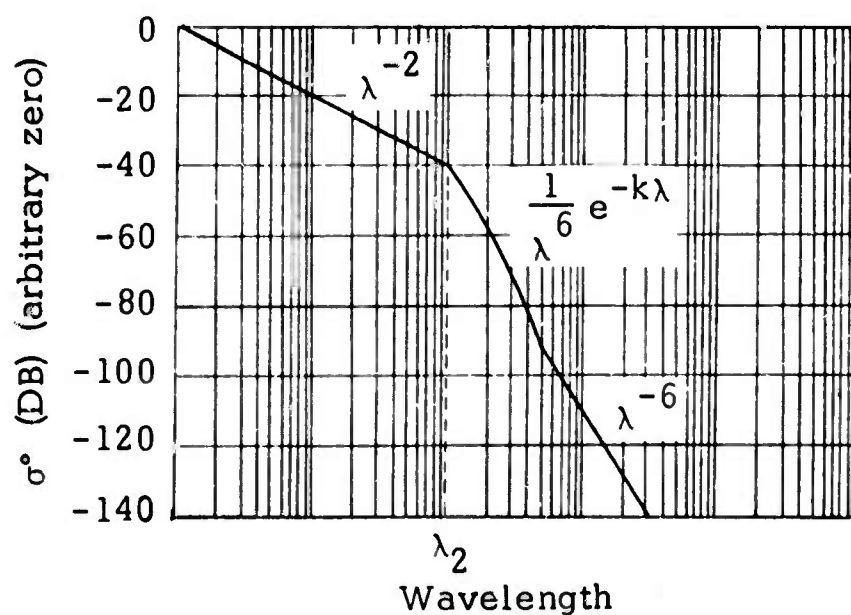


Figure 2.2 Wavelength dependence of normalized radar cross section (specular point model). (after Spetner and Katz)

in particular it is related to the slope variance, s^2 . Assuming a flat-slope spectrum with a cutoff at λ_2^{-1} , and considering the slope variance to be an effective parameter which is related to the measured variance, s_0^2 , by

$$s^2 = \begin{cases} s_0^2 & \lambda < \lambda_2 \\ s_0^2 \lambda_2 / \lambda & \lambda > \lambda_2 \end{cases} \quad (2.5)$$

then the density of large scatterers, at vertical incidence, is

$$p_L = \begin{cases} C_3 / \lambda_2^2 & \lambda < \lambda_2 \\ C_3 / \lambda^2 & \lambda > \lambda_2 \end{cases} \quad (2.6)$$

The scattering cross sections are

$$\sigma_{IL} = \rho \frac{4\pi A^2}{\lambda^2} \quad (\text{flat plate}) \quad (2.7)$$

and

$$\sigma_{IS} = \rho \frac{C_4 v^2}{\lambda^4} \quad (\text{Rayleigh scatter}) \quad (2.8)$$

The final result obtained for a surface composed as described and having a Gaussian slope distribution and flat-slope spectrum is

$$\sigma^0 = \begin{cases} \rho \frac{4\pi A^2 C_3}{\lambda^2 \lambda_2^2} e^{(-\cot^2 \theta / 2 s_0^2)} ; \lambda < \lambda_2 \\ \frac{C_3 C_4 v^2}{\lambda^6} e^{(-\cot^2 \theta) \lambda / 2 s_0^2 \lambda_2} + \frac{C_5}{\lambda^6} ; \lambda > \lambda_2 \end{cases} \quad (2.9)$$

The results for $C_5 < C_3 C_4$ are shown in figure 2.2.

The concepts advanced in this work are basically that various sub-ranges of scatter sizes effect the return differently at different wavelengths, thus the average return power expression must somehow accept the role of the changing range of dominant scatterers as the wavelength varies. This idea is elaborated in section 5.4 except that the Kirchhoff method is employed.

2.1.3 Kirchhoff Method

The method of physical optics, or Kirchhoff method, is based on the assumption that the incident field is "locally" reflected at a point on the irregular surface as if an infinite plane were tangent to the surface at that point. This assumption does not restrict the method to roughness of any particular size relative to the wavelength. However, its use is restricted to surfaces which are "locally flat" with respect to wavelength. Brekhovskikh's (1952) criterion for applicability is

$$4\pi\rho \cos \theta \gg \lambda$$

where ρ is the radius of curvature of the surface at the point of incidence and θ is the local angle of incidence between the incident energy vector and the unit normal to the surface at the point of incidence.

An expression for average backscatter power derived using the Kirchhoff method is (Beckmann and Spizzichino, 1963)

$$\langle E_2 E_2^* \rangle = 2\pi F_2 K \int_{\tau} J_0(\tau v_{xy}) \exp[-g(1-C(\tau))] \tau d\tau \quad (2.10)$$

where

$$g = 16\pi^2 (\sigma/\lambda)^2 \cos^2 \theta$$

$$v_{xy} = 16\pi^2 \lambda^{-2} \sin^2 \theta$$

λ = wavelength of incident radiation
 σ = standard deviation of surface heights
 θ = incidence angle of incident radiation

$C(r)$ = surface auto-correlation function
 r = distance on surface

Equation (2.10) is derived under the assumed conditions that the incident energy is a plane wave and the point of observation is in the Fraunhofer zone of diffraction. In addition the surface is assumed to be perfectly conducting, isotropic, and that no shadowing of one region by another exists. Further, multiple reflection and specular reflection components are negligible.

The frequency dependence of this equation is determined by the argument of the zero-order Bessel function and the constant g . The contribution of the Bessel function to the integral is decreasing with increases in either angle or frequency. The factor g decreases as the wavelength increases, however note that g is the multiplier in the exponent which operates on the quantity $[1 - C(\tau)]$. Depending on the value of σ/λ (assuming $g \gg 1$) the factor $C(\tau)$ cannot decrease far from unity before the contribution of the exponent term becomes negligible. Therefore the region of $C(\tau)$ that contributes is wavelength dependent (Fung and Moore, 1966). This fact is discussed in detail in section 5.4, and the Kirchhoff method is developed in Appendix A.

2.2 Experimental Analyses

Experiment programs designed to determine the frequency dependence of backscatter are few. The most significant programs are those conducted by Ohio State University (Taylor, 1959; Cosgriff, et al., 1960) and the Naval Research Laboratories (Ament, et al., 1958; Grant and Yapple, 1957); Sandia Corp. (Edison, et al, 1960) and Johns Hopkins University (Wiltse, et al., 1957). Additional measurements include those of the moon (Evans and Pettengill, 1963; Evans, 1962, 1965; Lynn, et al. 1964), and acoustic multi-frequency measurements of Fung and Leovaris (1968), and Chapman and Scott (1964). Studies presently underway by the Philco-Ford Corp. and several classified studies in progress offer more promise of defining the frequency dependence of backscatter than any previous programs. In addition, the University of Kansas is constructing a panchromatic system (Waite, 1968) for similar investigations.

2.2.1 Ohio State University Experiments

The OSU Antenna Laboratory has conducted extensive experimental programs using a three-frequency system mounted on a truck platform. The system antennas are elevated on an adjustable boom. The system operates at 10 GHz (X-band), 15.5 GHz (Ku-band), and 35 GHz (Ka-band).

The illuminated area is generally less than a meter in diameter and hence the experimental targets are small scale terrain features such as grass, concrete roads, etc. The measurement of average return power is obtained by moving the truck over the terrain during the recording period. The resulting data is reasonably accurate and repeatable, and the terrain type is well defined, although its statistical parameters are unknown. The experimental results are not readily adaptable to aircraft altitude measurements, due to the composite nature of terrain seen at these altitudes, but the results have proven very valuable as a guide to understanding scattering from "natural" terrain. Figure 2.3 shows examples of OSU data.

2.2.2 The Naval Research Laboratory Experiments

NRL operates a four-frequency radar system mounted in a WV-2 aircraft. At each frequency the radar is capable of transmitting either a horizontal or vertical linearly polarized signal and can receive both polarizations, hence the full polarization matrix is recorded. The system operates at 428 MHz (P-band), 1225 MHz (L-band), 4455 MHz (C-band), and 8910 MHz (X-band). The four antennas have azimuth beamwidths of 12° (P-band), 5.5° (L-band), and 5° (C- and X-band).

The system has been used extensively to record backscatter characteristics from a variety of targets, although the primary interest has been sea clutter. Because of the narrow elevation beamwidths of the C- and X-band antennas, the angular data are recorded on multiple passes, consequently terrain definition is gross, e.g. "New Jersey Woods". Figure 2.4 is an example of NRL aircraft-mounted system results.

NRL also operated a three frequency ground based system in a brief experiment (Grant and Yapplee, 1957). The system operated at wavelengths of 3.2 cm, 1.25 cm, and 8.6 mm. Measurements were recorded for various

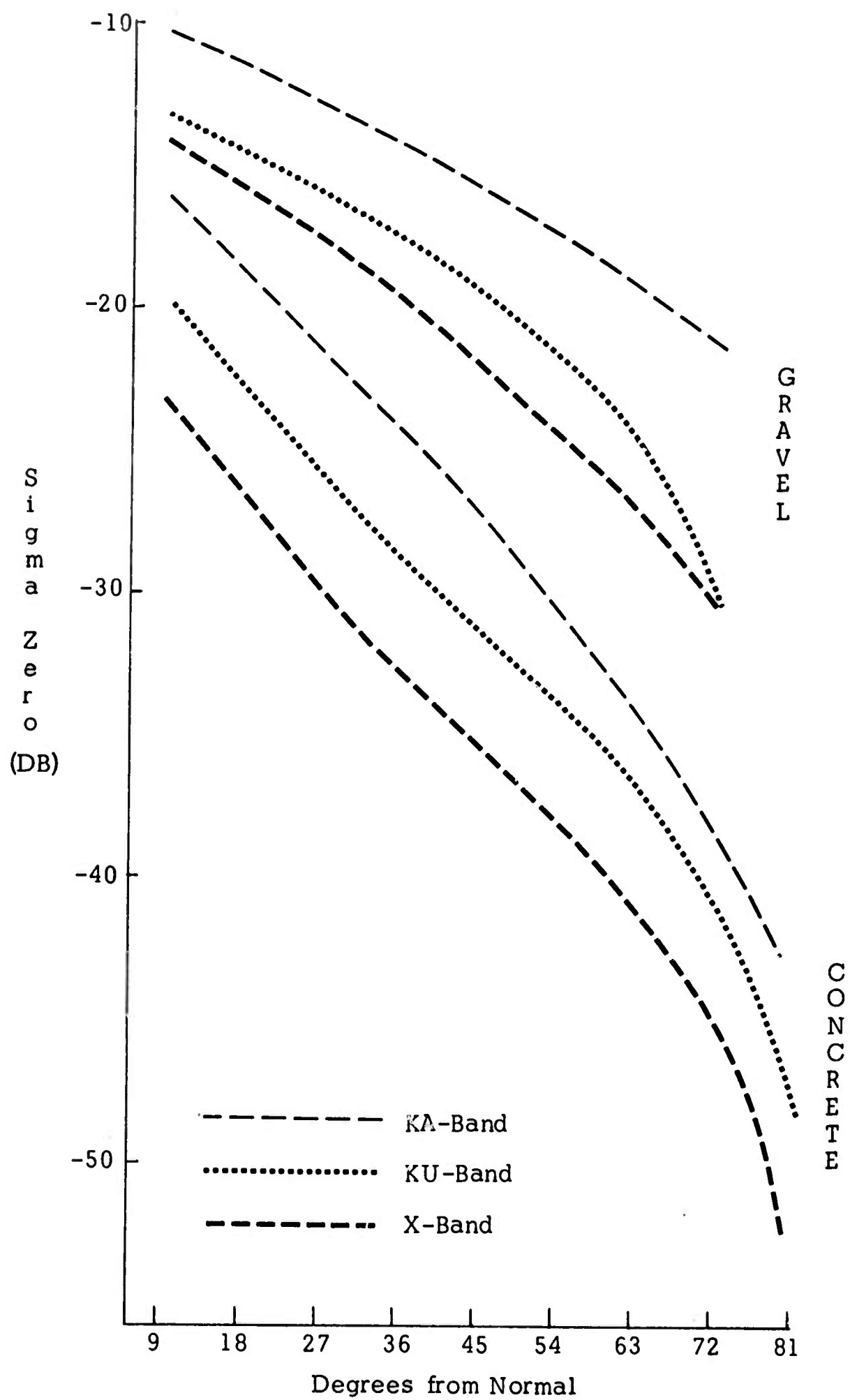


Figure 2.3 Ohio State University Measurements (May, 1960)

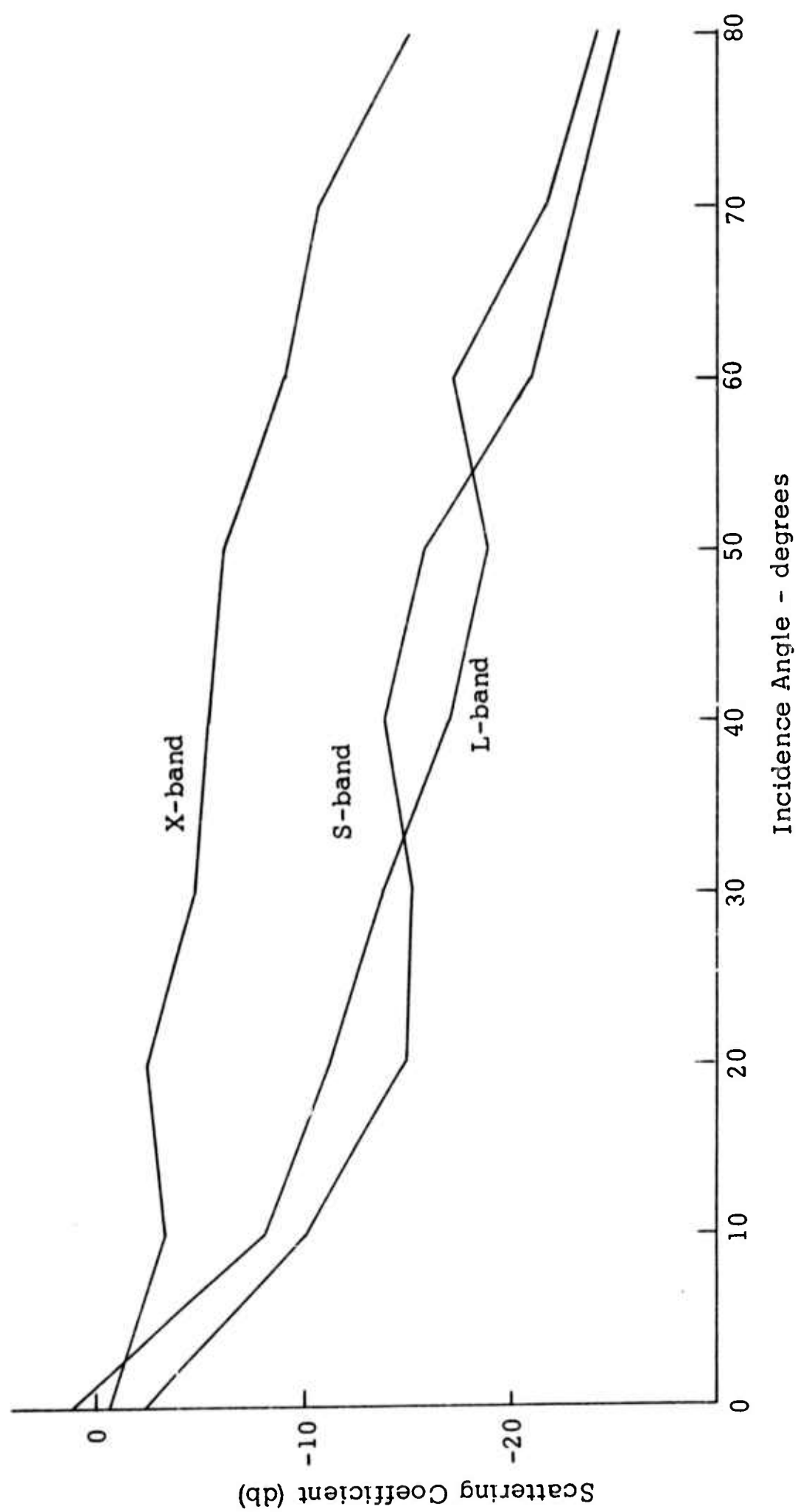


Figure 2.4 Naval Research Laboratories Measurements - New Jersey Woods

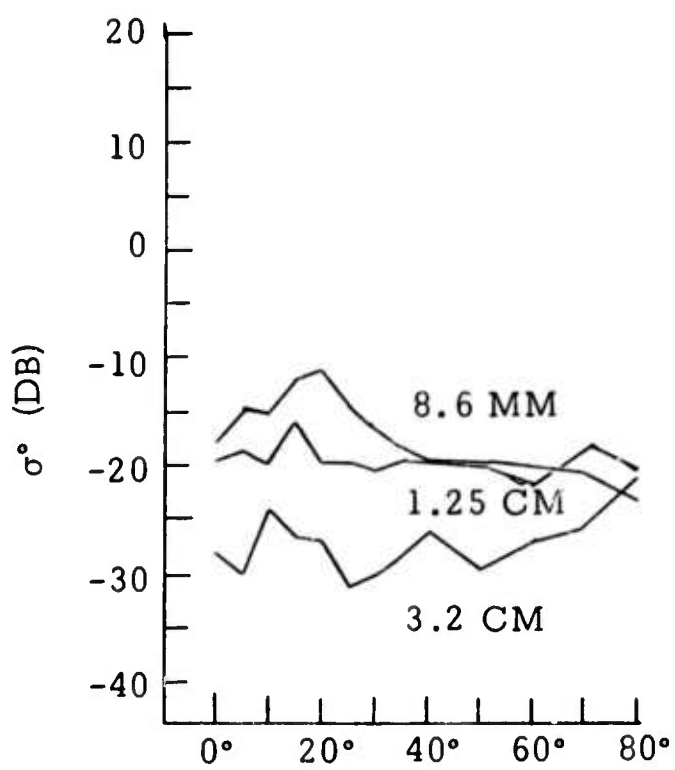


Figure (a) Terrain covered with tall dry weeds

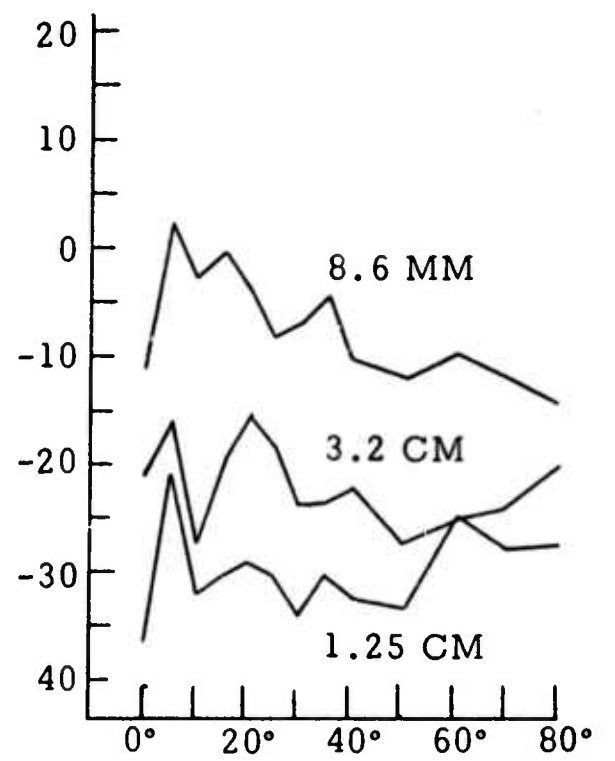


Figure (b) Nonhomogeneous terrain

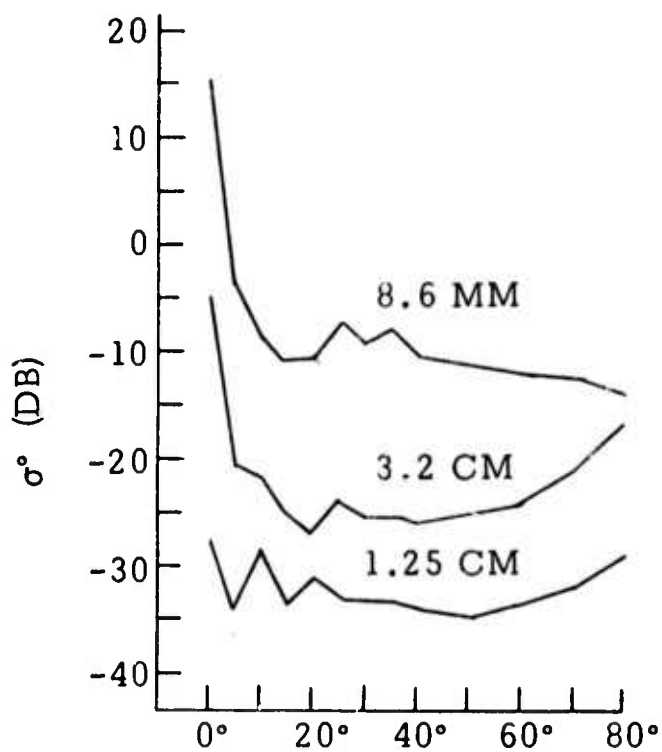


Figure (c) Wet terrain covered with tall green weeds or flags

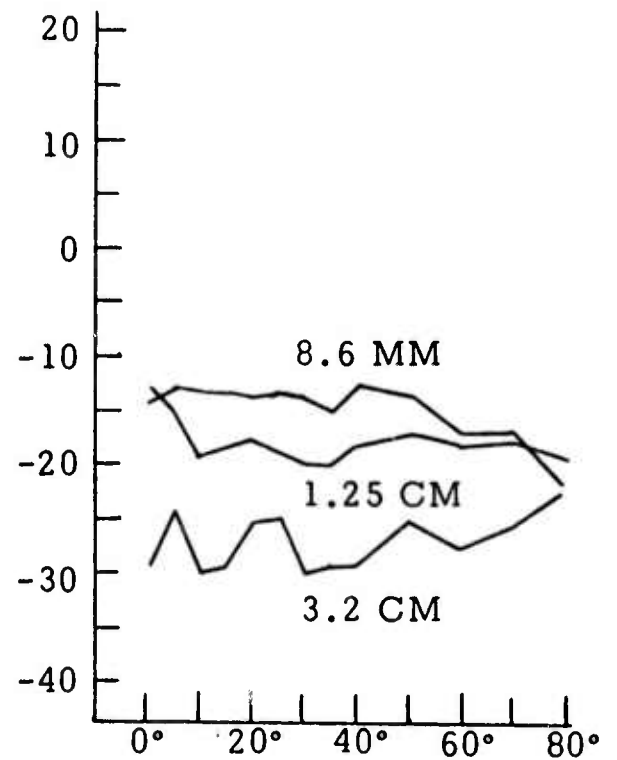


Figure (d) Tree-covered terrain.

Figure 2.5 NRL ground-based backscatter measurements (after Grant and Yapple)

terrain types including trees, marsh, dry weeds, etc. Figure 2.5 shows examples of measurements obtained.

2.2.3 Waterways Experiment Station Experiments

The U.S. Army Engineer WES operates a four-frequency radar system mounted on a 50-ft. radius arch. The antennas travel across the arch on a movable platform which allows viewing of the target sample over a 105 degree segment. The system frequencies are 297 MHz (P-band), 5879 MHz (C-band), 9375 MHz (X-band), and 35,543 MHz (Ka-band). The targets consist of specially prepared samples, usually soil, placed at the center point of the arch such that the range from the antennas to the target is constant for all angles of incidence. WES has facilities for controlled drying of the samples and much of their work has been devoted to determination of the effect of moisture content on radar return. In addition they have dealt extensively with penetration measurements.

Figure 2.6 shows plots of WES data obtained from a wheat sample at two stages of growth.

2.2.4 Sandia Corporation Experiments

These experiments were conducted using a two-frequency (415 MHz and 3800 MHz) narrow-pulse airborne radar system (Edison, et al., 1960). Measurements were recorded at altitudes of 2000 to 12000 feet over different target areas. The backscatter measurements were restricted to near-vertical incidence (less than 30° from the nadir), but the targets are reasonably well documented. The objective of the program was to provide data for the altimeter designer. Examples of the Sandia results are shown in Figure 2.7.

2.2.5 Johns Hopkins University Experiments

This program consisted of backscatter measurements from the sea using multi-frequency radar system mounted on the bow of a ship (Wiltse, et al., 1957). The system operated at 9.6, 15, 24, 26, 35, 38, and 48.7 GHz. Most of the data are for 9.6, 24 and 35 GHz and incidence angles of

0° , 10° , 20° , 30° , 45° , 60° , and 75° . Figure 2.8 shows plots of the scattering coefficient as a function of frequency for five incidence angles. Note that the scattering coefficient varies as $\lambda^{+3.5}$ for $\Theta = 60^\circ$ and λ^{+5} for $\Theta = 45^\circ$ in the region between 24 and 35 GHz. This slope exceeds that of the data compiled by Katz (see Section 5.3) which shows a maximum of λ^{+2} variation, also for sea return. The shape of the frequency dependence curves are similar to the results obtained from the fundamental surface measured in this program (see Section 5.1) which showed a maximum of $\lambda^{+3.7}$.

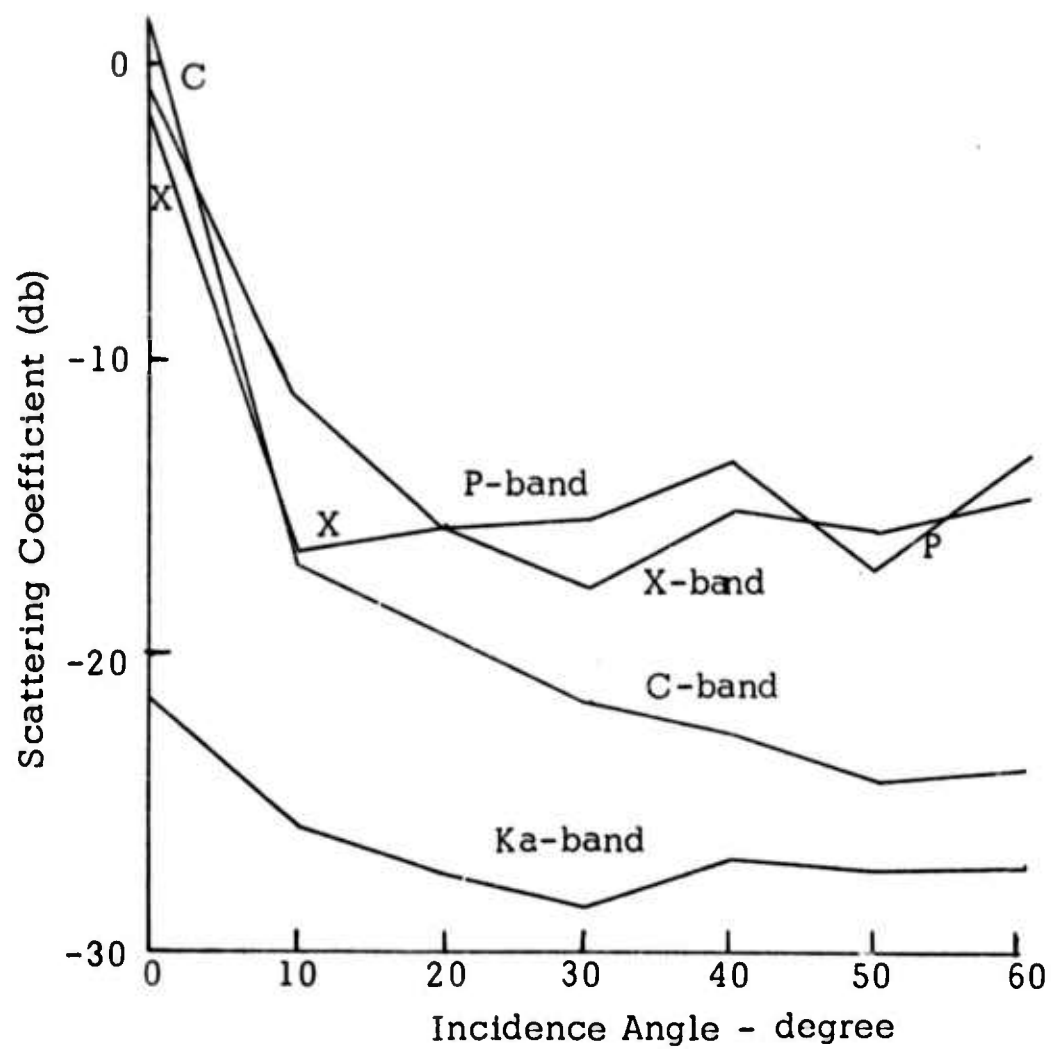


Figure (a) Wheat Sample - 3 1/2 in. height

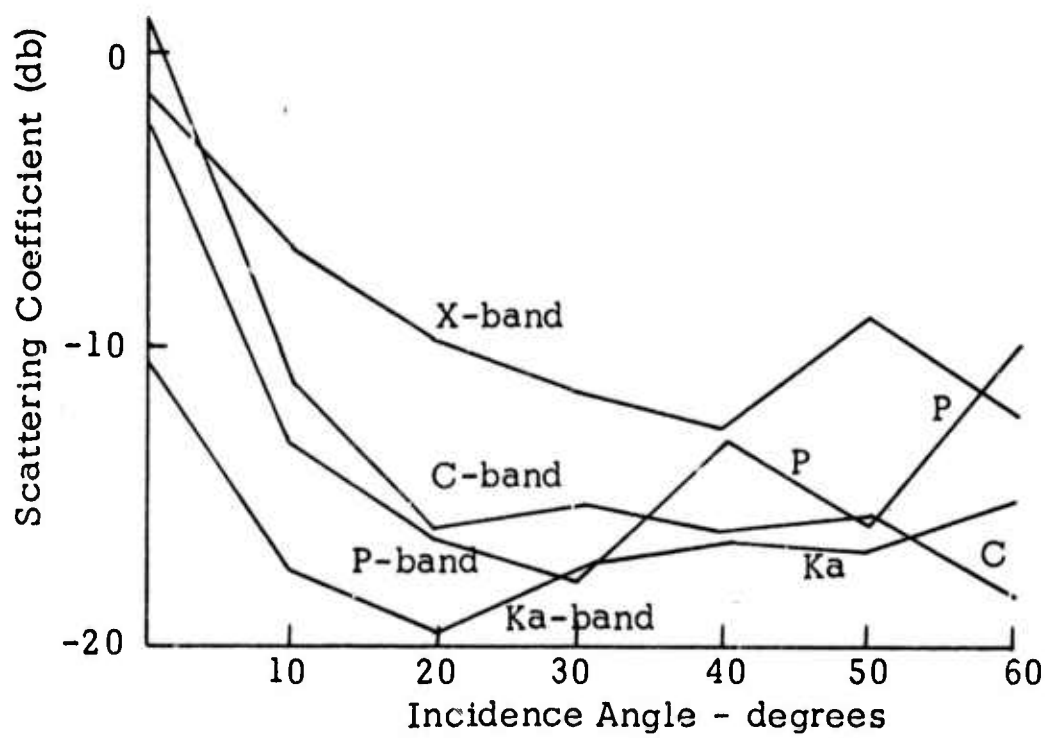
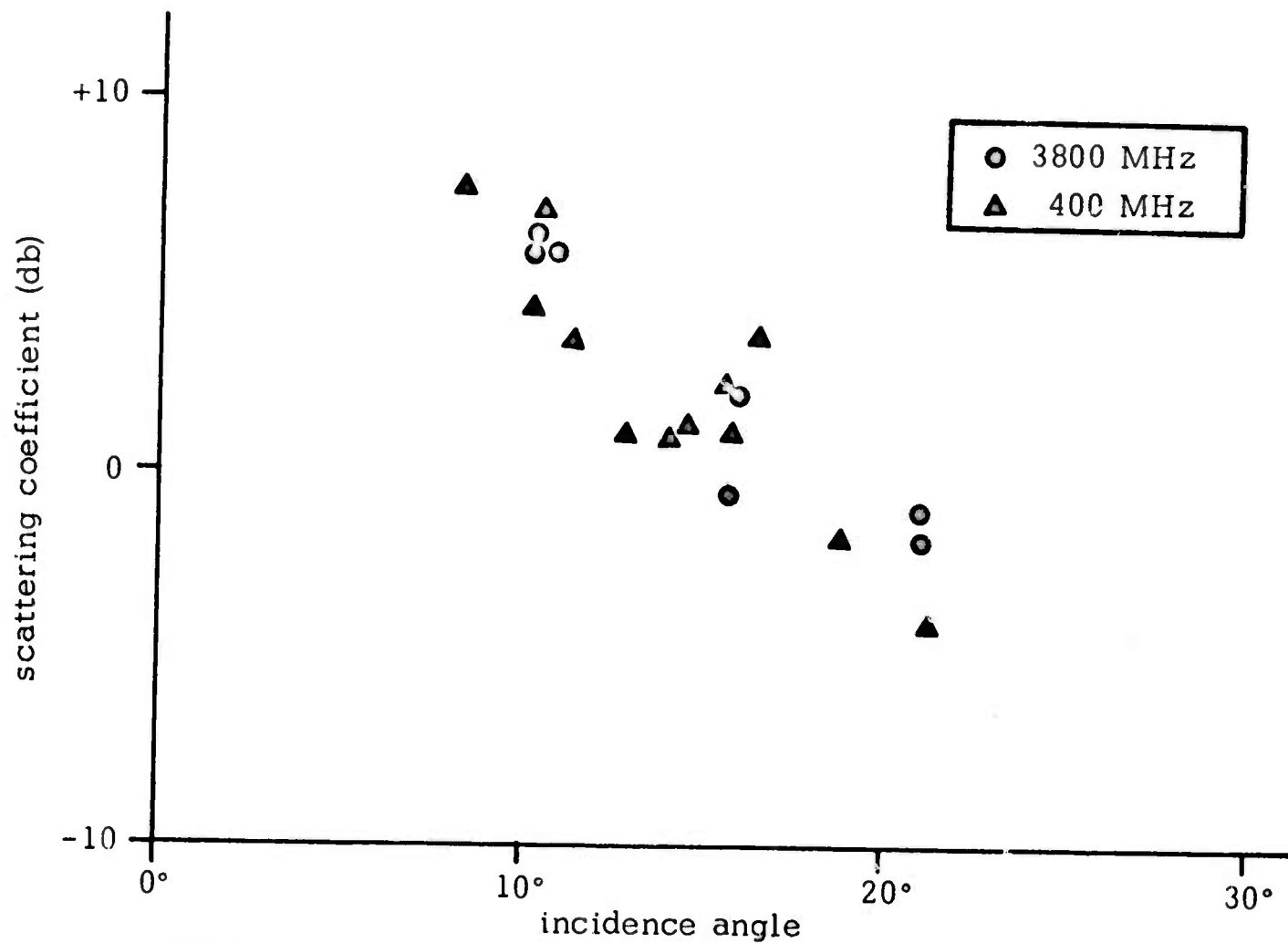
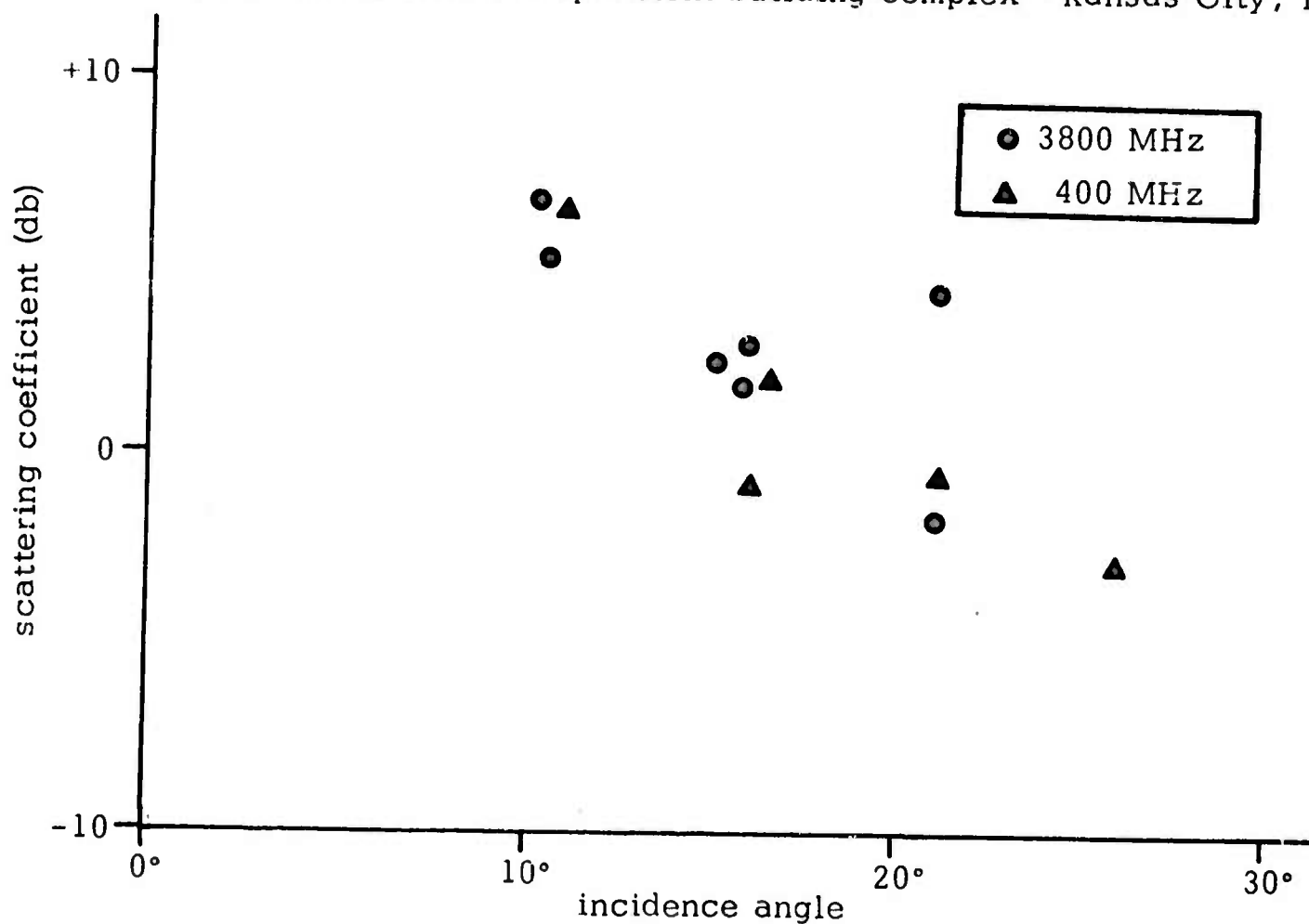


Figure (b) Wheat sample - 14 in. height

Figure 2.6 Waterways Experiment Station measurements



(a) Radar return from apartment building complex - Kansas City, Mo.



(b) Radar return from farmland - Sioux City, Iowa

Figure 2.7 Sandia Corp. Experiment Results

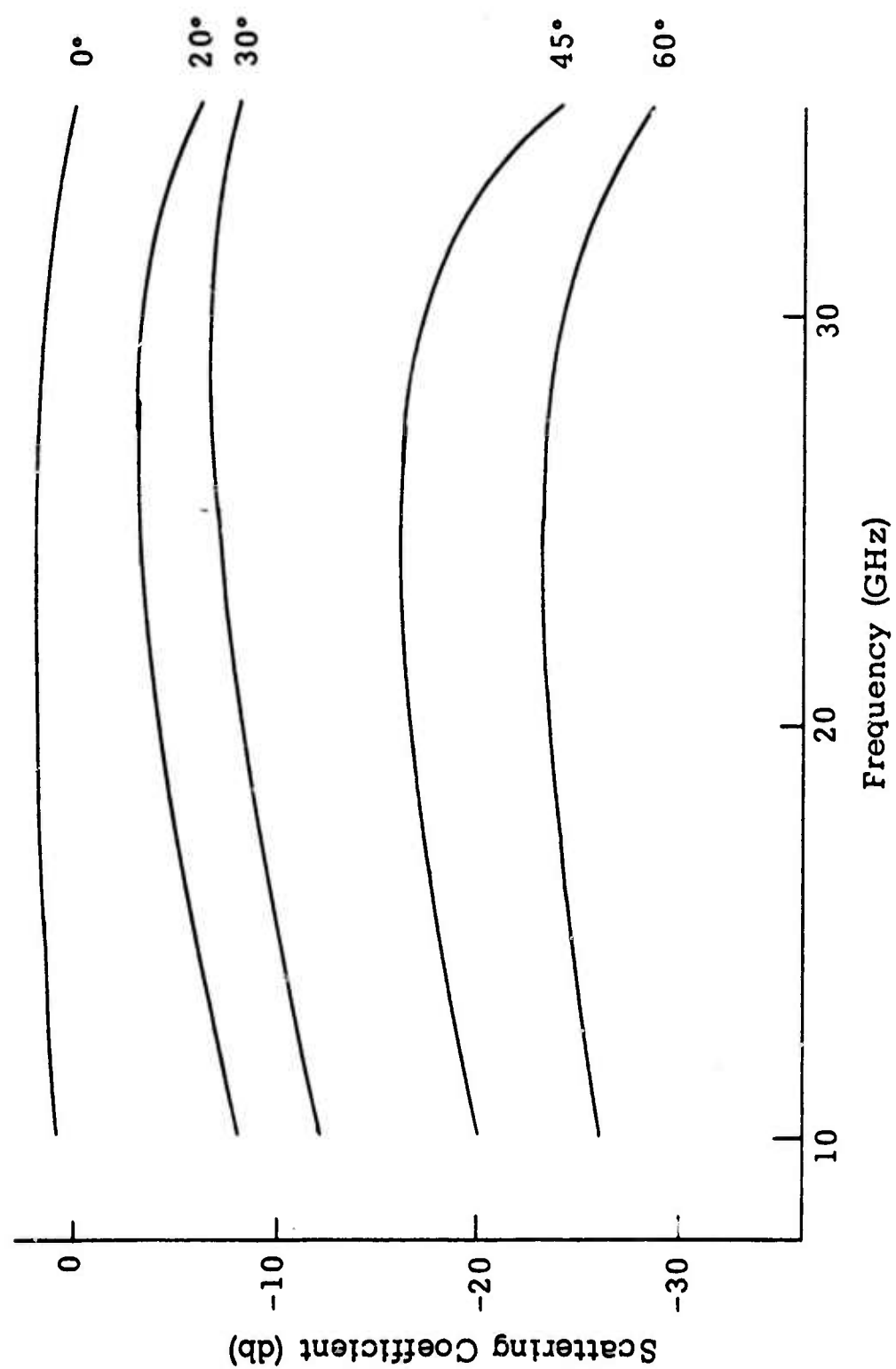


Figure 2.8 Frequency dependence of radar return from the sea.
(After Wiltse, Schlesinger, and Johnson)

CHAPTER 3

SYSTEM INSTRUMENTATION

The system used for this measurements program was designed and built as a part of this research program. The need for flexibility heavily influenced the selection of subassemblies throughout the instrument, and in many cases the subassembly used has many times the actual capability required for this program.

3.1 System Function

The system operates in what is termed a "slow-sweep" mode. In this mode the transmitted frequency is swept from minimum to maximum in a fixed time. The transmitter is gated on by a narrow pulse at a repetition rate from 10 to 10^3 times faster than the sweep rate, hence the transmitter output consists of a pulse train in which each pulse contains a different carrier frequency. This technique is illustrated in figure 3.1. The approach is actually a multiple-discrete frequency method where several hundred discrete frequencies are used and the spacing is such that the output spectrum of one overlaps the spectra of neighboring pulses.

The envelope of the average amplitudes of the returns associated with pulses t_0 through t_2 is the average return power spectrum for the particular target being tested. The handling of the data necessary to obtain this spectrum is complex and is described in detail later.

3.2 System Description

The block diagram of the system is shown in figure 3.2. It consists of three main sections: 1) transmitting, 2) receiving, and 3) data processing.

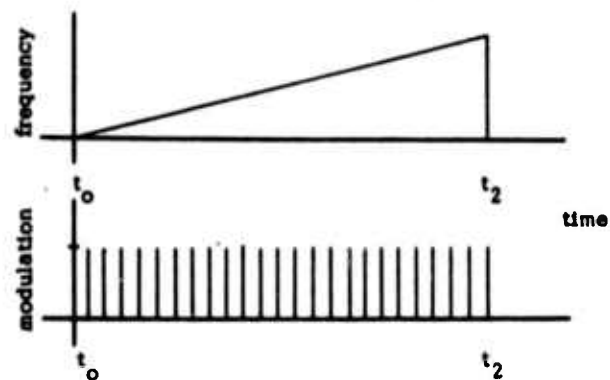


Figure 3.1 Slow-sweep mode sampling technique

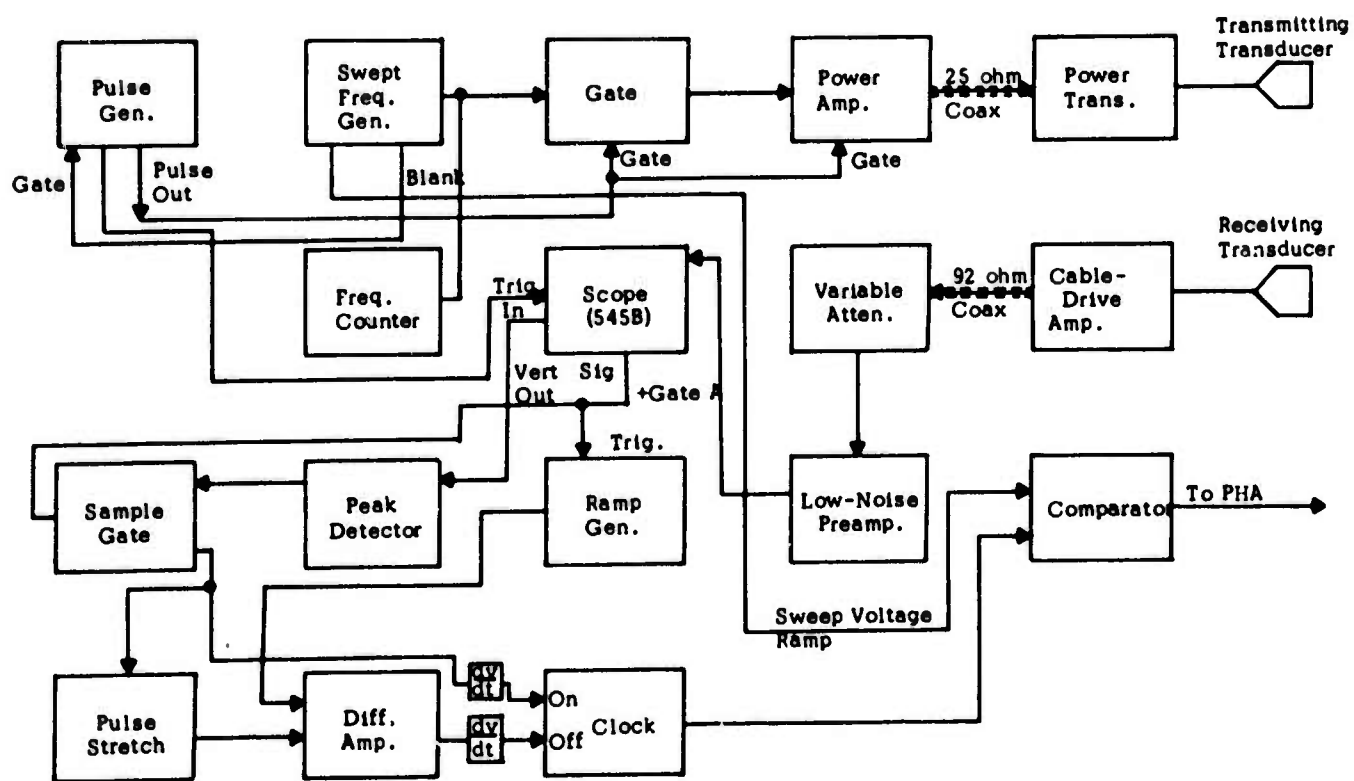


Figure 3.2 Block Diagram of System

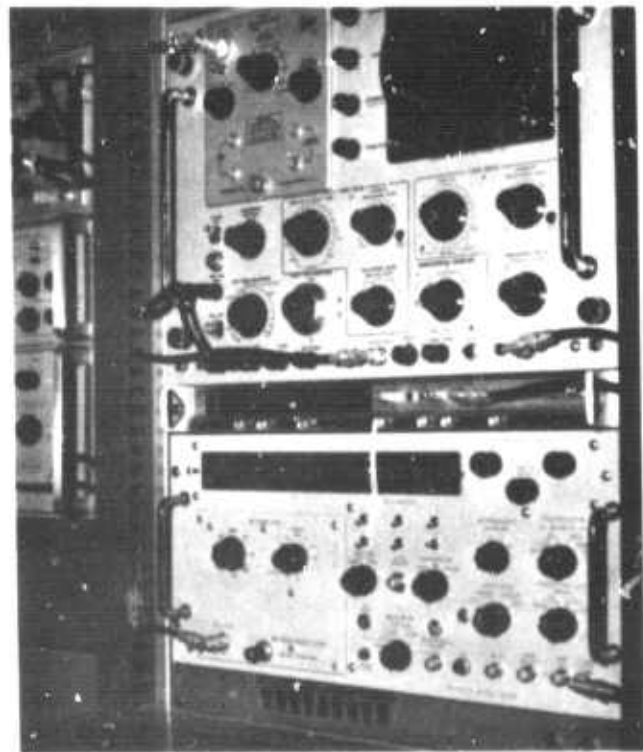
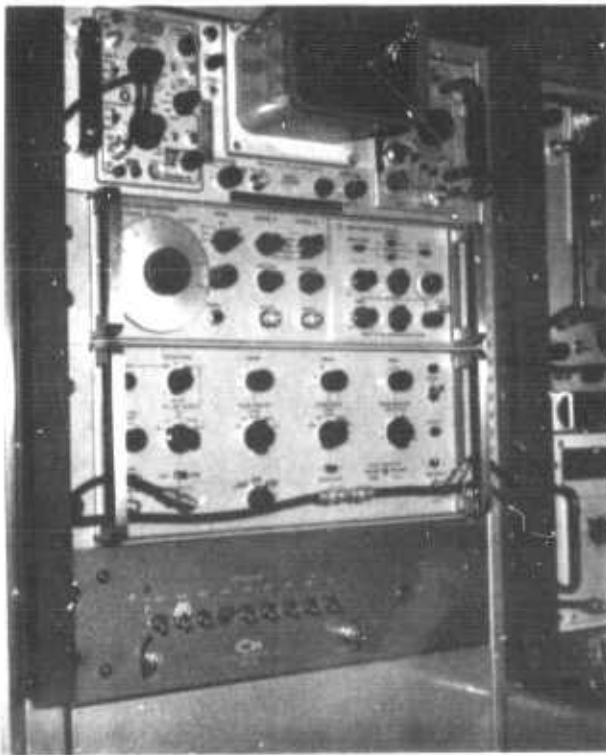
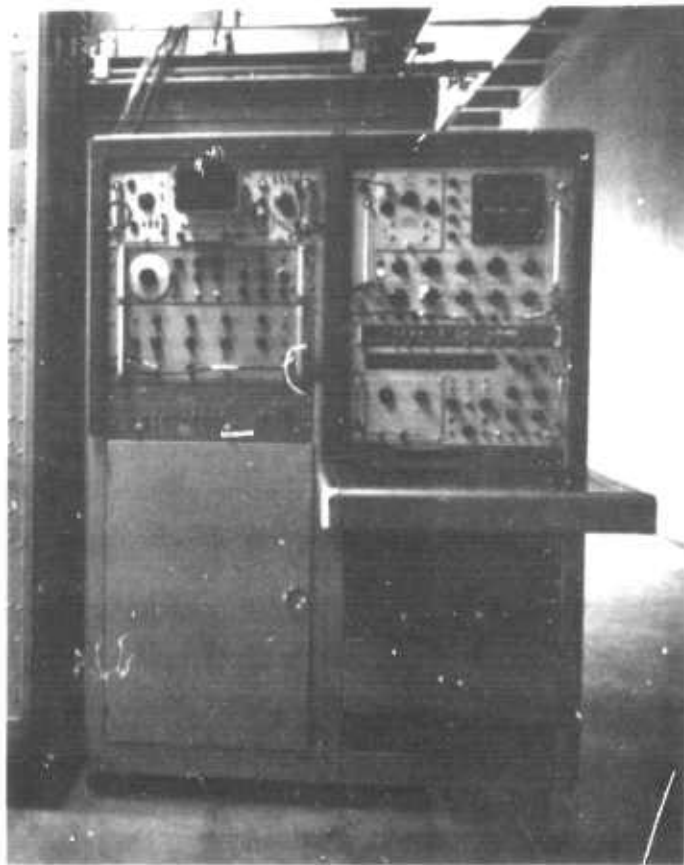


Illustration 3.1 ACOUSTIC TEST FACILITY

3.2.1 Transmitting Section

The transmitting section consists of a multi-purpose sweep frequency generator, pulse generator, gate, gated wide-band power amplifier, step-up pulse transformer, and transmitting transducer.

3.2.1.1 Sweep frequency generator — This generator is a commercial Wiltron Model 610B sweep frequency generator with a 100KHz to 100MHz Model 6104 plug-in unit that serves a multi-purpose role in the system operation. The output signal can be swept between variable f_1 and f_2 frequency settings in a variable time. The output signal is leveled to within ± 0.25 db across the range. In addition to the output signal, the generator provides a blanking pulse, which is used to gate off the pulse generator during the generator retrace interval, and a ramp signal, which is used as a frequency reference in the processor.

In a typical operation the sweep might traverse from 350KHz to 1.2 MHz in 5.0 seconds. The blanking pulse would be 0.2 seconds duration and the reference ramp would rise from 0 volts to 10 volts in 4.8 seconds.

3.2.1.2 Pulse Generator — This generator is a commercial Hewlett Packard Model 214A pulse generator which also serves a multi-purpose role in the system operation. It provides a train of pulses used to drive both the gate and the gated power amplifier. The pulse train has variable pulse width, amplitude, and period. The pulse train is gated off during the sweep frequency generator retrace interval by a blanking pulse from the Wilton 610B. The pulse generator also provides the trigger pulse for the Tektronix scope.

In a typical operation the pulse rate is 100 pulses per second with a pulse width of 0.3 milliseconds and amplitude of -10 volts.

3.2.1.3 Power Amplifier and gate — The amplifier is a Coffman Industries Inc., Model PA-51. The amplifier supplies 55 volts RMS leveled to ± 1 db, to a transducer load over the frequency range of 100KHz to 3.0MHz. The gain is approximately 30. The unit consists of a wide-band, high-power, push-pull amplifier, with a gain of 10, feeding 25 feet of 25 ohm coaxial

cable. The cable is terminated by a 3:1 step-up transformer and 200 ohm resistor across the transducer. An inductor in series with the transducer acts to form a low-pass filter with a cut-off frequency of about 5MHz, depending on the transducer impedance. This arrangement is shown in figure 3.3.

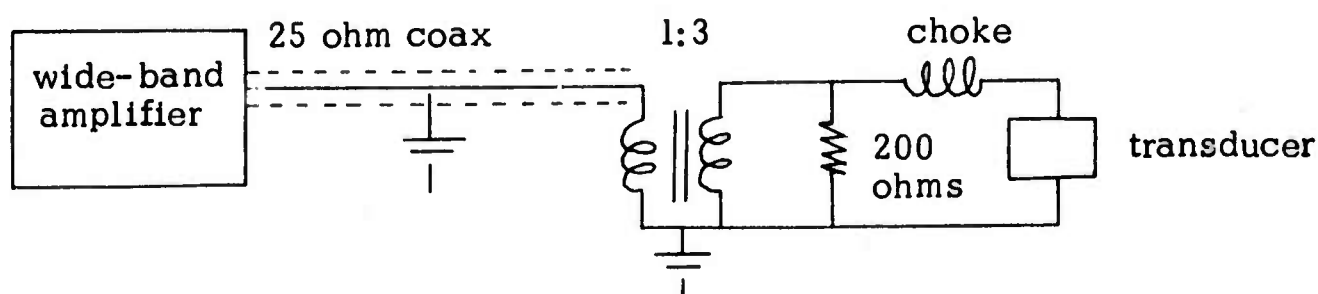


Figure 3.3. Power amplifier termination

The power amplifier is equipped with an optional gating capability that accepts a negative 5-15 volt pulse to reduce the gain by biasing off one stage. The resulting on-off ratio is approximately 30 db. This ratio is inadequate to maintain the receiver input noise at a sufficiently low level, therefore a diode gate precedes the power amplifier. This gate has an on-off ratio of 40 db. The combined 70 db isolation ratio is satisfactory to allow adequate signal-to-noise ratios for the measurements recorded.

3.2.2 Receiving Section

The receiving section consists of a receiving transducer, cable driving amplifier, low-noise preamplifier, final amplifier, and signal attenuators.

3.2.2.1 Cable Driving Amplifier — The high capacitive impedance of the receiving transducer creates a major impedance mismatch at the transducer-cable connection. This is partially overcome by inserting an impedance transforming amplifier. The amplifier is a direct coupled two-stage emitter follower having an input impedance of 25 ohms and an output impedance of

approximately 92 ohms. The output is connected through 25 feet of 92 ohm cable to the low-noise preamplifier. The voltage gain is unity ± 0.2 db across the frequency range 0.1 MHz to 5 MHz. The power gain is approximately 25.

3.2.2.2 Low-Noise Preamplifier — The unit is a Coffman Industries, Inc. Model PA-10. The two-stage preamplifier has a maximum gain of 55 db ± 1 db across the frequency range 0.1 MHz to 3 MHz. The equivalent input noise voltage is less than 30 μ v. The input impedance is matched to the 92 ohm input cable and the output impedance is approximately 1K ohm.

3.2.2.3 Final amplifier — The last stage of amplification is obtained in the preamplifier (Type L) of a Tektronix 545 RM oscilloscope.

3.2.2.4 Attenuators — The receiving section utilizes two variable attenuators to control the input signal. An attenuator prior to the preamplifier controls the signal level to avoid saturation of the first stage. Another 0-72 db attenuator separates the two amplifier stages to protect the second stage and enhance the output signal-to-noise ratio. In typical operation the second attenuator is approximately 20 db, but never less than 10db.

3.2.3 Data Processing Section

The role of the data processing section is to convert the amplified video return signal to a form representative of the average power received as a function of frequency. This is accomplished by sampling the amplitude of the detected signal, converting the sample from analog to digital form, and storing the digital information in a multi-channel memory in a manner such that each storage channel corresponds to a different transmitted frequency. The section consists of an envelope detector, sample gate, pulse stretcher, ramp generator, differential amplifier, gated clock, comparator, and pulse height analyser.

The output of the receiving section is a display of the return signal on the CRT of a Tektronix 545B oscilloscope. The input to the data pro-

cessing section is the vertical signal displayed as obtained at the VERT SIG OUT of the scope. The dual time base of the 545B provides a variable width sampling gate pulse which can be positioned as desired throughout the return signal interval. This gate pulse is used to drive a sampling gate which selects a portion of the return signal after detection. The sampled pulse is stretched and amplitude compared with a ramp function. This operation is shown in figure 3.4.

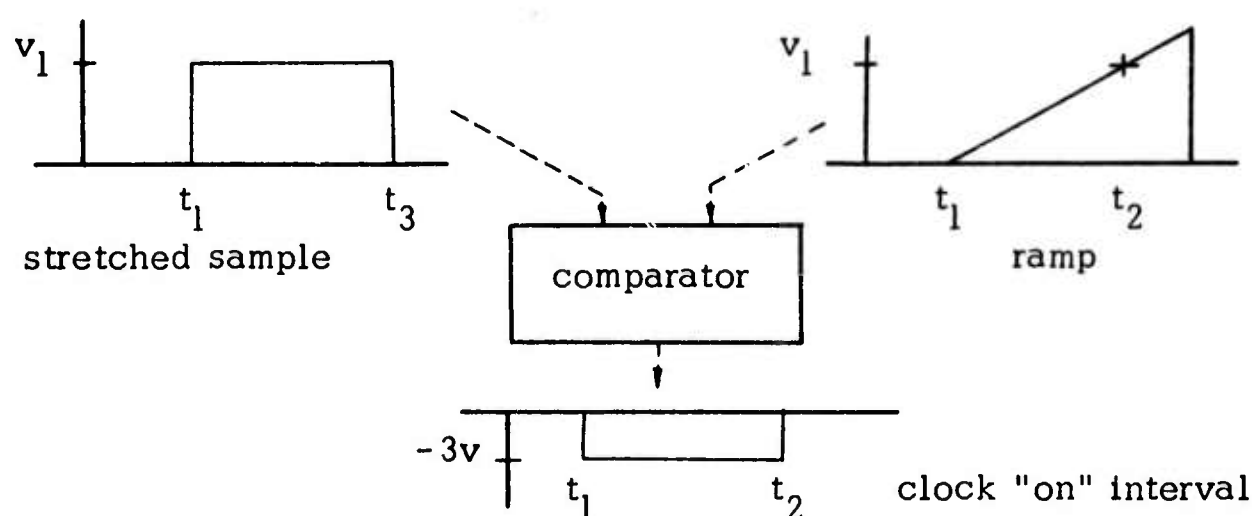


Figure 3.4

The comparator produces an "on" pulse at the start of the stretched pulse, and an "off" pulse at the instant the ramp voltage equals the sampled pulse voltage. This interval represents the "on" time of a 5.0 KHz clock. The clock output is a train of 100 n sec, uniform amplitude pulses.

The storage channels mentioned earlier are actually a part of a 256 channel pulse height analyzer. This equipment is designed to analyze incoming pulses and separate them into channels according to height. The analyser in essence counts the number of pulses of particular heights, i.e. a single count is recorded in one channel for one pulse of a particular amplitude. To utilize this device in the data processing section, such that the channels represent frequency rather than amplitude, the clock burst, which contains pulses proportional in number to the signal amplitude, must be varied in amplitude across the sweep-frequency range. This operation is performed by a comparator which amplifies the clock pulses by a

gain set by a reference ramp function. The ramp function is obtained from the sweep-frequency generator and varies proportionately with the frequency change.

The record accumulated in the 256 storage channels represents the average signal amplitude as a function of frequency. The number of counts in each channel is recorded and subsequently converted by a computer program to a scattering coefficient.

3.2.3.1 Sampling Circuit — The input to the processing section is the amplified video return voltage from the oscilloscope vertical deflection plates. This signal is detected in a linear diode detector and sampled by gating through a commercial solid state switch, which is controlled by the Tektronix 545B +A GATE pulse. The switch provides an on-off ratio of greater than 30 db for the frequency range 50KHz to 10MHz with less than 1db insertion loss.

3.2.3.2 Conversion Circuit — The objective of this circuit is to convert the amplitude of the sample pulse into a time interval in a proportionate manner. To accomplish this the sample pulse is stretched from the sample width (approximately 0.02 m sec) to approximately half the inter-pulse period, i.e. 10 m sec for $\text{prf} = 50 \text{ Hz}$. The amplitude of the stretched pulse is equal to the amplitude of the sample pulse. The leading edge of the sample pulse also triggers a ramp generator. The ramp is compared with the stretched pulse by a differential amplifier which produces an output voltage of -3 volts when the pulse amplitude exceeds the ramp, and 0 volts when the ramp voltage exceeds the pulse. The resulting -3 volt pulse has a duration proportional to the amplitude of the sampled return signal. This pulse is fed to a 5 KHz clock "on" gate. The number of 100 n sec clock pulses produced is the measure of the amplitude of the return signal.

The clock-pulse train is one input of an operational amplifier. The reference input to the amplifier is the frequency driving ramp from the sweep frequency generator. The ramp duration is several times that of the pulse train, hence the output of the operational amplifier consists of a series of individually equal amplitude pulse trains, each group having

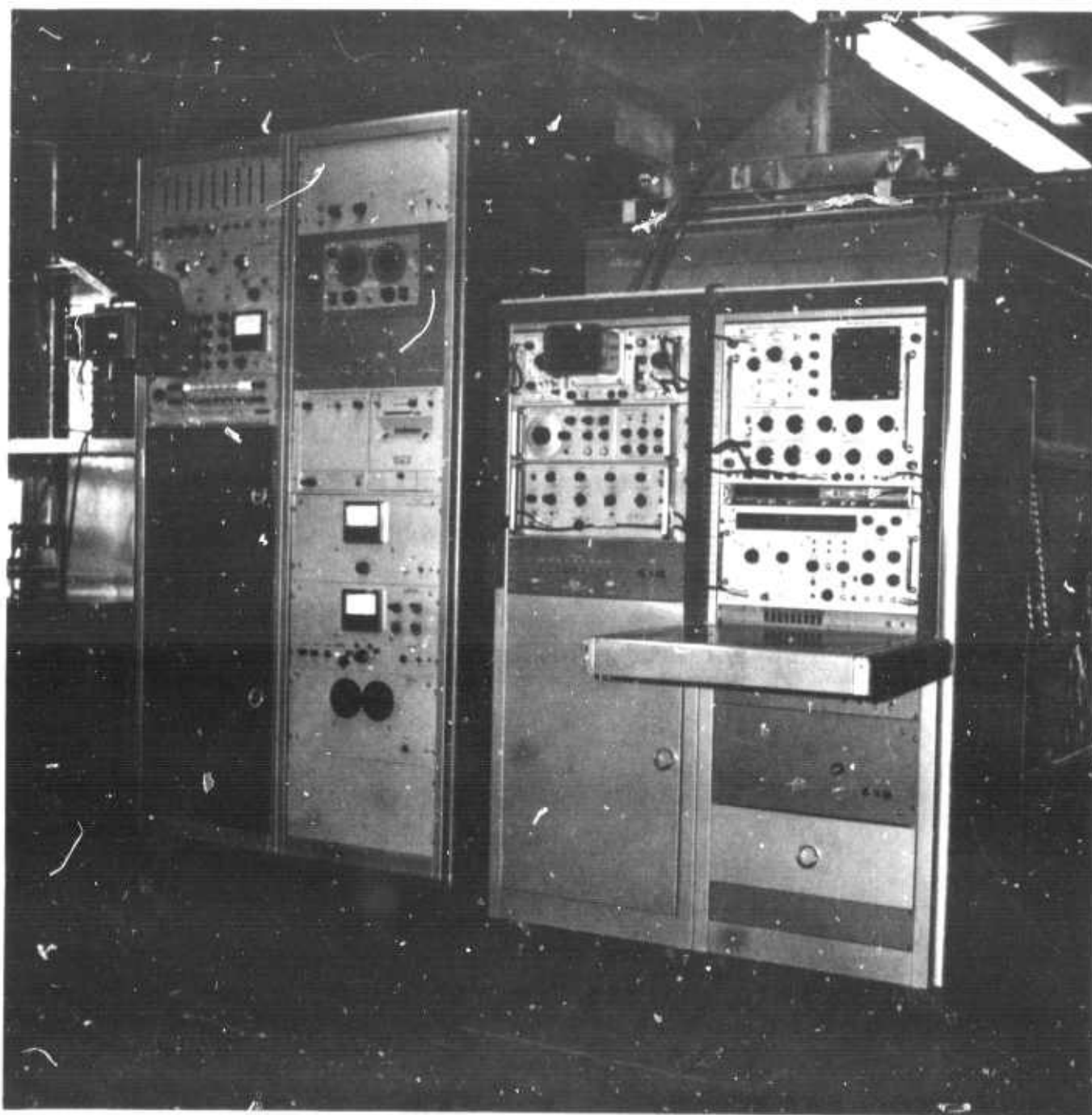


Illustration 3.2 VIEW OF ACOUSTIC TEST FACILITY
Showing Pulse-Height Analyzer (left)

an amplitude proportional to the frequency of the transmitted signal. The operational amplifier output is amplified by a linear amplifier and fed to the pulse height analyser.

3.2.3.3 Pulse Height Analyser — The analyser used is the Radiation Counter Laboratories Mark 20 Model 2603. It consists of 256 channels of memory having a per channel capacity of 2^{16} counts. Basically it consists of an analog-to-digital converter, a simple digital computer with magnetic core memory, a cathode-ray-tube data display system, and a paper-tape data printer.

3.3 Data Handling

The system output is a printed record of the number of counts recorded in each of 256 storage channels. Each count represents an increment of the total received signal voltage. Each channel represents a segment of the total transmitted spectrum. A determination is made as to the correspondence between channel numbers and frequencies. The channel counts are then smoothed by averaging the counts in five channels centered about the discrete frequency to be tabulated. Referring to the system calibration curve of counts versus voltage, provides the necessary conversion of the tabulated results to voltage and ultimately to average power received.

In practice the record is preserved as average number of counts per frequency and later converted to power. The reason for this is due to the calibration procedure. Ideally, the frequency sweep from minimum, f_1 , to maximum, f_2 , is linear and the traverse from minimum channel, C_{f_1} , to maximum channel, C_{f_2} , is also linear and directly proportional. To insure this, the analog-to-digital conversion circuit is set to provide a count of four for zero received signal and a count of thirty-two for maximum received signal. After recording the return signal from a target, a zero input record is made. This record of counts is then subtracted from the target record, hence any non-linearity present during the test is eliminated. The count versus frequency record is entered into a computer program for conversion to average power.

Actually, since the ultimate measurement desired is the scattering coefficient, σ^0 , the conversion is not to average received power, but instead to the ratio of the average received power to average transmitted power. The relationship used is:

$$\sigma^0 = \frac{\langle P_r/P_t \rangle / \langle P_r/P_t \rangle_c}{r_c^2 \iint_S \frac{g_t g_r}{4\pi r_t^4} dA} \quad (3.1)$$

where: $\langle P_r/P_t \rangle$ = power ration (target signal)

$\langle P_r/P_t \rangle_c$ = power ratio (calibration signal)

r_c = distance between calibration transducers

r_t = distance from transmitter to target

A = area illuminated by beam

g_t = normalized gain of transmitting transducer

g_r = normalized gain of receiving transducer

The calibration information is the count record for the transducer pair when they are sighted at each other at a distance r_c meters. A more complete discussion of equation (3.1) is contained in chapter 4.

3.4 System Limitations

The system design objective of obtaining the measurement of broad-spectrum backscatter required a technique of recording a very large quantity of data quickly and with a minimum of manual handling. This objective necessitated a relaxation in the absolute accuracy of the measurements. In addition the 30:1 frequency range sought was not obtained due, primarily to the limited capability of the piezoelectric transducers.

3.4.1 System Accuracy

The fact that the scattering coefficient is expressed as a ratio of

the target return and the calibration return reduced the complexity of the calibration procedure, i.e. whether or not the received power was absolutely correct was immaterial so long as both the target and calibration measurements were in error by the same amount. Even so the accuracy of the scattering coefficient measurements is considered valid only to within 3 db.

The principal error is due to the method of data storage. In practice, approximately 200 channels of the 256 Channel Analyzer are employed. The voltage range required to traverse these 200 channels is 10 volts. Therefore, to perform the ideal recording where each clock count burst is recorded in a single channel, every pulse of the possible 32 pulses must be equal in amplitude to within $\pm .05$ volts. The system capability is approximately $\pm .15$ volts maximum deviation which occurs for the full count number, i.e. 32. The recording of the four count zero input reference signal is almost ideal, but the subsequent subtraction from the target signal is unavoidably in error. For this reason it was necessary to smooth the results by averaging over five channels.

A second cause of error is due to the dynamic range of the receiving section and data processing section combined. This dynamic range is approximately 20 db which is adequate for the expected 18 db of fading. However, due to the narrow frequency response curve of the transducers, much of this range was absorbed by gain changes. By repeating data runs several times and varying the center position of the dynamic range with each run, it was possible to compensate for much of the gain change, however the extreme ends of the transducer response skirts for each run were generally regarded as unusable.

To minimize all error terms, the data for each target was repeated until reasonable assurance of data accuracy was attained.

3.4.2 System Frequency Range

The frequency response of the transmitting and receiving section was discussed earlier, however neither constitutes the critical control or the system frequency range. This is controlled by the transmitting and receiving transducers. No single transducer pair is capable of providing

sufficient gain to be usable over the entire frequency range desired, i.e. 0.1 MHz to 3.0 MHz, therefore it is necessary to employ several pairs.

In most documented acoustic wave experiments, transducer gain is measured by transducer pairs and seldom is the gain of an individual transducer obtained. In this study an attempt was made to determine the absolute gain of a single transducer. To accomplish this, two type measurements were necessary.

3.4.2.1 Single Transducer Measurement — The test setup for this measurement is shown in figure 3.5. A single transducer is used as both the transmitting and receiving antennas. The transducer is oriented so that the acoustic wave propagation is normal to a 0.25 inch thick plate glass target.

The single transducer measurements were recorded with the sweep frequency oscillator set to a fixed frequency. The measurement was the ratio of V_{IN}/V_{OUT} . The transducer gain is calculated from the equation

$$G = \frac{V_{IN}}{V_{OUT}} \frac{4\pi(2h)}{K} \quad (3.2)$$

where $2h$ is the distance to the target, λ is the wave length, and K is the reflection coefficient, which is unknown. Equation (3.2) was developed from the equation for one-way propagation by assuming the receiving transducer is at the image point of the transmitting transducer and that $K = 1$. The correct value of K is determined later.

Plate glass was used as the target to insure a smooth surface to all wave lengths in the range of interest. The calculated reflection coefficient for glass in water is 0.83.

As is evident in the data, using the plate glass as a target created some unexpected difficulties. The glass target was approximately 0.25 inches thick, which is equal to one wave length at about 1 MHz (velocity of propagation of sound in glass is 6 km/sec). Assuming the glass acts as a low-loss transmission line, the terminating impedance on the backside of the plate is reflected to the front side and thus presents a matched

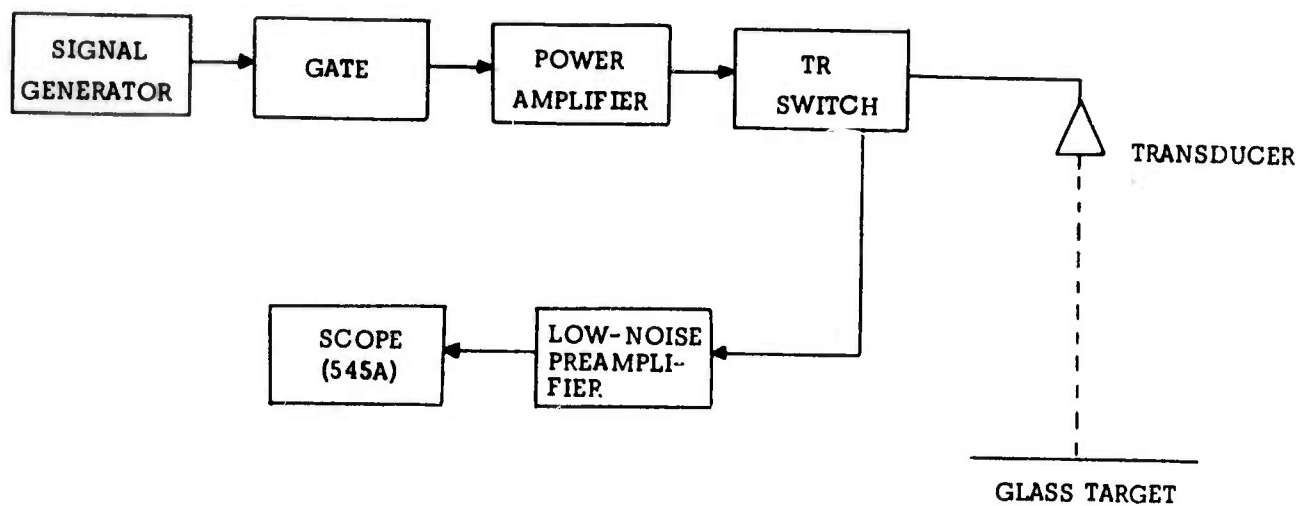


Figure 3.5. SINGLE TRANSDUCER TEST

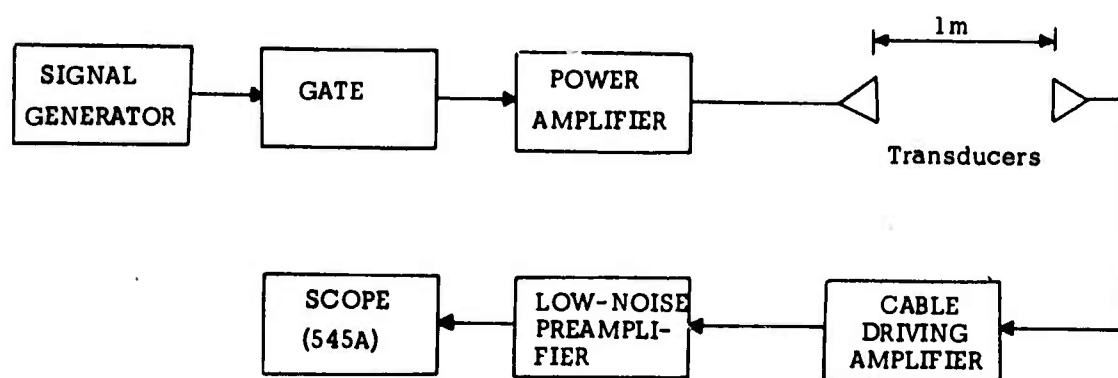


Figure 3.6. TRANSDUCER PAIR MEASUREMENT

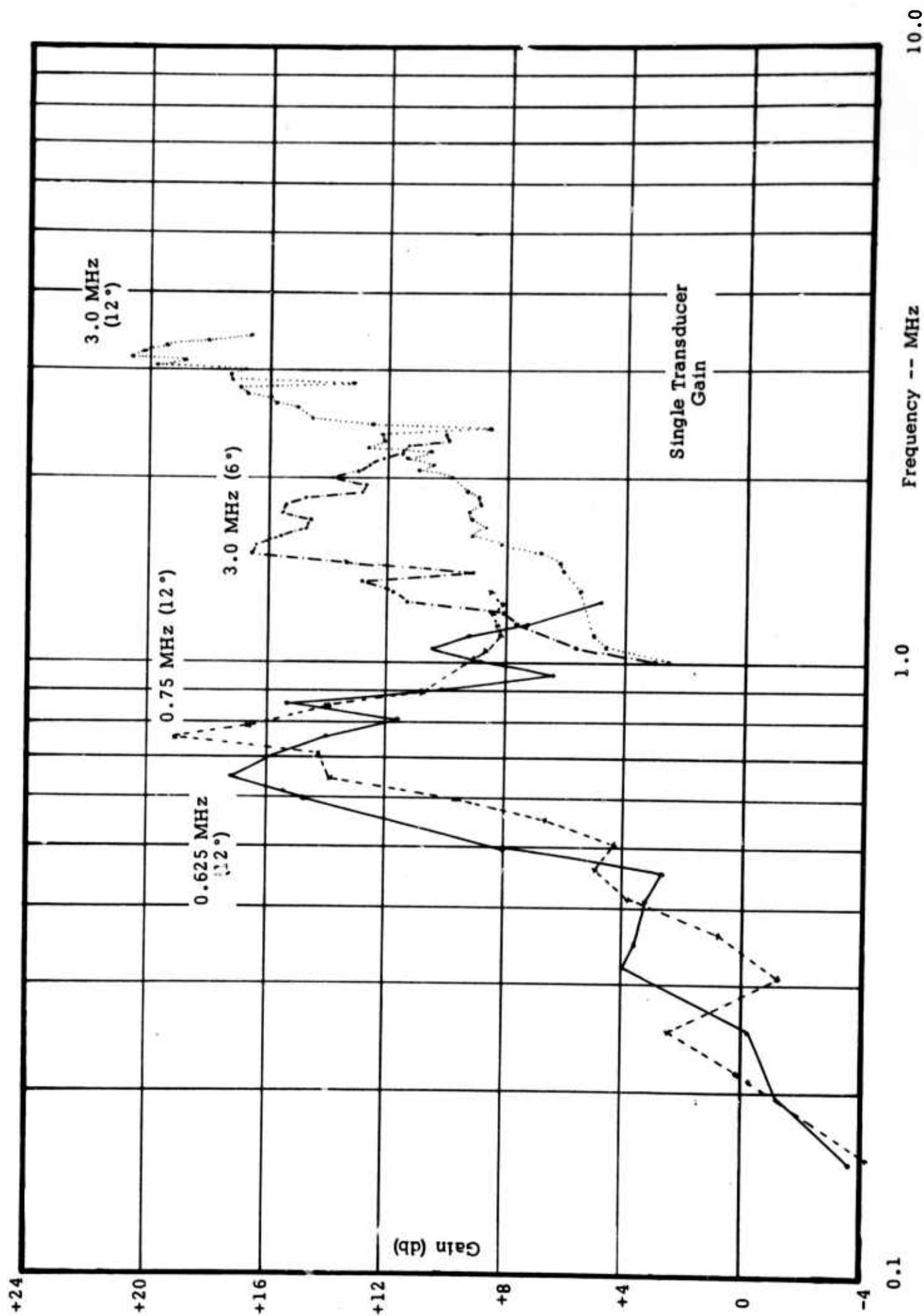


Illustration 3.3

impedance termination to the incident energy. The matched condition should appear at about 0.5 MHz, 1.0 MHz, 1.5 MHz, 2.0 MHz, 2.5 MHz, and 3.0 MHz based on the thickness of the glass. The results confirm the condition at these frequencies. Fortunately the nulls were very sharp for frequencies above 1 MHz. The two nulls at 1 MHz and 0.5 MHz were broad, and hence the data are suspect in this range.

3.4.2.2 Transducer Pair Measurements — The test set up for this measurement is shown in figure 3.6. Two transducers were aligned directly facing each other, 1.0 meter apart. The measurement recorded was the ratio of voltage at the receiving transducer to the voltage at the transmitting transducer, V_{OUT}/V_{IN} .

In this arrangement signals were recordable for the entire frequency range of 0.1 MHz to 3.0 MHz for nearly all transducers. The gain, either receiving or transmitting, is calculated using the equation for one-way propagation.

$$G_t = \frac{V_{IN}}{V_{OUT}} \frac{(4\pi R^2)}{G_r \lambda^2} \quad (3.3)$$

where: G_t = gain of transmitting (or receiving) transducer
 G_r = gain of receiving (or transmitting) transducer measured by single transducer method
 R = spacing between transducers
 λ = wavelength

Although it was mentioned that the entire frequency range can be covered in the pair measurements, G_t can only be calculated over small segments due to the limited number of values of G_r (equation 3.2) available for calculation from the single transducer measurements.

The data plots are very similar in shape to those obtained in the single transducer measurement, especially above 1 MHz. However,

there is a difference in magnitude of 14-15 db. This difference is due to the fact that the reflection coefficient, K, was assumed to be unity in equation (3.2). The actual value of K was determined using both the single and pairs data.

$$K = \left(\frac{2h}{R} \right) \left(\frac{V_{IN}}{V_{OUT}} \right) \left[\left(\frac{V_{OUT}''}{V_{IN}''} \right) \left(\frac{V_{OUT}'}{V_{IN}'} \right) \right]^{1/2} \quad (3.4)$$

where h = height above target (single)

R = spacing (pairs)

V_{IN}'' and V_{OUT}'' = input and output of receiving transducer (single)

V_{IN}' and V_{OUT}' = input and output of transmitting transducer (single)

V_{IN} and V_{OUT} = input and output of pairs measurement

The value of K for the 3.0 MHz 12° and 6° pairs was 0.21. This compares with a calculated value for K of 0.83. The difference is most likely due to a combination of effects such as 1) difference in the power delivered to the transducer mount as compared to that actually delivered to the water, 2) difference in actual properties of the glass target and ideal properties of glass; density equal 2400 kb/cm³ and velocity of propagation equal 6 km/sec, and 3) transmission line impedance transformation effects.

Using a K value of 0.21 the receiving gain was computed for each transducer used in the experiment both as individual units and in pairs.

The disk or piston transducers used in this work have an active surface area measuring several wave lengths across and produce a directive antenna pattern. The far field pattern for a flat disk transducer operating in an infinite baffle is given by

$$F(\theta) = \frac{2J_1(ka \sin \theta)}{ka \sin \theta} \quad (3.5)$$

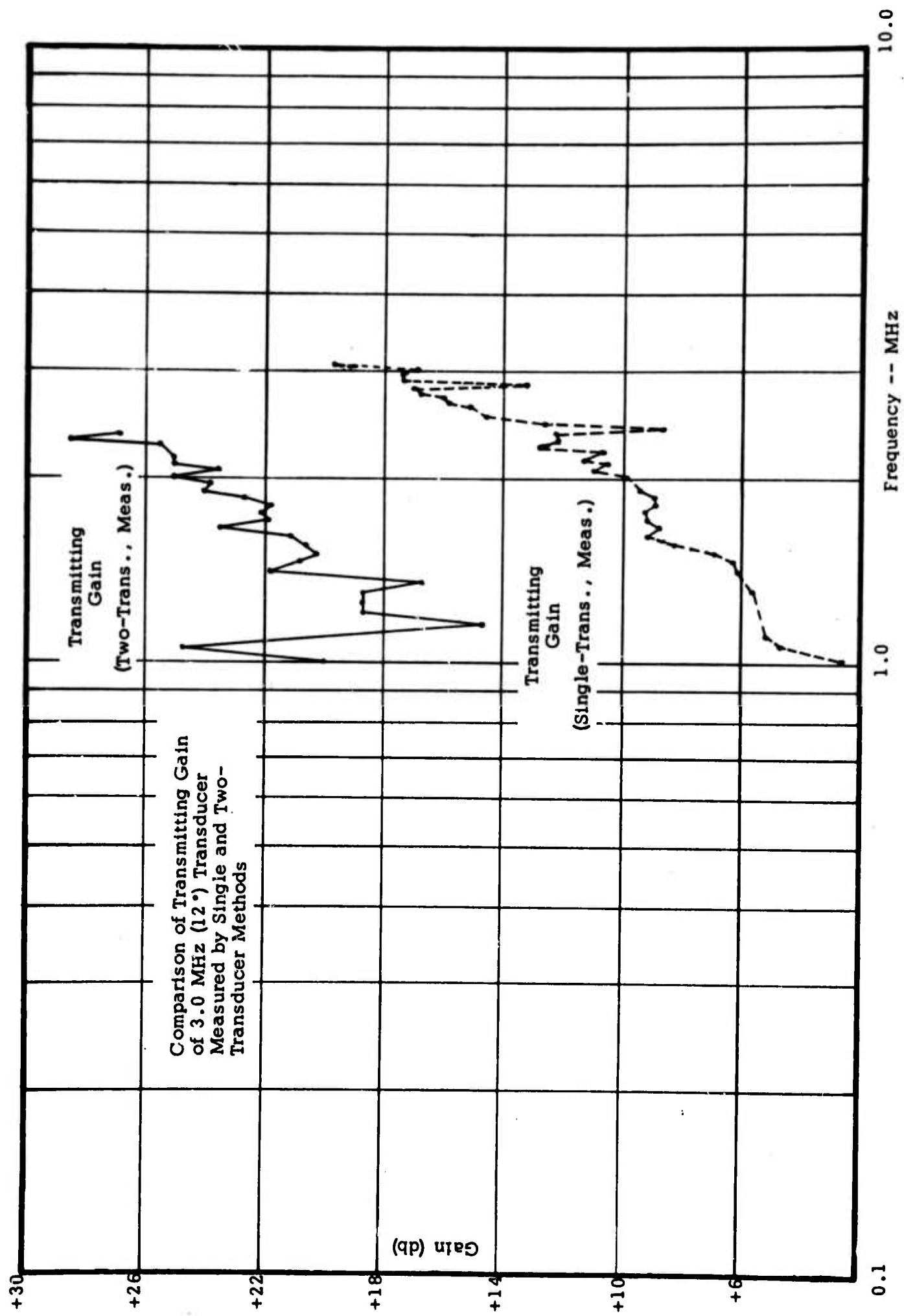


Illustration 3.4

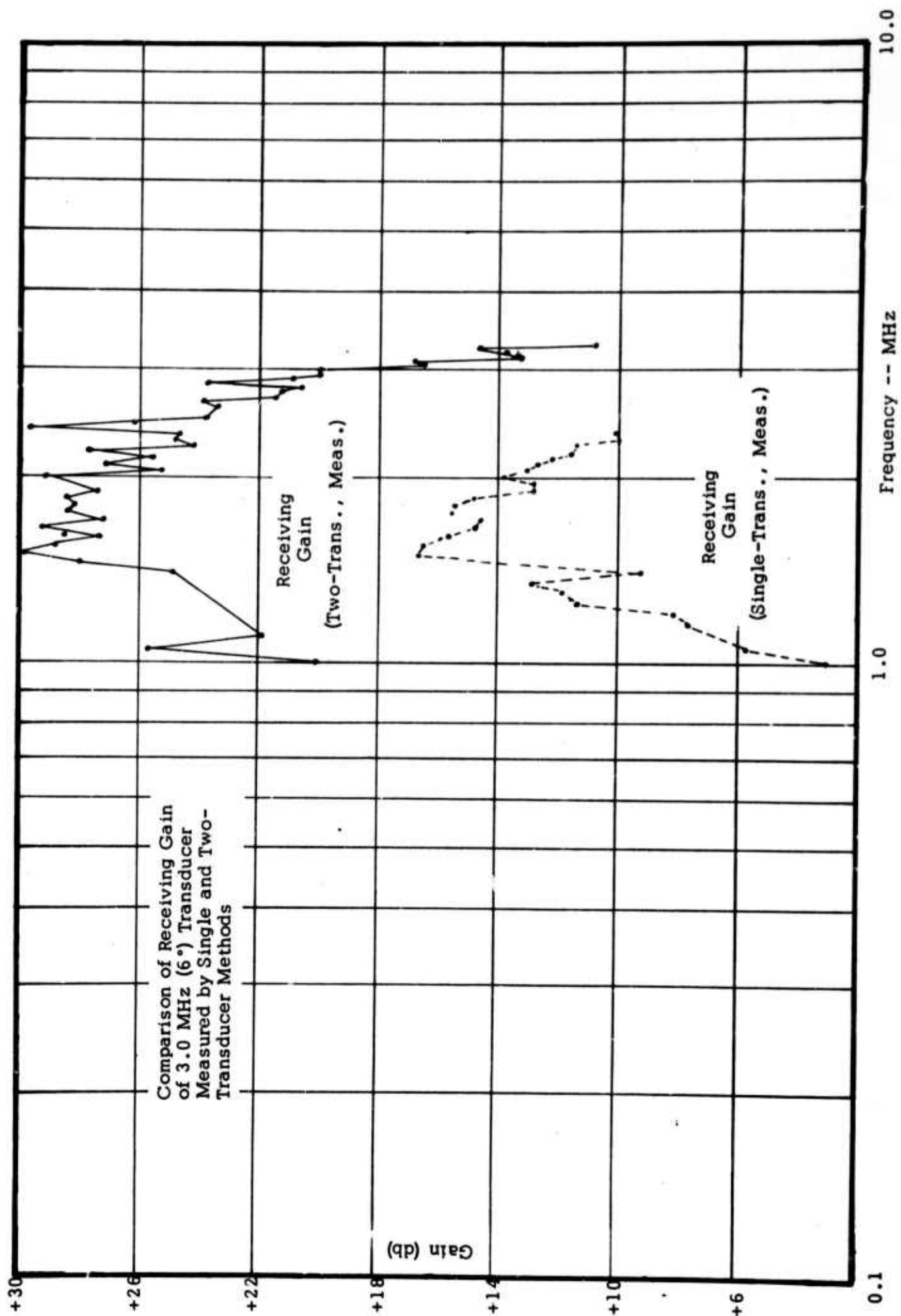


Illustration 3.5

where J_1 = Bessel function of first kind and first order

k = wave number

a = radius of flat disk

Θ = angle from surface normal

3.5 System Imaging Capability

The basic design of the system concentrated on obtaining back-scatter power spectra from homogeneous rough surfaces, however to facilitate application studies, an imaging capability was also included. The system will record a B-scan presentation of the return signal. The scan is presented on a Tektronix 561 scope equipped with a P-16 phosphor CRT. This phosphor has excellent characteristics for image recording, including rapid decay time and high dynamic range. The recording sheet film and film developing process were chosen to give maximum gray scale in the final image.

The system arrangement for imaging uses the same transmitting and receiving sections, however the data processing section is disconnected. The VERT SIG OUT of the Tektronix 545B is fed directly through a 5 MHz band width amplifier to the grid of the Tektronix 561 CRT. A delayed sweep time base unit (3B3) allows positioning of the return signal so that the intensity modulated raster shows only the target return interval. The presentation technique employed, as well as the type images obtained, is discussed in Chapter 6.

In order that controlled conditions could be assured during recording of images, a linear motion carriage was constructed. This device, in essence, simulates aircraft flight except that its motion is uniform and extremely stable. The carriage velocity can be varied over an approximate 50:1 range with a minimum of approximately 0.5 cm/sec.

CHAPTER 4

SCATTERING EXPERIMENT

The experiment program undertakes two major areas of investigation. This chapter and Chapter 5 deal with the measurement of broad-spectrum backscatter from statistically rough surfaces. The objectives are to determine the nature of the frequency dependence of the backscatter from various surfaces and to compare the results with theory. The second area of investigation is handled in Chapter 6 which establishes the characteristics of broad-spectrum illumination applicable to imaging radar systems.

Two surfaces were prepared for measurement representing a gently undulating "rough" surface and a gently undulating "rough" surface with small scatterers superimposed. The first surface presents a broad roughness density spectrum. The second has the same spectrum with a narrow high frequency spectrum added. The broad-spectrum backscatter from each surface was measured and the results are presented in Chapter 5.

In this chapter the measurement technique is discussed, the targets are described, some characteristics of broad-spectrum illumination are shown, and the acoustic-electromagnetic analogy is explained.

4.1 Measurement Technique

The scattering experiment conducted constitutes a case of re-radiation from a surface sufficiently rough that the re-radiated energy is composed entirely of scatter components. This is, the amount of reflected energy in the re-radiated field is negligible. Therefore it is sufficient to determine only the scattering cross section. The scattering cross section is measured as a function of angle and frequency by measuring the re-radiated power which is related to the scattering cross section by the radar equation.

$$\langle P(\theta, \lambda) \rangle = \iint_S \frac{P_T G_T(\psi_T) G_R(\psi_R) \lambda^2 \sigma^0}{(4\pi)^3 r_T^2 r_R^2} dA \quad (4.1)$$

where: $P(\theta, \lambda)$ = the average of the received power obtained over an ensemble of surfaces

P_T = transmitted power

$G_T(\psi_T), G_R(\psi_R)$ = the gain function of the transmitting and receiving antennas (transducers) respectively. Each is assumed to be circularly symmetric.

λ = wavelength of radiation

S = mean surface illuminated

σ^0 = scattering cross section

r_T, r_R = range from mean surface to transmitter and receiver

Backscatter measurements were made using sufficiently narrow beam antennas (transducers) that the assumption that the scattering cross section was constant over the illuminated area was considered valid. The measurements recorded were time independent over the effective illuminated area and the steady state was assumed to exist. This condition is referred to as "beam width limitation" and consists of utilizing a sufficiently wide transmitted pulse to simultaneously illuminate the entire effective area on the surface.

With the assumption of constant σ^0 over the surface, equation (4.1) can be written as:

$$\langle P(\theta, \lambda) \rangle = \sigma^0(\theta, \lambda) \iint_S \frac{P_T G_T(\psi_T) G_R(\psi_R) \lambda^2}{(4\pi)^3 r_T^2 r_R^2} dA \quad (4.2)$$

The calibration procedure detailed in Chapter 3 described the recording of direct one-way power with the transmitting and receiving transducers

directed toward each other. This measurement is convenient for normalization of the average received power. The calibration measurement can be written as:

$$P_c = \frac{P_{Tc} G_T(0) G_R(0)}{(4\pi r_c)^2} \quad (4.3)$$

where r_c is the distance separating the two transducers. The normalized power is then:

$$\langle P_n(\theta, \lambda) \rangle = \sigma^0(\theta, \lambda) r_c^2 \iint_S \frac{g_T(\psi_T) g_R(\psi_R)}{r_T^2 r_R^2} dA \quad (4.4)$$

where $g_T(\psi_T)$ and $g_R(\psi_R)$ are the normalized antenna gain functions having a maximum of unity. The integral accounts for the "aperture effect" which is the weighing of the scattered signals by the antenna gain functions. This effect has been detailed by Parkins (1966).

Because of the system operation employed in this experiment it is convenient to express equation (4.4) as follows:

$$\sigma^0(\theta, \lambda) = \frac{[\langle P(\theta, \lambda) \rangle / P_T] [P_{Tc} / P_c]}{r_c^2 \iint_S \frac{g_T(\psi_T) g_R(\psi_R)}{r_T^2 r_R^2} dA} \quad (4.5)$$

The "aperture effect" integral is calculated separately and is a constant for each θ and λ . The cross section is then determined by the measured ratio $\langle P(\theta, \lambda) \rangle / P_T$ and P_{Tc} / P_c . The transmitted power used for all measurements and calibrations was constant, hence $P_T = P_{Tc}$, however the ratios were calculated individually and then multiplied in equation (4.5). The reason for this will become obvious when reviewing the data recording procedure.

As described in Chapter 3, the backscattered energy is recorded as a voltage amplitude on a frequency ordinate, i.e. a voltage spectrum.

The record is collected for the calibration set up, where the transmitting and receiving transducers are facing each other, and for several incidence angles on the target. If the transducer performance was not highly frequency dependent and their response were more repeatable, the target return could be used directly in equation (4.5) with a suitable normalization factor. However, to insure valid results the transducer characteristics are recorded for the exact frequency spread as the target data and is repeated during each data run. The P_{TC}/P_C plot for each data run are used on a point-by-point frequency basis to calculate σ^* in equation (4.5). Even with this care, the frequency response curve of the transducers is not sufficiently reliable and repeatable on the extreme skirts to lend confidence to measurements far removed from resonance. To illustrate the characteristics of the transducer, the pulse height analyzer display is shown in figure 4.1a for the 0.5 MHz transducer pair. Figures 4.1b and c are shown to illustrate the method used to record the return over the entire frequency range. The gain in 4.1b is 6db less than that of 4.1a, 4.1c is 12db less than 4.1a. Figure 4.1d shows the zero return reference count. The spikes at each end are the minimum and maximum frequency marks, f_1 and f_2 . The $\langle P(\Theta, \lambda) \rangle / P_T$ curve is calculated for all three data runs and superimposed as shown in figure 4.2 to obtain the points used to calculate the scattering coefficients.

4.2 Measurement Set-up and System Parameter

The measurement of σ^* , as discussed earlier, requires the measurement of the average of the received power over an ensemble of surfaces. These measurements were obtained using a mechanical system which rotated the statistically rough targets under the fixed transducers. The transducers were mounted on a boom which allowed positioning of the transducers at fixed angles, relative to the target normal, at a constant range from the target.

The target was rotated at a constant rate of 3 rpm to minimize turbulence of the water. The transmitter pulse width of 300 microseconds

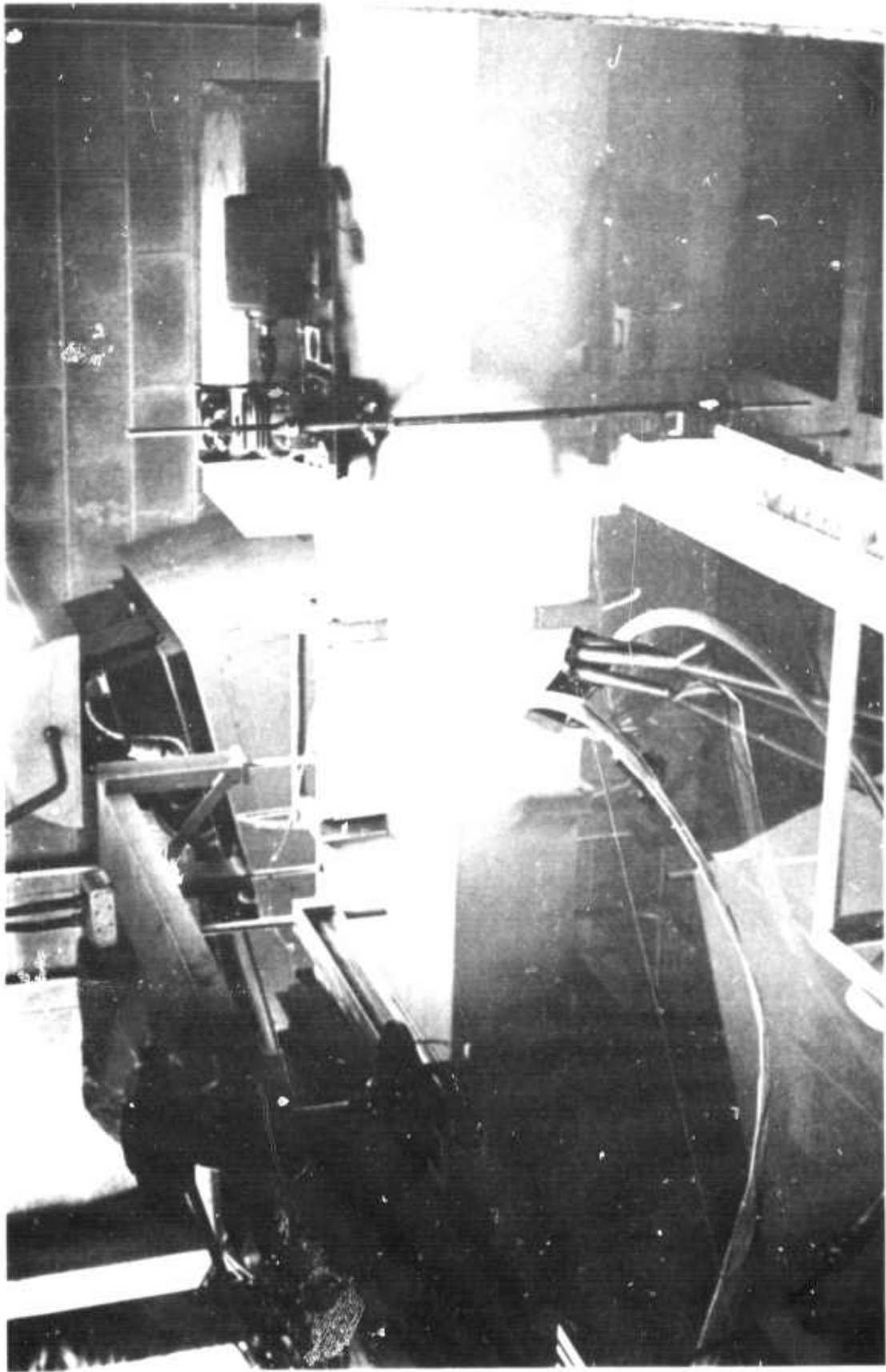


Illustration 4.1 ACOUSTIC TANK ARRANGEMENT USED FOR RECORDING OF
BACKSCATTER MEASUREMENTS

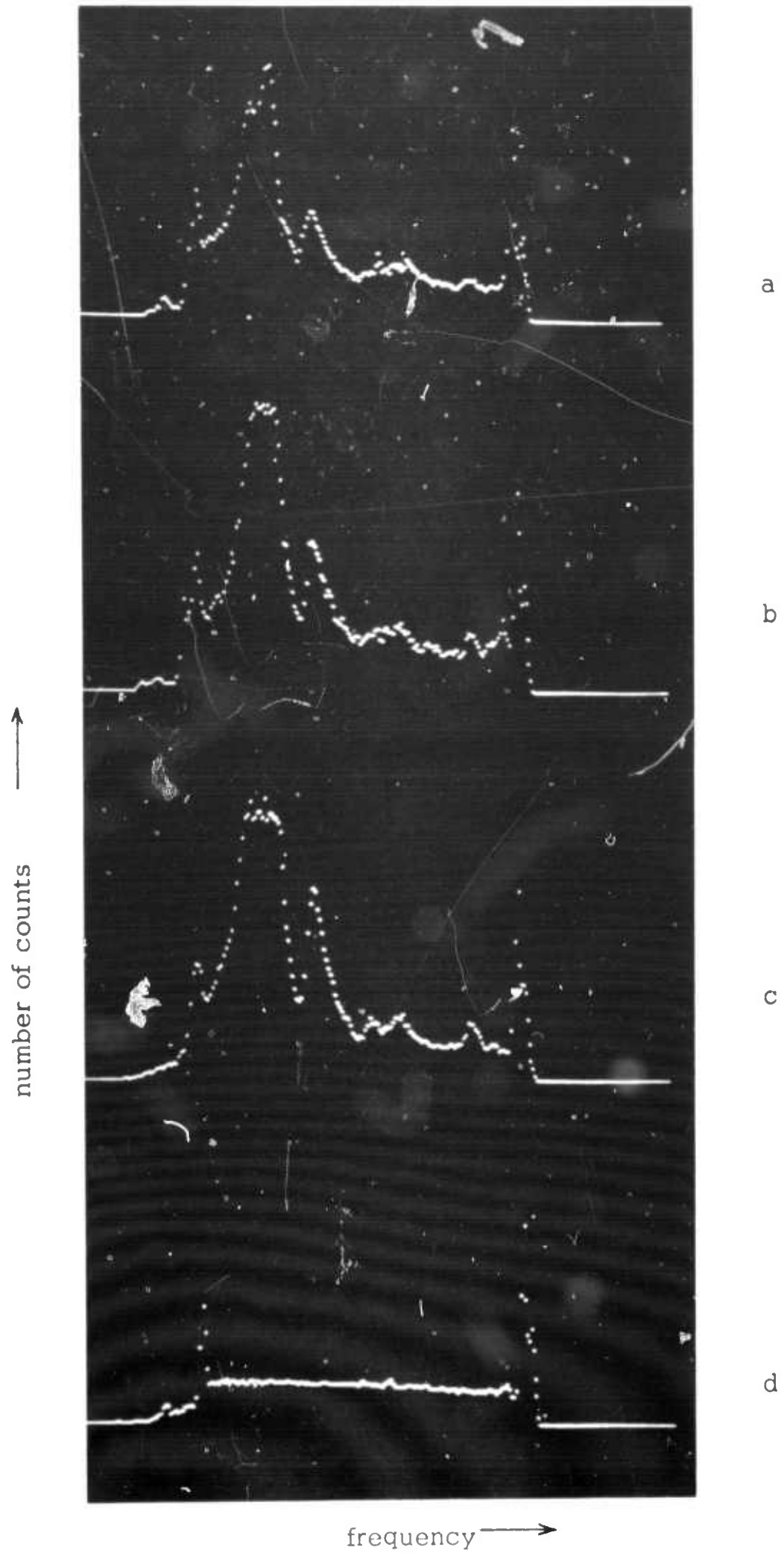


Figure 4.1 Signal return spectra recorded at three different receiver gain settings (a-c) and reference signal record (d).

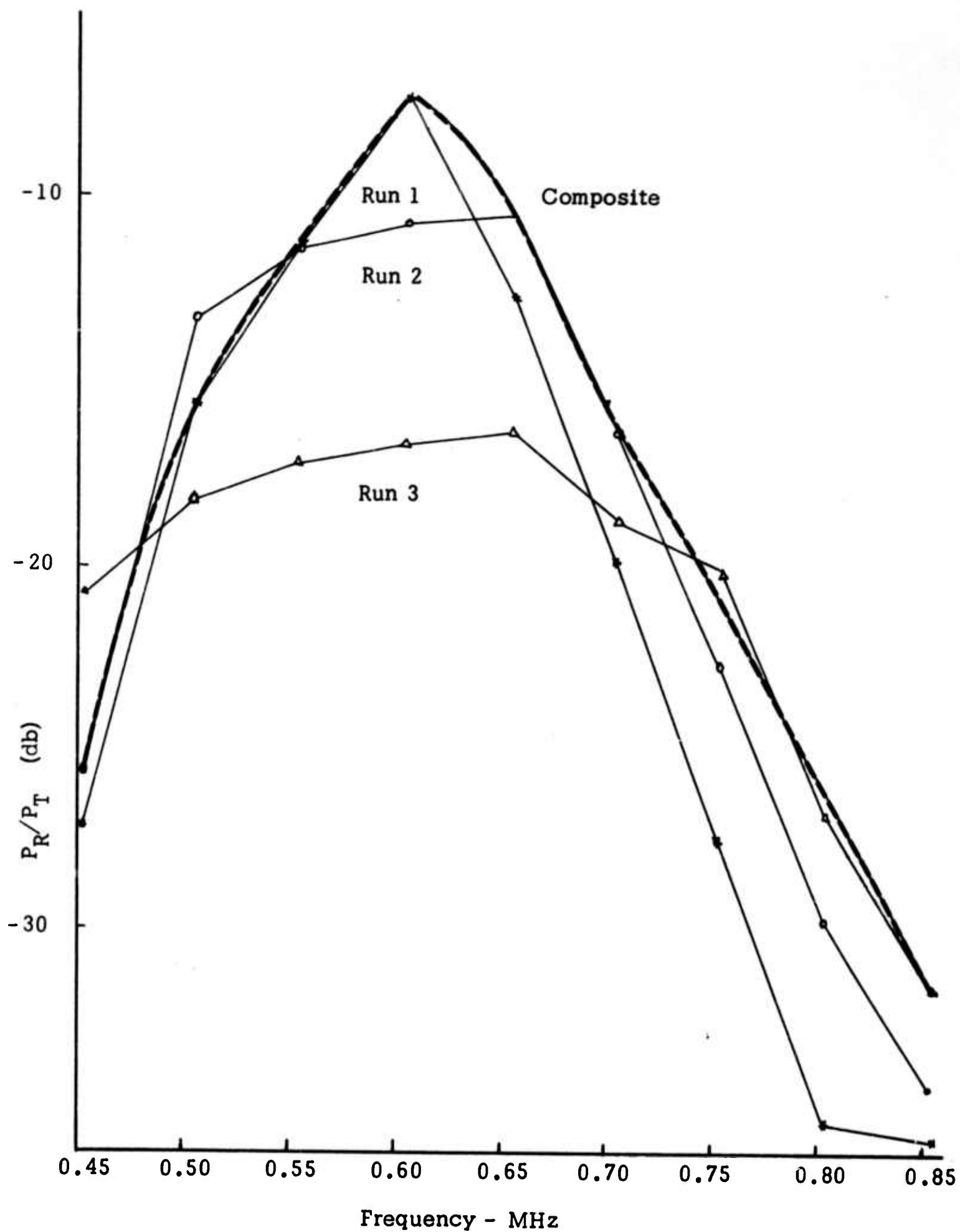


Figure 4.2 Ratio of average received power to transmitted power for different receiver gain settings to obtain composite.

was sufficiently wide to give the desired steady state condition at the extreme angle of 60° incidence. The transmitter PRF was set a 50 Hz.

The sweep rate was 5.0 seconds, hence the sample rate for each frequency was 0.2 Hz, or approximately four samples per each rotation of the target, which was sufficiently low to produce independent data points. The data were averaged for 300 seconds, i.e. 60 sweeps.

4.3 Description of the Rough Surfaces

The scattering experiment utilized two targets. The first consisted of a stationary surface of roughness that was describable mathematically and smooth enough that locally flat approximation would be valid. A second target was obtained by coating the first target with uniform diameter sand particles. This surface represents a high frequency, but discontinuous, surface component superimposed on a low frequency surface component. No attempt was made to describe this surface statistically. The objective was to introduce a reasonably sharp spike in the roughness density spectrum of a known surface.

The fundamental surface was constructed of depolymerized rubber (DPR Compound #242, DPR Corp.). This material was found to form a desirable structural rigidity and insured minimum propagation of shear waves. Tests on this material indicated its reflection coefficient to be constant over the range of frequencies used. The sand subsequently used on the surface was screened to particle sizes in range 0.595-0.825mm diameter.

The original surface was molded from a steel surface previously used by Parkins (1966) in an extensive monochromatic, bi-static experiment program. He determined the properties of the surfaces by making estimates of the probability function of the surface heights, the autocorrelation function of the surface heights as a function of lateral distances, and the stationarity of the processes. The estimates were computed from a series of sampled height measurements that were taken along profiles of the target.

The sampled height measurements were made along several profiles of the steel target mold. The profiles were separated a distance sufficient (several correlation distances) to insure independence of the data points of separate measurement runs. The probability distribution function and auto-correlation function were computed for each of these runs as well as the mean, \bar{m} , and standard deviation of heights, σ .

The estimate of the correlation function was calculated using the statistical estimator (the overbar indicates sample function)

$$C(\tau) = C(\ell \Delta x) = \frac{\frac{1}{N-\ell} \sum_{i=1}^{N-\ell} (h_i - \bar{m})(h_{i+\ell} - \bar{m})}{\frac{1}{N} \sum_{i=1}^N (h_i - \bar{m})^2} \quad (4.6)$$

where: h_i is the i^{th} height in the series of N points.

ℓ is the lag.

Δx is the sampling interval.

$$\bar{m} = \frac{1}{N} \sum_{i=1}^N h_i \text{ is the sample mean.}$$

The denominator of equation (4.6) is the sample variance, $\bar{\sigma}^2$, or the square of the sample standard deviation. The maximum lag used in the calculation of $C(\tau)$ was $N/10$ where N was made sufficiently large for the particular sampling interval used to adequately define $C(\tau)$. The criterion for the selection of the sampling interval is that it must not exceed half the period of the highest frequency present in the record of the profile. For the surface used in the experiment, the value of $\Delta x = 0.02$ inches amply satisfied this criterion. The number of points taken in the measurement was 1500 which corresponds to a record length of 30 inches. This provided a maximum lag of one inch which is sufficient to adequately define the falls of the sample auto-correlation coefficients. The sample auto-correlation coefficients computed are shown together with the sample variances of the surface in figure 4.4.

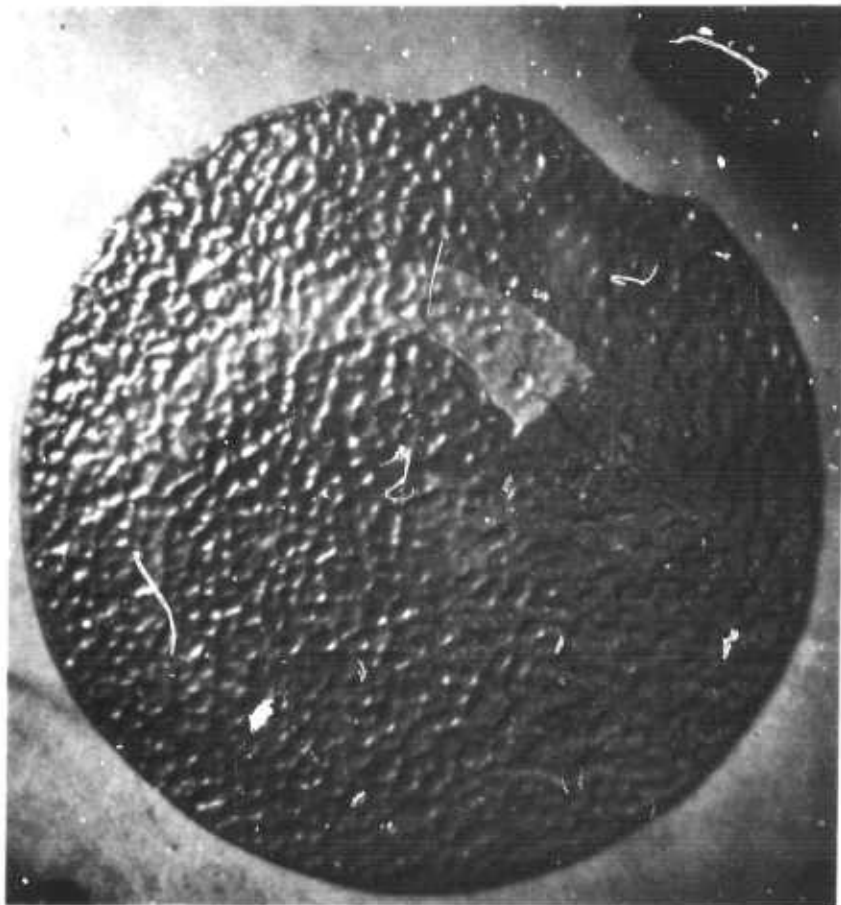


Illustration 4.2 RUBBER TARGET — FUNDAMENTAL SURFACE
(3 ft. diameter)

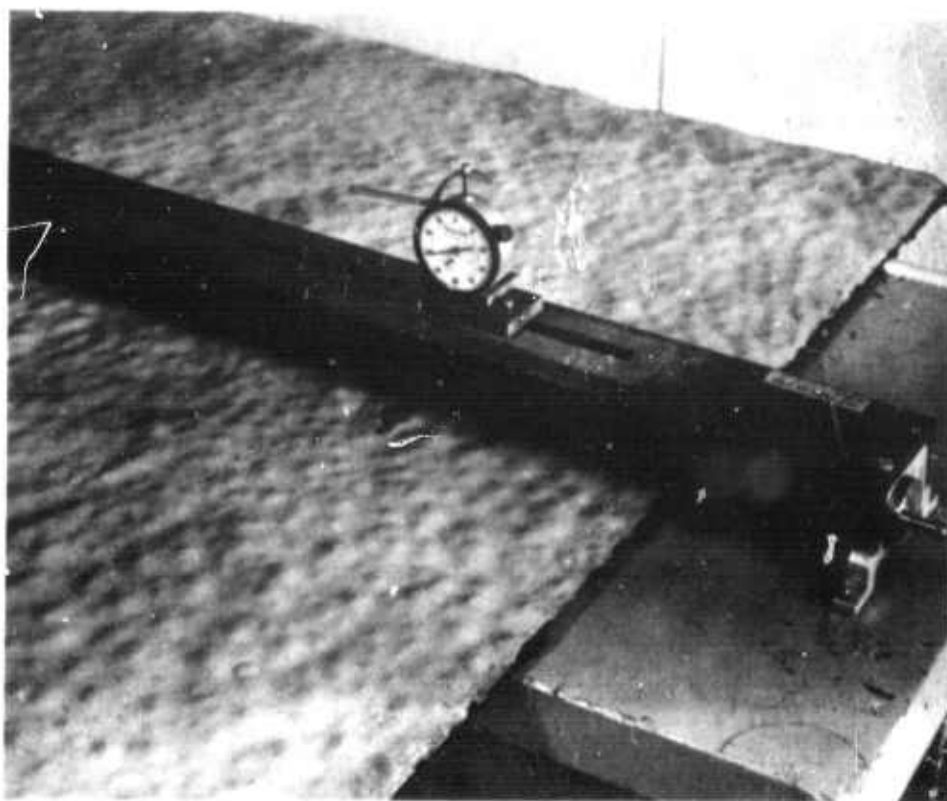


Illustration 4.3 HEIGHT GAUGE FOR MEASURING
SURFACE PROFILE

Run # 1: x $\sigma^{-2} = 0.587 \text{ mm}^2$

$$-C(\tau) = \exp \left[-\left(\frac{\tau}{17.78} \right)^2 \right]$$

Run # 2: + $\sigma^{-2} = 0.475 \text{ mm}^2$

$$-C(\tau) = \exp \left[-\left(\frac{\tau}{13.97} \right)^2 \right]$$

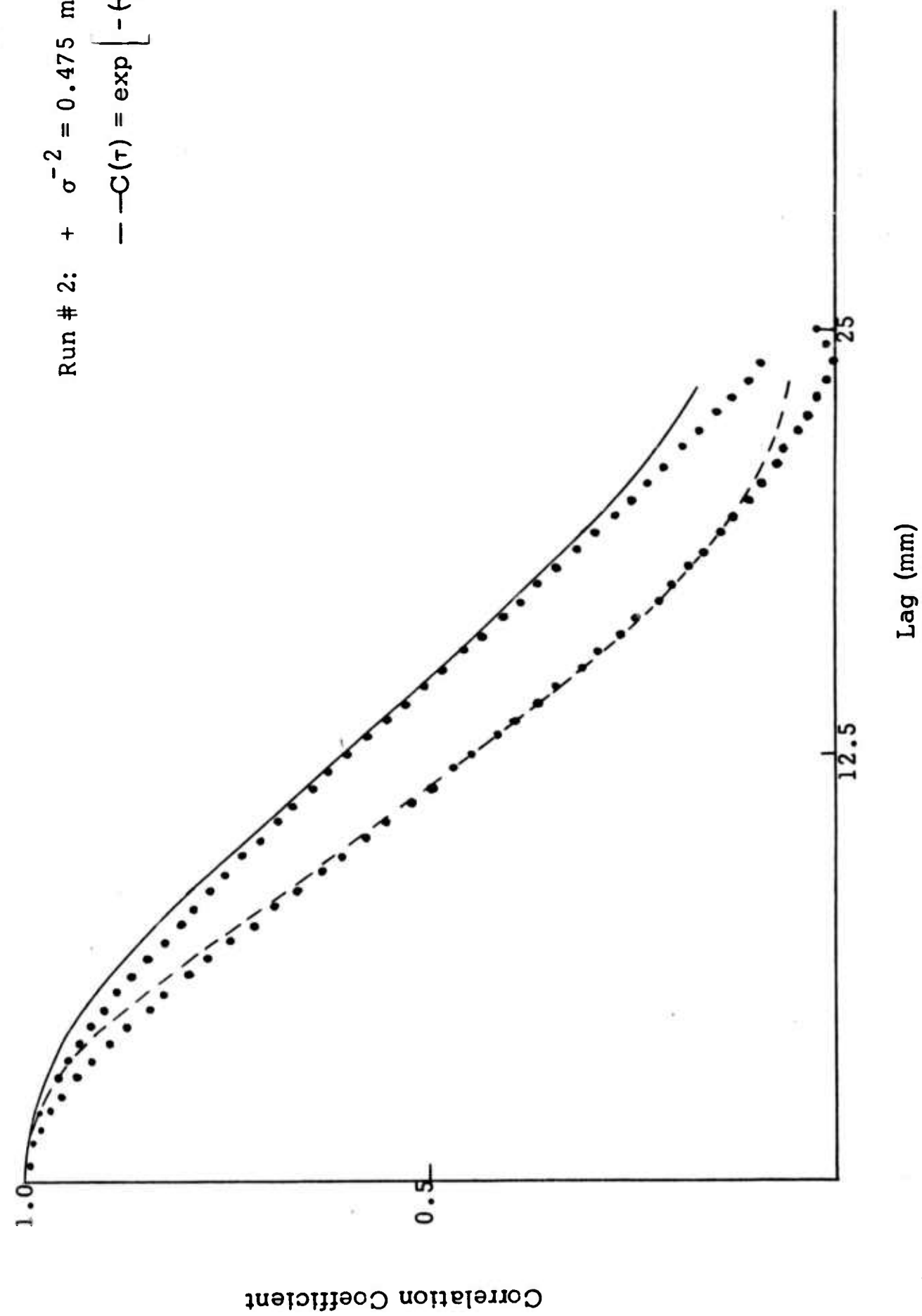


Figure 4.4 SAMPLE AUTO CORRELATION FUNCTIONS FOR FUNDAMENTAL SURFACE (Parkins 1965)

The behavior of the sample auto-correlation coefficients indicate, by the smooth falls and following rises, that the surface is gently undulating and, to a degree, periodic. It was found that near the origin the sample auto-correlation coefficient is closely approximated by the function

$$C(r) = \exp \left\{ - \left(\frac{r}{L} \right)^{3/2} \right\} \quad (4.7)$$

although this is not shown in the figure. However, away from the origin, the curve falls off more rapidly than this and a better overall approximation is the Gaussian function

$$C(r) = \exp \left\{ - \left(\frac{r}{L} \right)^2 \right\} \quad (4.8)$$

The probability distribution function of the sampled heights were determined for each of the profiles for which a sample auto-correlation function was calculated. These results are shown in figures 4.5 and 4.6 together with plots of the Gaussian distribution function

$$\Psi(h \leq H) = \int_{-\infty}^H \frac{1}{\sqrt{2\pi\sigma^2}} \exp \left\{ - \frac{(h - \bar{m})^2}{2\sigma^2} \right\} \quad (4.9)$$

obtained using for m and σ^2 values of the sample mean, \bar{m} , and the sample variance, $\bar{\sigma}^2$. Comparison of the experimental curves to those calculated shows the near-Gaussian nature of the random height process.

Run # 1: $\overline{\sigma}^2 = 0.587 \text{ mm}^2$

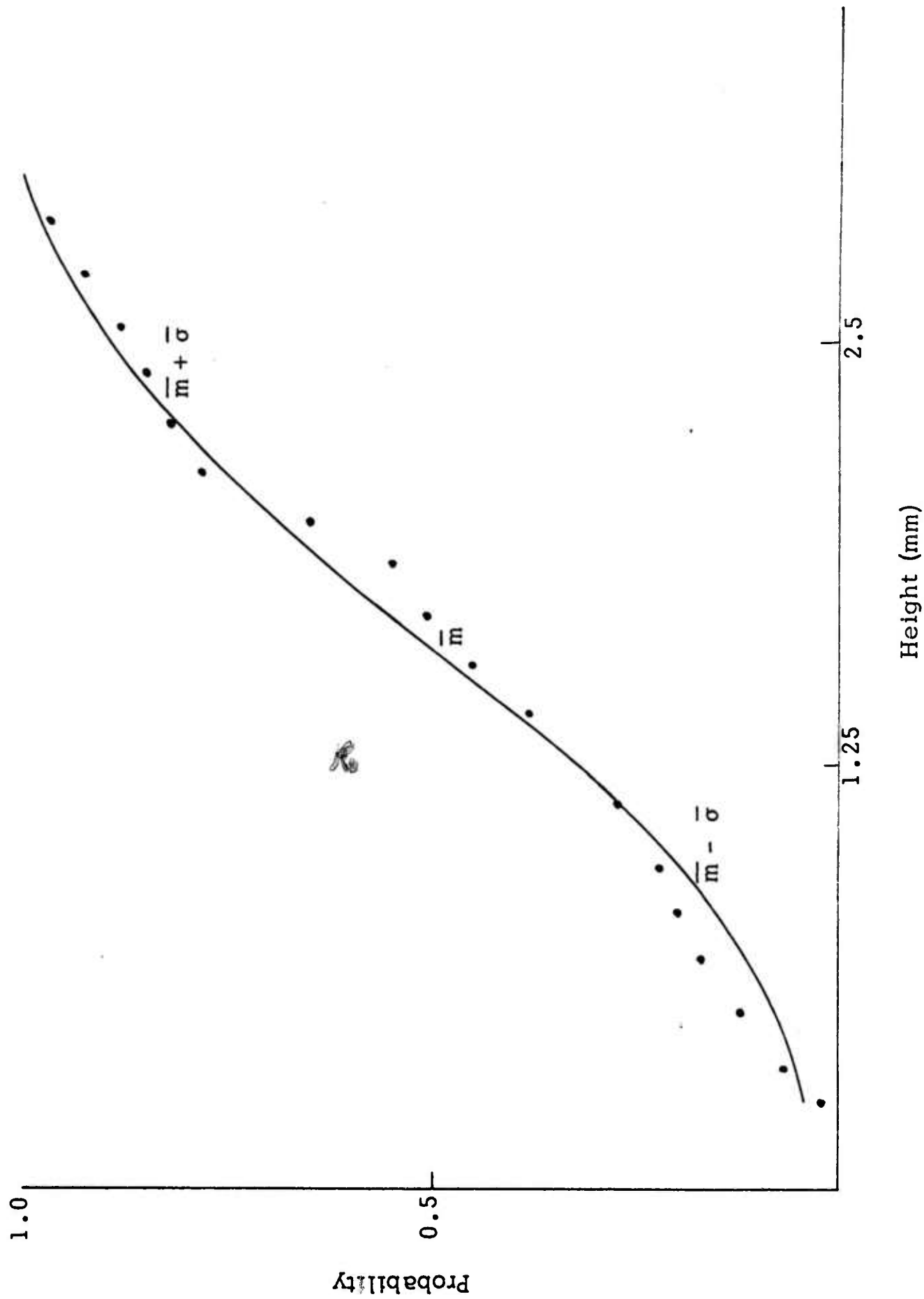


Figure 4.5 SAMPLE PROBABILITY DISTRIBUTION FUNCTION FOR FUNDAMENTAL SURFACE RUN # 1
(Parkins 1965)

Run # 2: $\sigma^2 = 0.475 \text{ mm}^2$

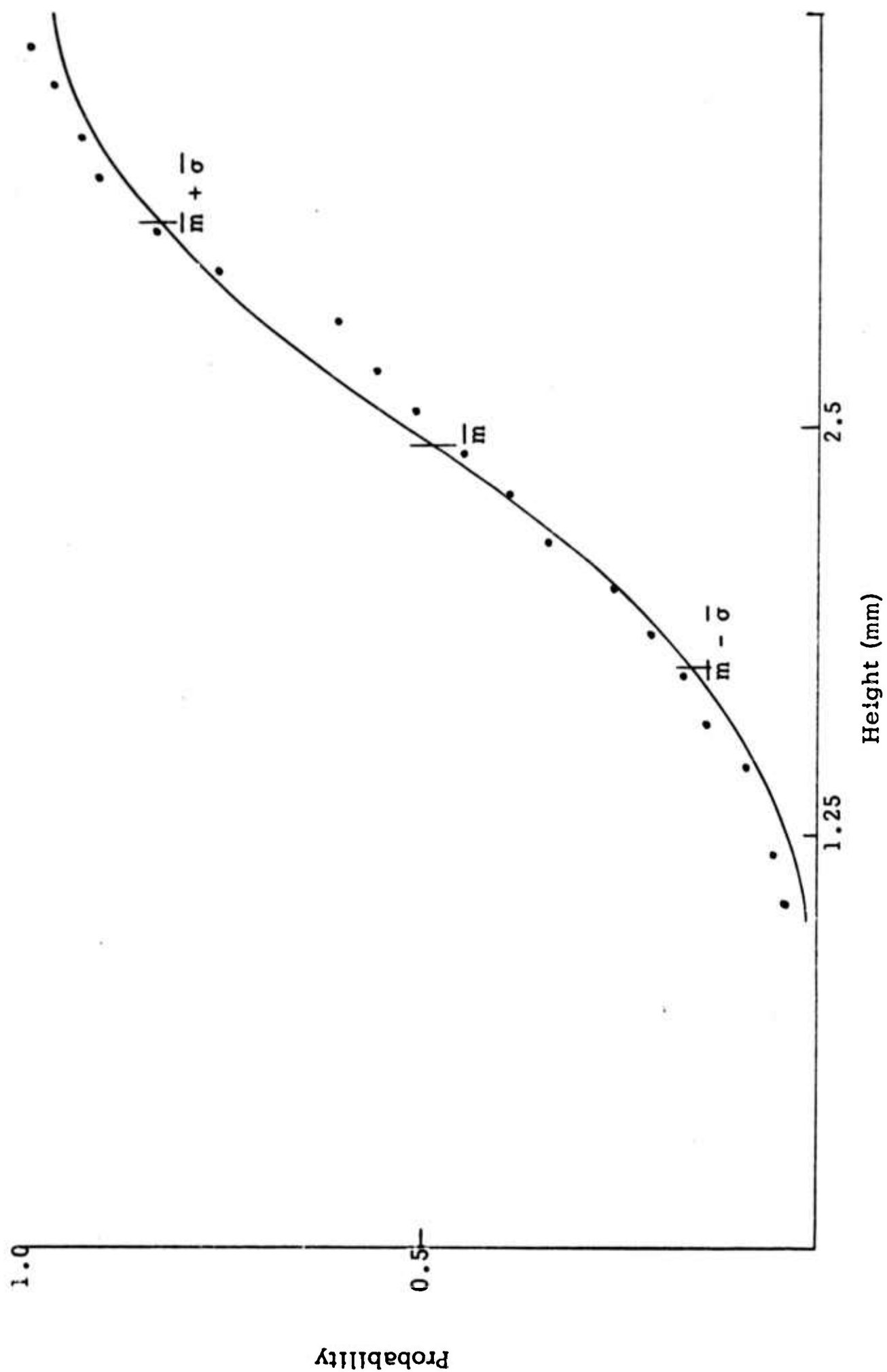


Figure 4.6 SAMPLE PROBABILITY DISTRIBUTION FUNCTION FOR FUNDAMENTAL SURFACE RUN # 2 (Parkins 1965)

4.4 Fading and Broad-Spectrum Illumination

The reradiation pattern of rough surfaces is a complex arrangement of maxima and minima that is a function of, among other things, angle of incidence of the illuminating energy. This complex pattern accounts for the phenomena termed fading. For this discussion, this will be specified as positional fading, that is, as the illuminating source is moved relative to a stationary target the return amplitude will fluxuate pulse-to-pulse. The reradiation is also a function of frequency, and definite reorientation of the reradiation lobes occurs as the frequency is changed. This experiment attempts to determine the relationship between positional fading and frequency fading.

4.4.1 Fading Experiment

This experiment consisted of recording the return from the roughened concrete floor of the water tank using a 1.5MHz transducer pair positioned at a 45° incidence angle. The transducers were mounted on the linear motion carriage and pointed broadside to the direction of travel. The return amplitudes were recorded by two methods: 1) the A-scan display was photographed on 35mm movie film on a pulse-to-pulse basis, and 2) the return amplitude was sampled and fed to the pulse-height analyzer which produced the probability density distribution of the amplitudes.

A position fading record was recorded and the probability density function obtained. This distribution is shown in Figure 4.7 and was obtained by recording the monochromatic returns for 200 seconds as the carriage moved the transducers relative to the surface at a velocity sufficient to assure pulse-to-pulse independence. The distribution shown in 4.7a is clearly Rayleigh as expected. The Rayleigh probability density function is

$$p(v) dv = \frac{2v}{\langle v^2 \rangle_{\text{avg}}} \exp\left(\frac{-v^2}{\langle v^2 \rangle_{\text{avg}}}\right) dv, \quad v > 0$$

where v = voltage

In 4.7b-e the system receiver gain was increased to observe the effect of increased $(v^2)_{ave}$ and to confirm that the fading was definitely Rayleigh.

A frequency fading record was recorded and the probability density function obtained. This distribution is shown in Figure 4.8 for four ranges of frequency sweep. The carriage is stationary for this measurement. In general no indication is given that the distribution is Rayleigh or Gaussian. The Rayleigh nature of the distribution shown in 4.8d is misleading. Due to the frequency response curve of the transducers, the average return decreases as the frequency sweep range is increased, hence, a nonlinear weighing is introduced that increases the predominance of low amplitude signals. In figure 4.9a-c are shown three distributions each obtained with the same frequency sweep range but at three different set positions (approximately 1 inch apart) along the track. These distributions verify that the surface is not uniformly rough (this is confirmed by observation of the trowel markings on the concrete surface).

A position-plus-frequency fading record was obtained by using a frequency swept transmitted signal and recording the amplitudes for 200 seconds as the carriage moved relative to the surface. This record is shown in Figure 4.10b. and compared with the distribution for positional fading alone (4.10a.). There is essentially no change due to adding frequency diversity. This result was confirmed by employing several carriage velocities, pulse-rate frequencies, and sweep widths. That is, the probability density distribution of the pulse-to-pulse fading of return from an area extensive rough surface is unchanged by the fact that each pulse is at a different frequency, at least for reasonable frequency ranges, e.g. ± 20 per cent from center. Although it could not be confirmed it is believed that this contention will hold for even much broader spectrum illumination.

However, even though the pulse-to-pulse fading distribution is unaffected, the scan-to-scan distribution is greatly altered. That is if the average return for each scan is compared with the monochromatic pulse-to-pulse return it would be seen that their distributions are considerably different and that the scan-to-scan fading distribution has a much smaller variance. Unfortunately, the system does not include the capability of

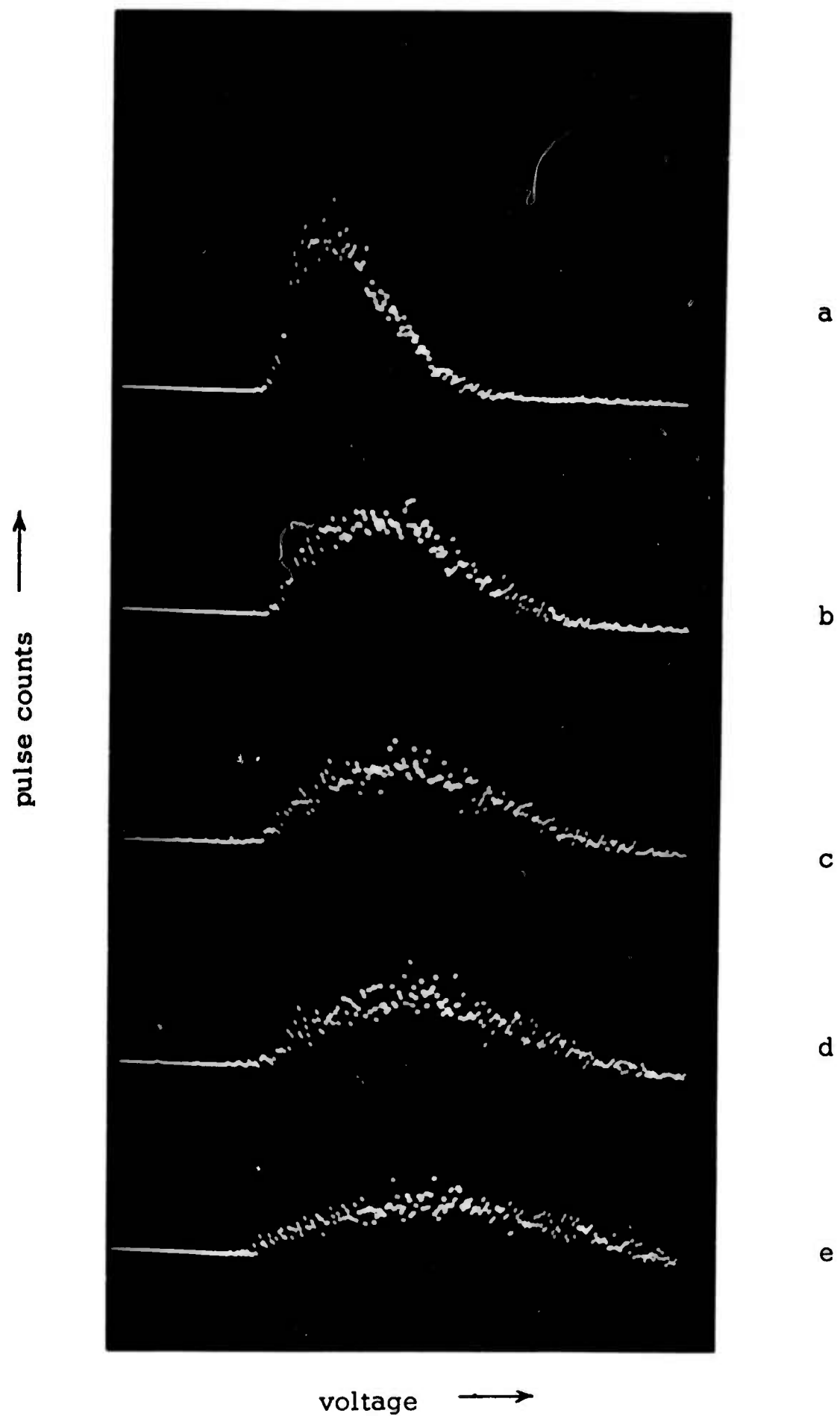


Figure 4.7 Positional fading probability distributions recorded at different receiver gain settings.

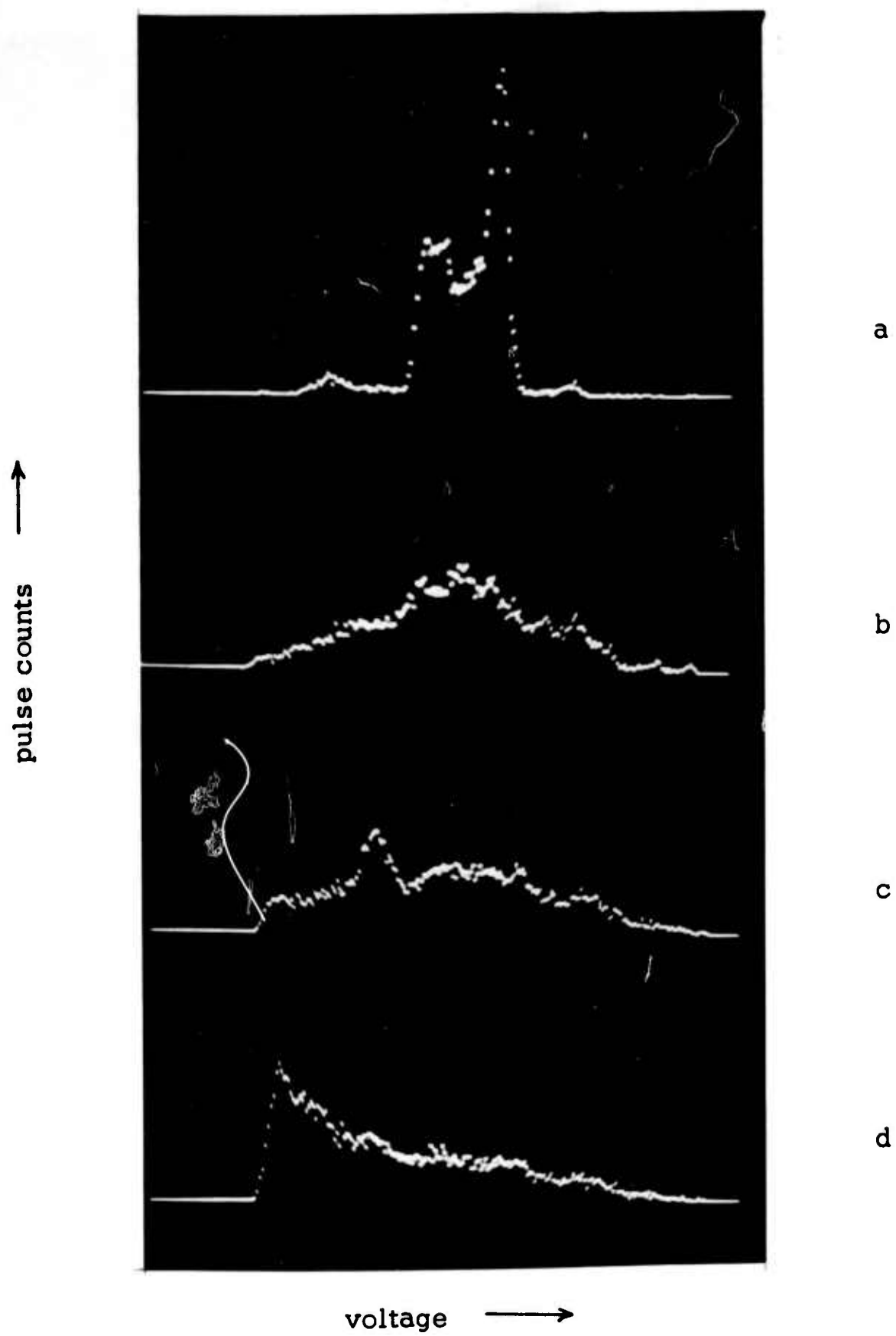


Figure 4.8 Frequency fading probability distributions for four ranges of transmitted spectrum width.

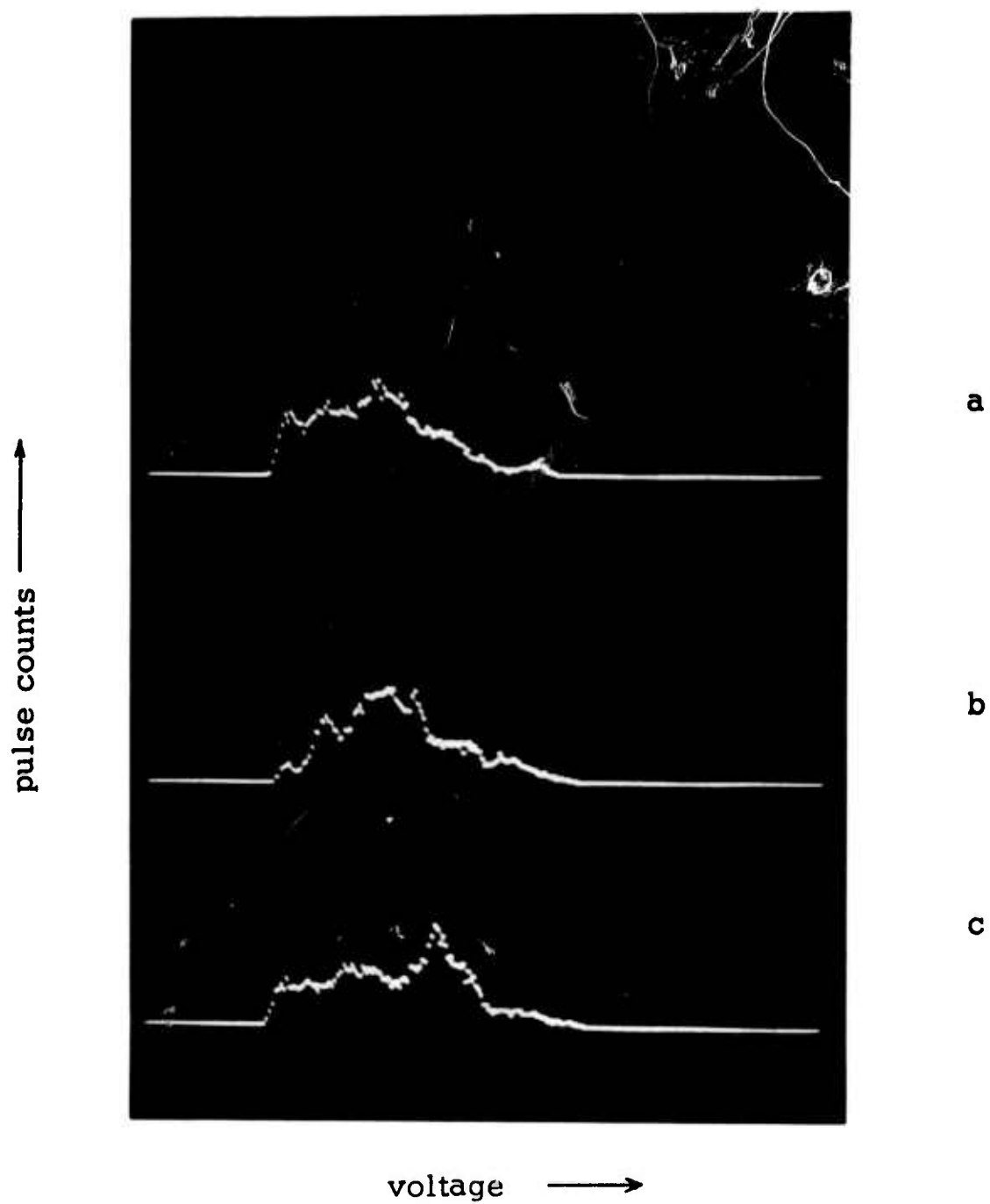


Figure 4.9 Frequency fading probability distributions recorded at different positions .

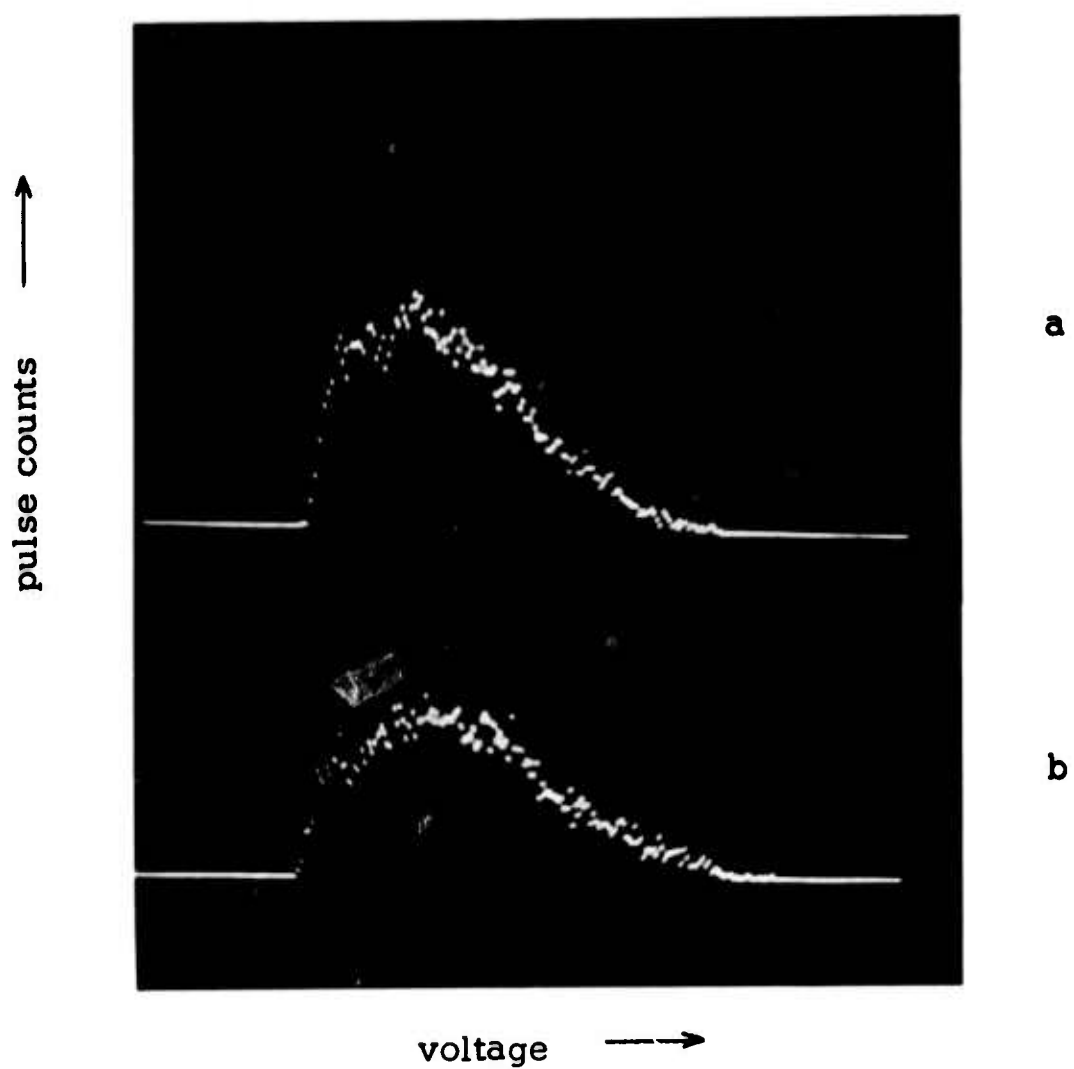


Figure 4.10 Positional fading probability distribution (a) and frequency-plus-positional fading probability distribution (b).

automatically producing the scan-to-scan fading distribution. To verify the contention, the return was photographically recorded and the averages computed manually. The sweep time was set to be less than the interpulse period of the monochromatic record, hence the time between pulses of the same frequency is the same in both the monochromatic and sweep frequency records. The pulse-to-pulse monochromatic fading records had a mean of 6.83 volts and a variance of 2.967 volts. The scan-to-scan swept frequency (with moving carriage) had a mean of 6.48 volts and a variance of only .545 volts.

4.5 Acoustic-Electromagnetic Analogy

Acoustic model experiments have been used extensively to study a variety of electromagnetic problems. The validity of such modelling experiments depends on the validity of the analogy of the acoustic model to the electromagnetic model. The bounds on analogue will be discussed in general terms. A complete description of acoustic modeling techniques used for radar backscatter is contained in the dissertation by Edison (1961). A detailed examination of the acoustic-electromagnetic analogy for scattering from rough surfaces meeting the conditions for application of the Kirchhoff approximation is presented in the dissertation by Parkins (1966).

The analogy between electromagnetic waves in air and acoustic waves in water, is easily seen by examining the differential equations in each case. The "telegraphers equations" describing acoustic and electromagnetic plane waves traveling in the z direction are:

Acoustic	Electromagnetic
$\frac{\partial p}{\partial z} = -\rho_v \frac{\partial u_z}{\partial t}$	$\frac{\partial E_x}{\partial z} = -\mu \frac{\partial H_y}{\partial t}$
$\frac{\partial u_z}{\partial z} = -k \frac{\partial p}{\partial t}$	$\frac{\partial H_y}{\partial z} = \epsilon \frac{\partial E_x}{\partial t}$

where: ρ = the acoustic pressure

μz = the particle velocity in the z direction

v = the mass density of the acoustic medium per unit volume

K = the compressibility of the acoustic medium

H = the magnetic field

E = the electric field

μ = the permeability of the electromagnetic medium

ϵ = the permittivity of the electromagnetic medium

The electromagnetic equations are recognized simply as expressions of Faraday's Law and Ampere's Law respectively. Combining the two equations in each case yields wave equations of the form

Acoustic	Electromagnetic
$\frac{\partial^2 \rho}{\partial z^2} = \frac{1}{c_w^2} \frac{\partial^2 \rho}{\partial t^2}$	$\frac{\partial^2 E_x}{\partial z^2} = \frac{1}{c_a^2} \frac{\partial^2 E_x}{\partial t^2}$
$\frac{\partial^2 \mu_z}{\partial z^2} = \frac{1}{c_w^2} \frac{\partial^2 \mu_z}{\partial t^2}$	$\frac{\partial^2 H_y}{\partial z^2} = \frac{1}{c_a^2} \frac{\partial^2 H_y}{\partial t^2}$

where: c_w = the velocity of the acoustic wave in water

c_a = the velocity of the electromagnetic wave in air

Since identical equations are obeyed by both the acoustic and electromagnetic waves, the solutions are likewise identical and the analogy is valid for plane waves in their respective media.

The boundary conditions in each of the two systems determine if the analogy may be extended to cover the reflection and scattering of the waves at an interface. The boundary conditions are:

Acoustic	Electromagnetic
$\rho_1 = \rho_2$	$E_{t_1} = E_{t_2}$
$\mu_{n_1} = \mu_{n_2}$	$H_{t_1} = H_{t_2}$

where n refers to the normal component and t refers to the tangential component; 1 and 2 refer to media on opposite sides of an interface. The electromagnetic expressions show the familiar condition that the tangential components of E and H are continuous across a boundary. The acoustic portions express the less familiar, but reasonable condition, that in an ideal fluid, the pressure on both sides of a boundary must be equal and that the normal component of velocity must be continuous across the boundary.

Only the scalar form of the electromagnetic wave equation has been used. This is in fact the only form of the equation that may be used for the analogy, for the acoustic equation must be scalar due to the scalar nature of pressure. The limitations of the analogy due to this fact may be seen from further examination of the boundary conditions. If it is assumed that the electromagnetic wave is linearly polarized one may choose the analogy such that the boundary conditions are the same in either system. Thus the equations are correct for horizontal polarization with pressure analogous with electric field and velocity analogous with magnetic field. By interchanging the roles of E and H in the equations an analogy of pressure with magnetic field and velocity with electric field is obtained. The boundary conditions for this analogy will hold only for vertical polarization.

CHAPTER 5

RESULTS OF SCATTERING EXPERIMENT

The scattering experiment consisted of the measurement of backscatter from two statistically rough surfaces. The fundamental surface was gently undulating surface having slopes large relative to the incident wavelength. The other surface was produced by adding sand particles to the fundamental surface. As shown by the results, the effect of superimposing small scatterers onto the fundamental surface was to convert the frequency dependent scattering coefficient curve from a negative slope to a positive slope. An attempt was made to explain this and other behavioral characteristics and to relate the results to theoretical predictions of frequency dependence.

The experiment results presented in this chapter were recorded as described in Chapter 4 and, to the degree possible by repetitive measurements, are considered to be accurate to within equipment tolerances. Data that could not be repeated were not included in the results. These include a sharply rising behavior of the scattering coefficient curve in the region 2.5 MHz to 3.0 MHz discovered in the measurement of the fundamental surface, which could not be checked due to subsequent malfunction of the transducer pair used in this frequency region. This malfunction, and the unreliable behavior of the 0.3 MHz to 0.1 MHz region of the low-frequency transducer pair, restricted the range of the available data.

5.1 Measurement Results of Fundamental Surface

The behavior of the scattering coefficient as a function of frequency for the fundamental, gently undulating rough surface is shown in figures 5.1 through 5.5 at incidence angles of 0° , 15° , 30° , 45° and 60° . Figure 5.6 shows all the curves plotted together.

The curves show two behavioral regions; one below and one above about 1.25 MHz ($\lambda = 1.2\text{mm}$). In the region below 1.25 MHz the 0° and

15° data have a negative slope which increases above 1.25 MHz. For 30°, 45°, and 60° the lower frequency region, at least down to 0.5 MHz ($\lambda = 3.0\text{mm}$), the slope is approximately zero. Below 0.5 MHz a positive slope is suggested, especially at 45° and 60°, however the confidence level of these data is not as high as that above 0.5 MHz.

The region above 1.25 MHz has a pronounced negative slope for all angles. This slope is confirmed to 2.5 MHz ($\lambda = 0.6\text{mm}$) and is believed to continue to higher frequencies, however some measurements indicated a rapid change to a large positive slope in the region above 2.5 MHz. These measurements could not be confirmed and no physical explanation was found for such a behavior, therefore the data were discarded.

The data were also plotted as a function of angle for several discrete frequencies in figure 5.7. The plots indicate a greater negative slope near vertical for the low frequencies with a gradual flattening out to about 1.2 MHz ($\lambda = 1.2\text{mm}$). Thereafter the plots hold approximately the same shape but gradually drop in overall amplitude.

5.2 Measurement Results of Sanded Surface

The frequency dependence of the scattering coefficient measured for the fundamental surface densely coated with 0.595-0.825 mm sand particles are shown in figures 5.8 through 5.12 at incidence angles of 0°, 15°, 30°, 45°, and 60°. Figure 5.13 shows all curves plotted on the same graph.

As in the case of the fundamental surface, these data exhibit different behavior in two frequency regions. In the region below 1.25 MHz the curves have a positive slope of approximately the same magnitude for all angles. Above 1.25 MHz the data tend to become frequency independent. There was some support for defining a third region above about 2.0 MHz ($\lambda = 0.75\text{mm}$) where the data exhibit a positive slope such as was found for the fundamental surface. Unfortunately this could not be confirmed due to the malfunction of the transducer pair used in this region.

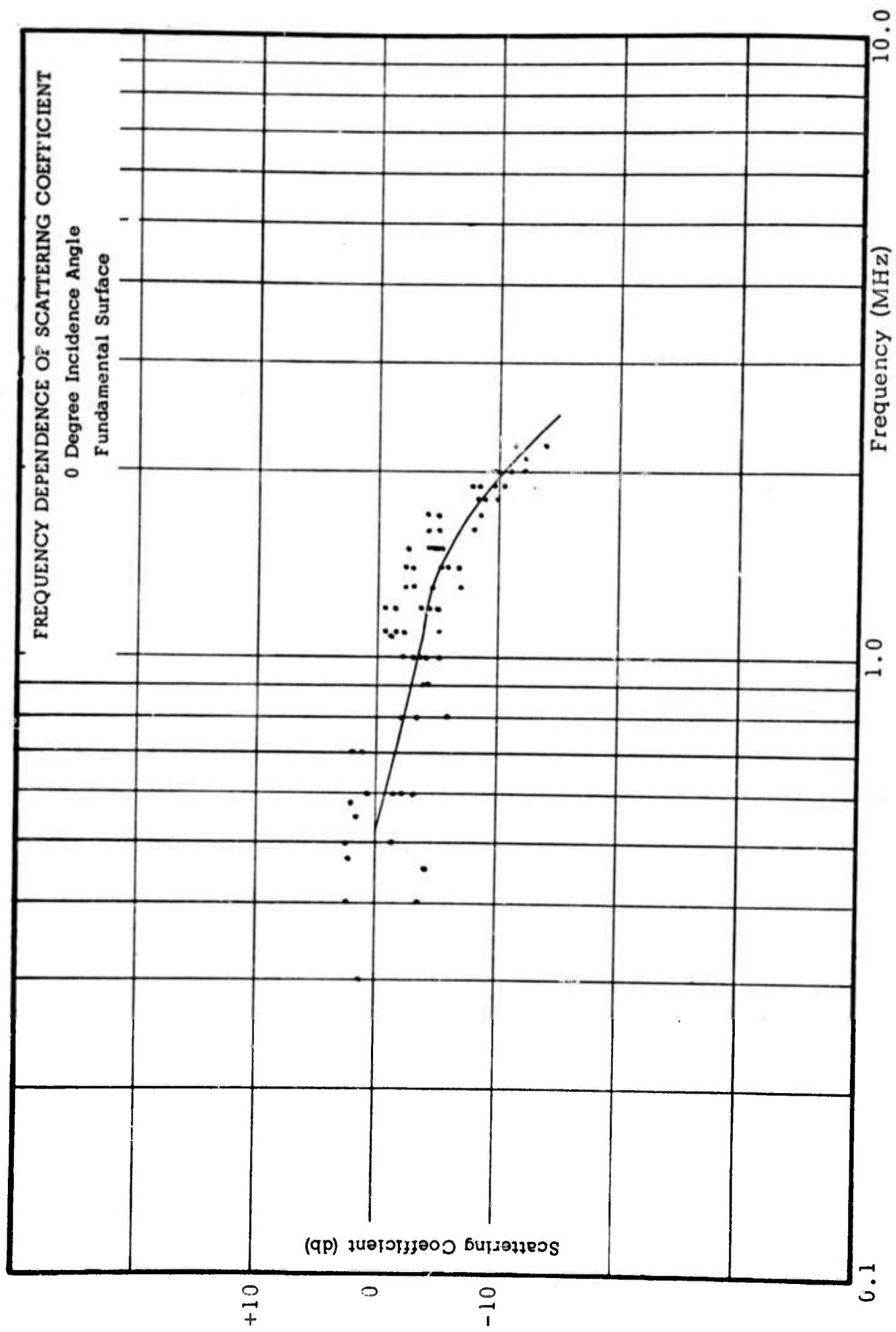


Figure 5.1

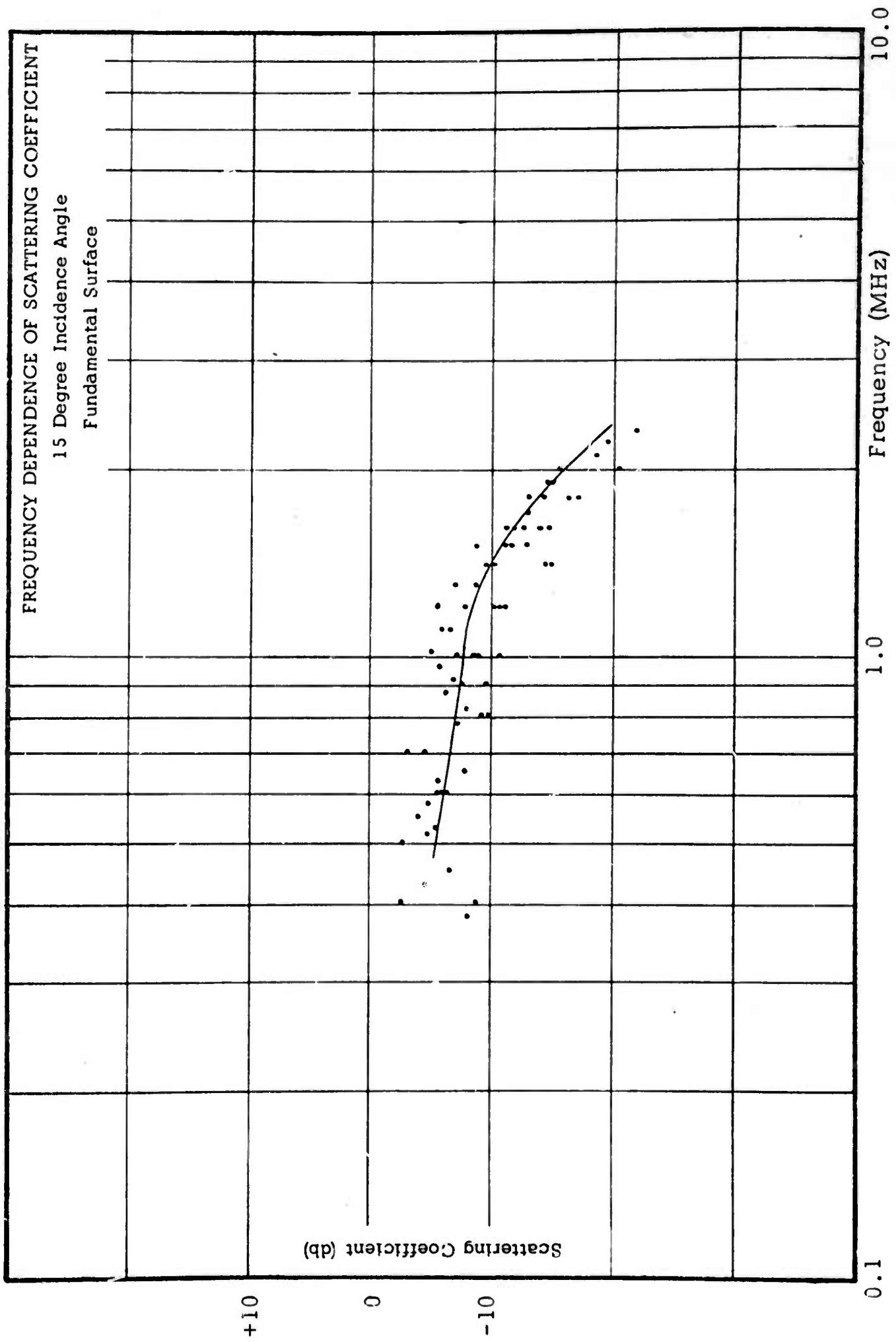


Figure 5.2

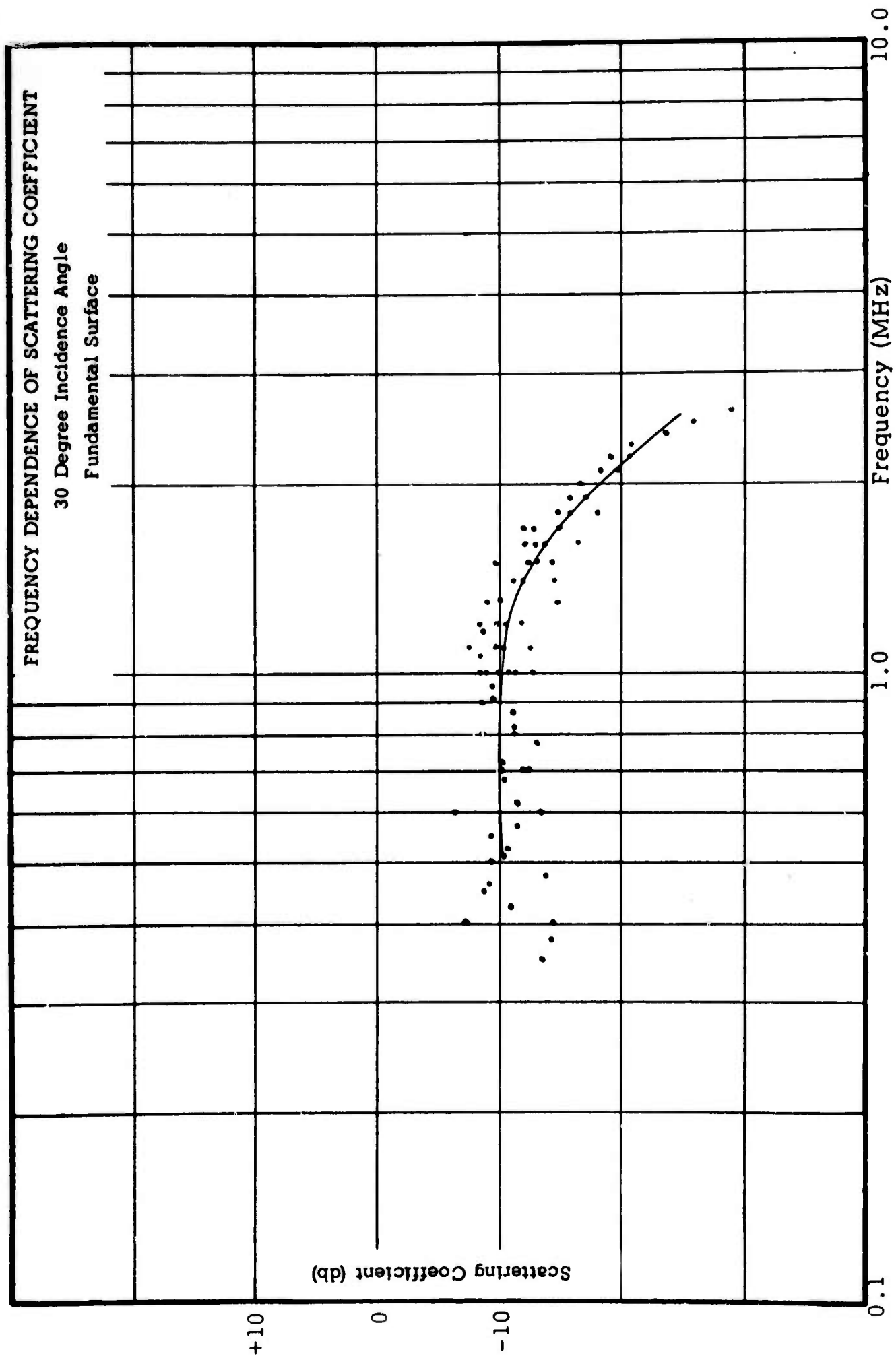


Figure 5.3

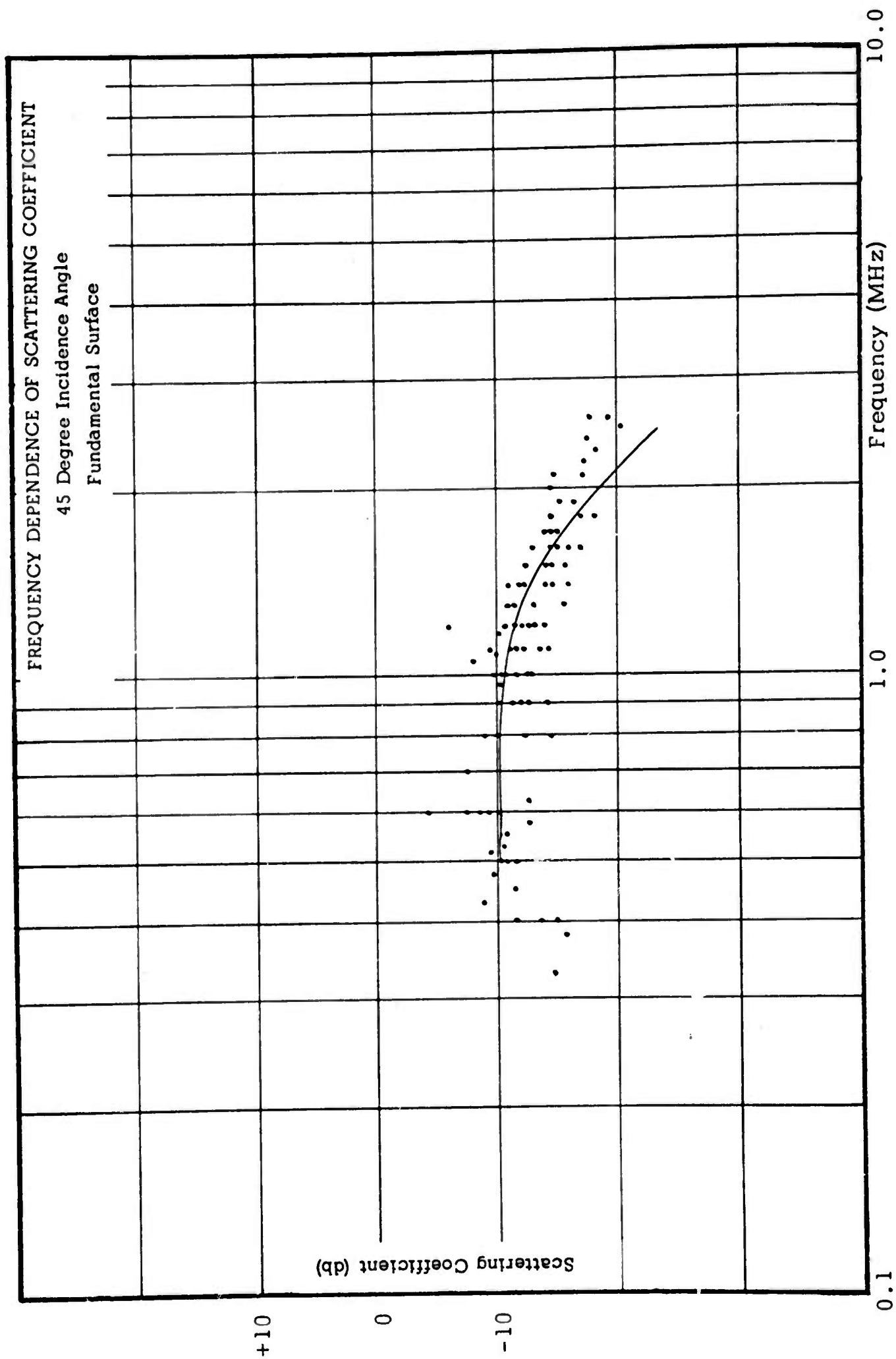


Figure 5.4

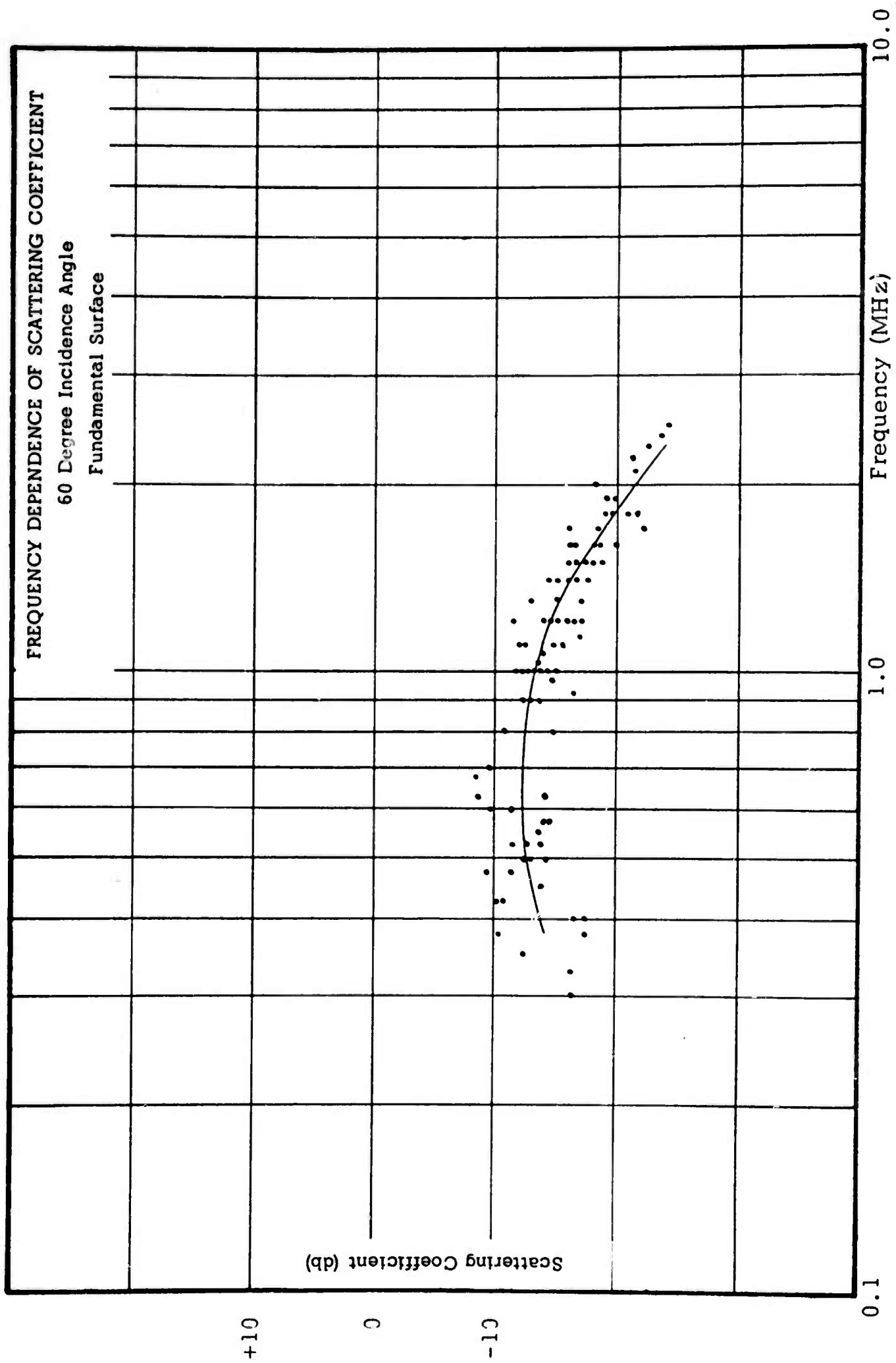


Figure 5.5

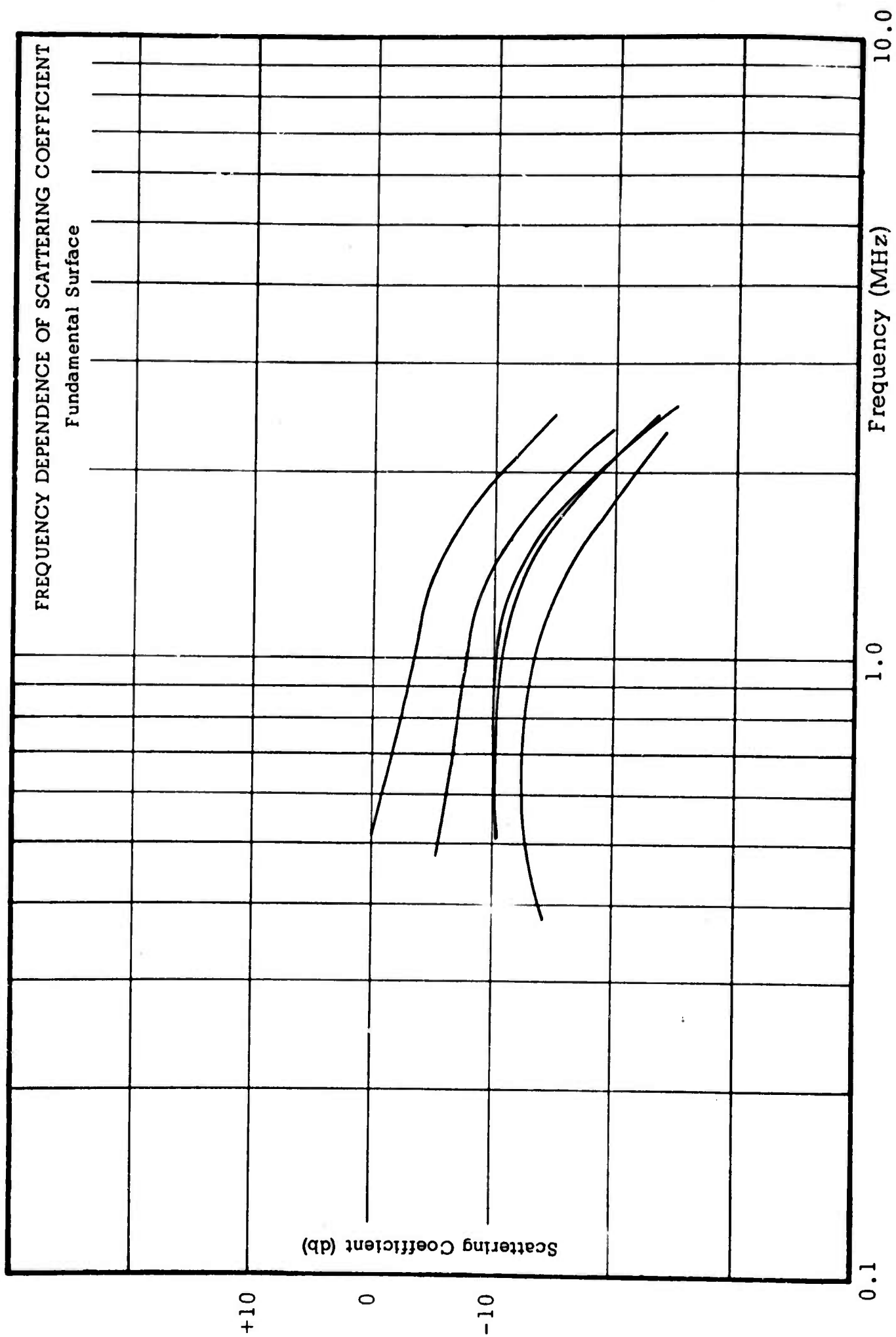


Figure 5.6

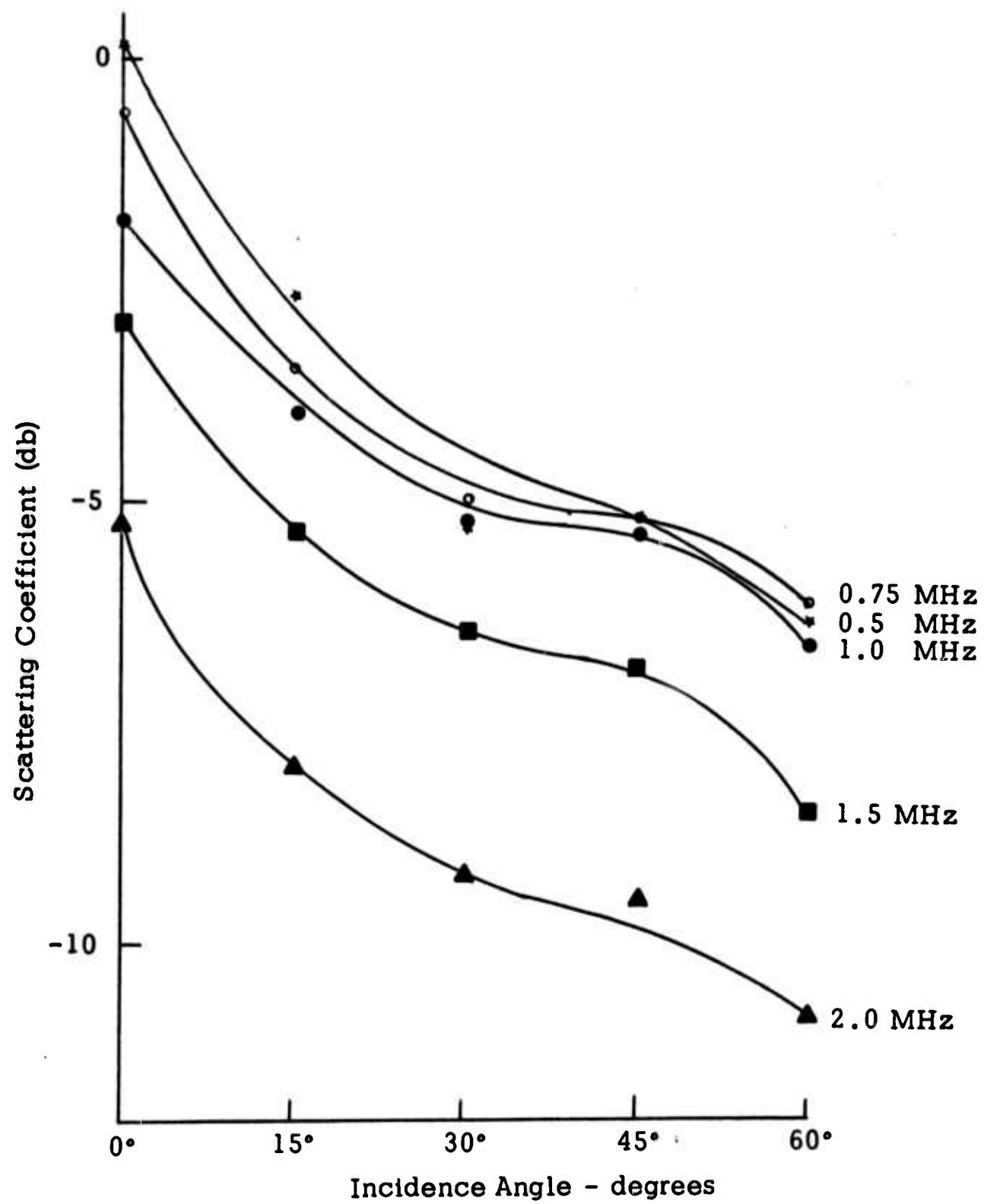


Figure 5.7 Variation of scattering coefficient with angle and frequency - fundamental surface.

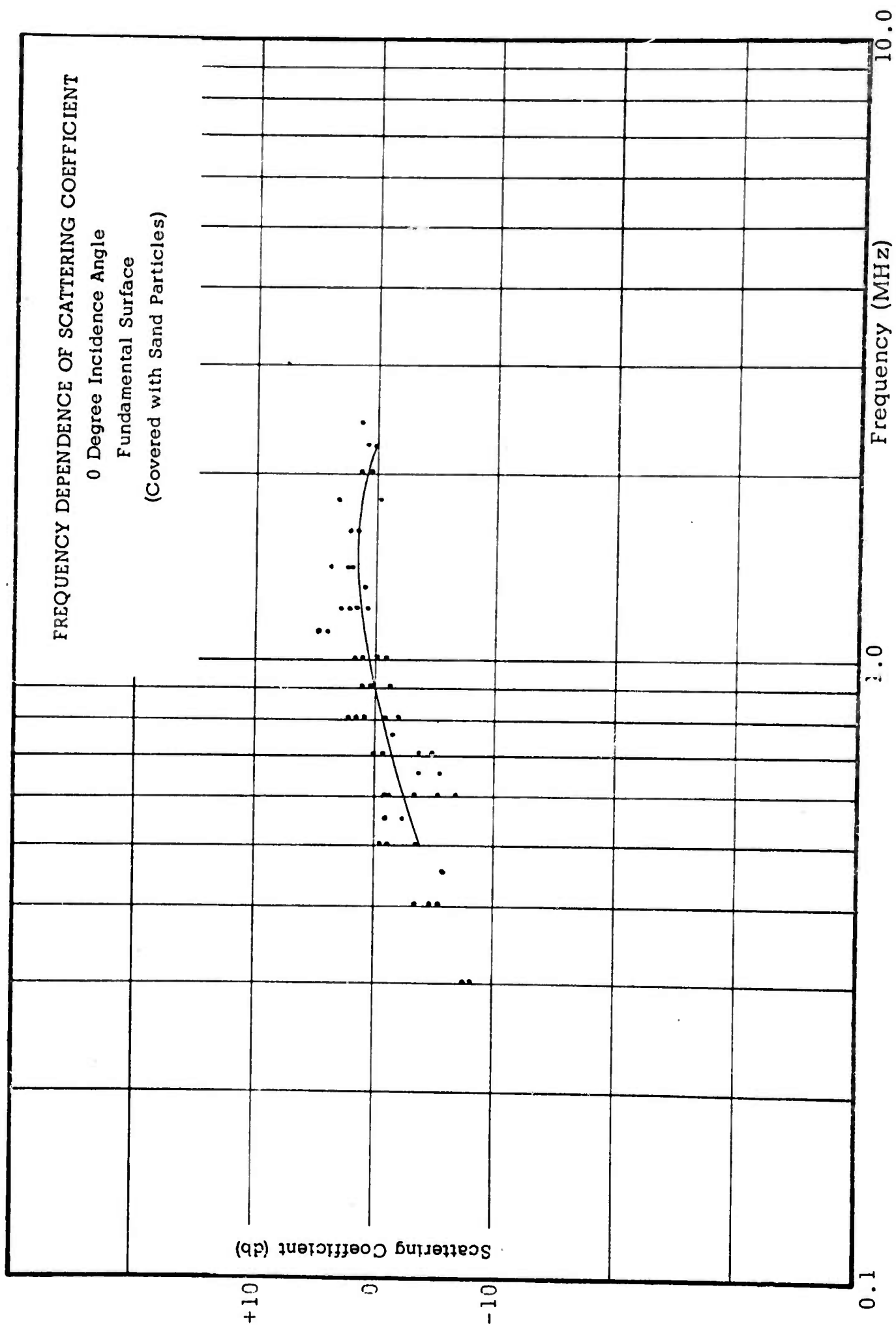


Figure 5.8

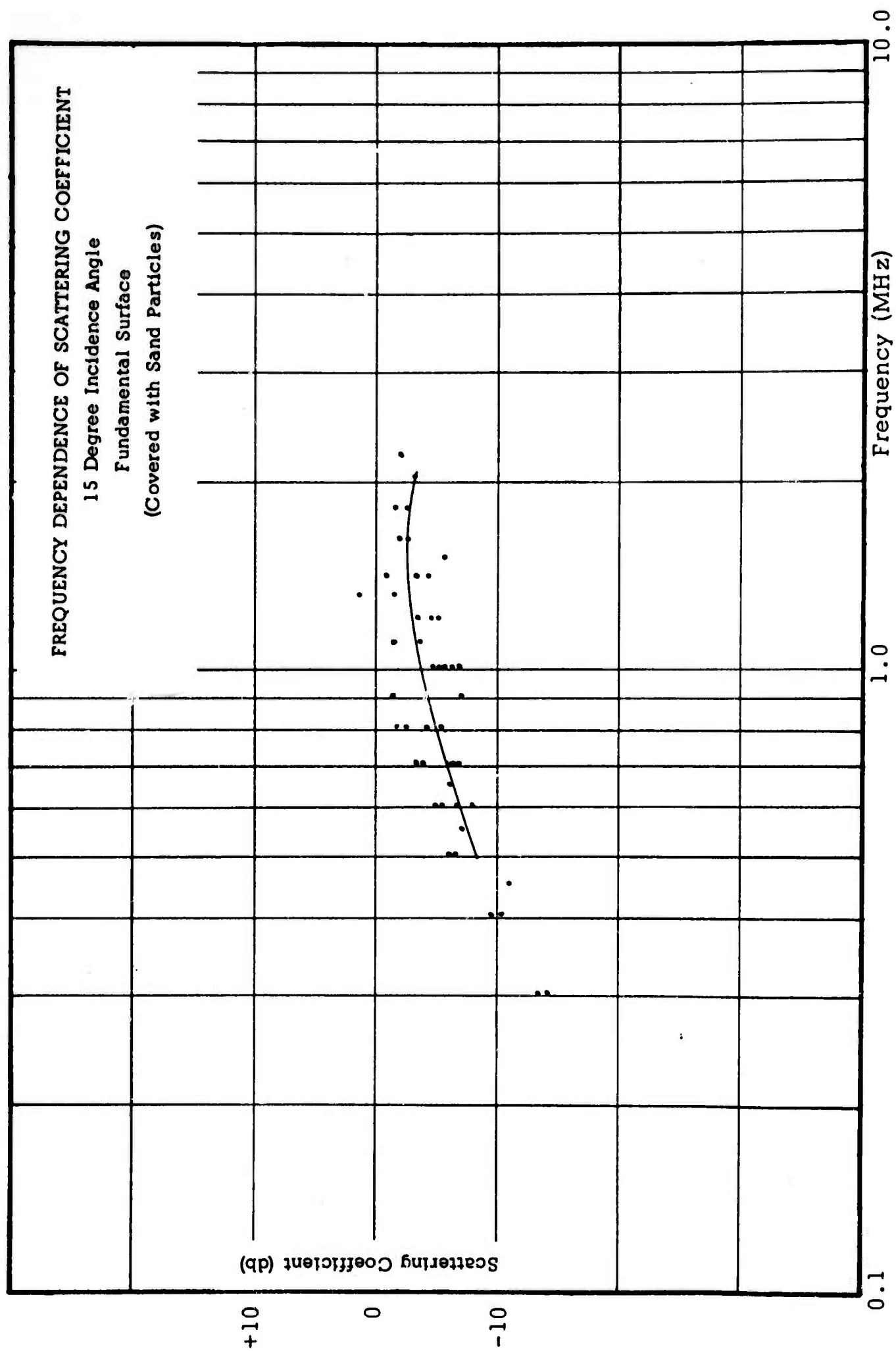


Figure 5.9

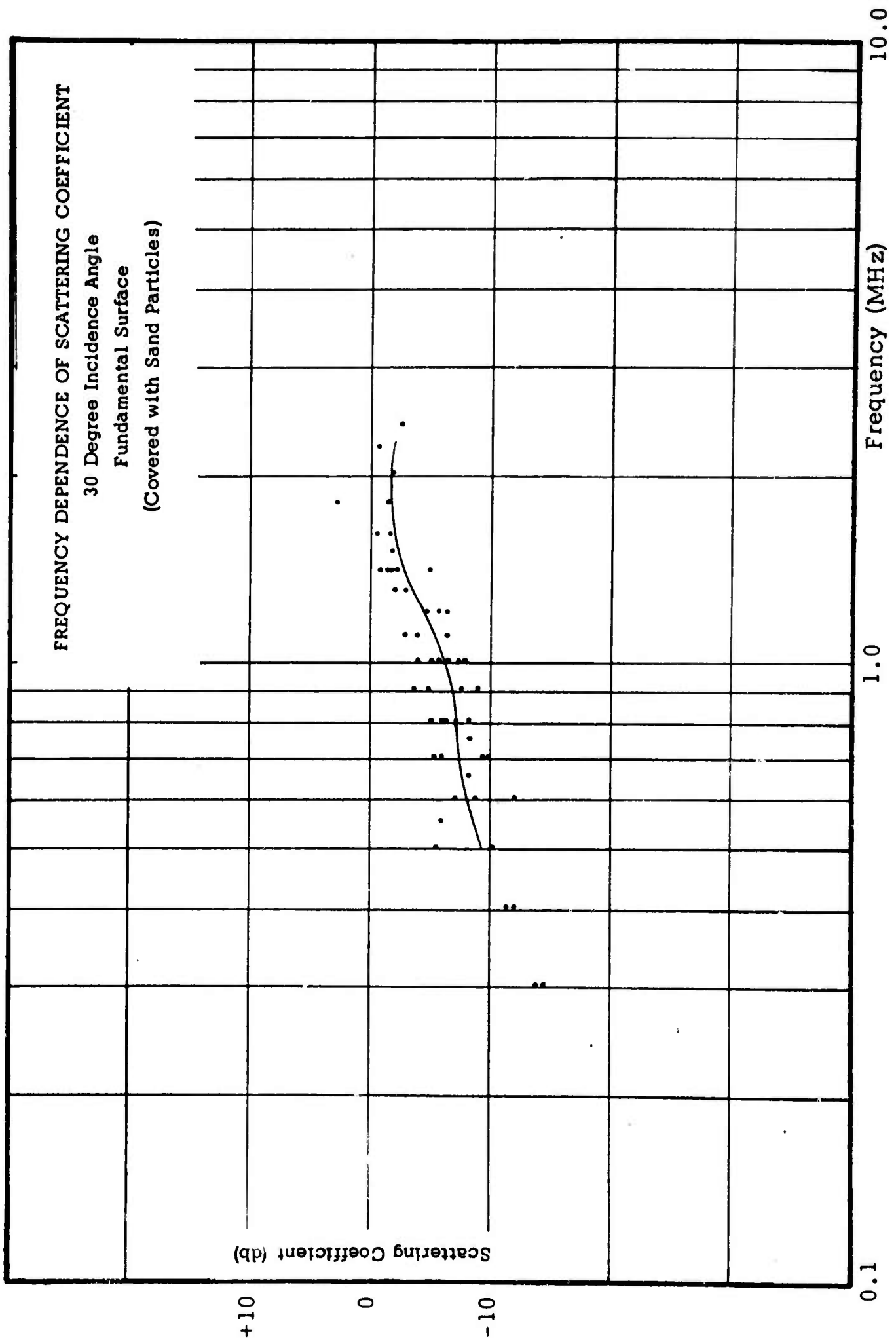


Figure 5.10

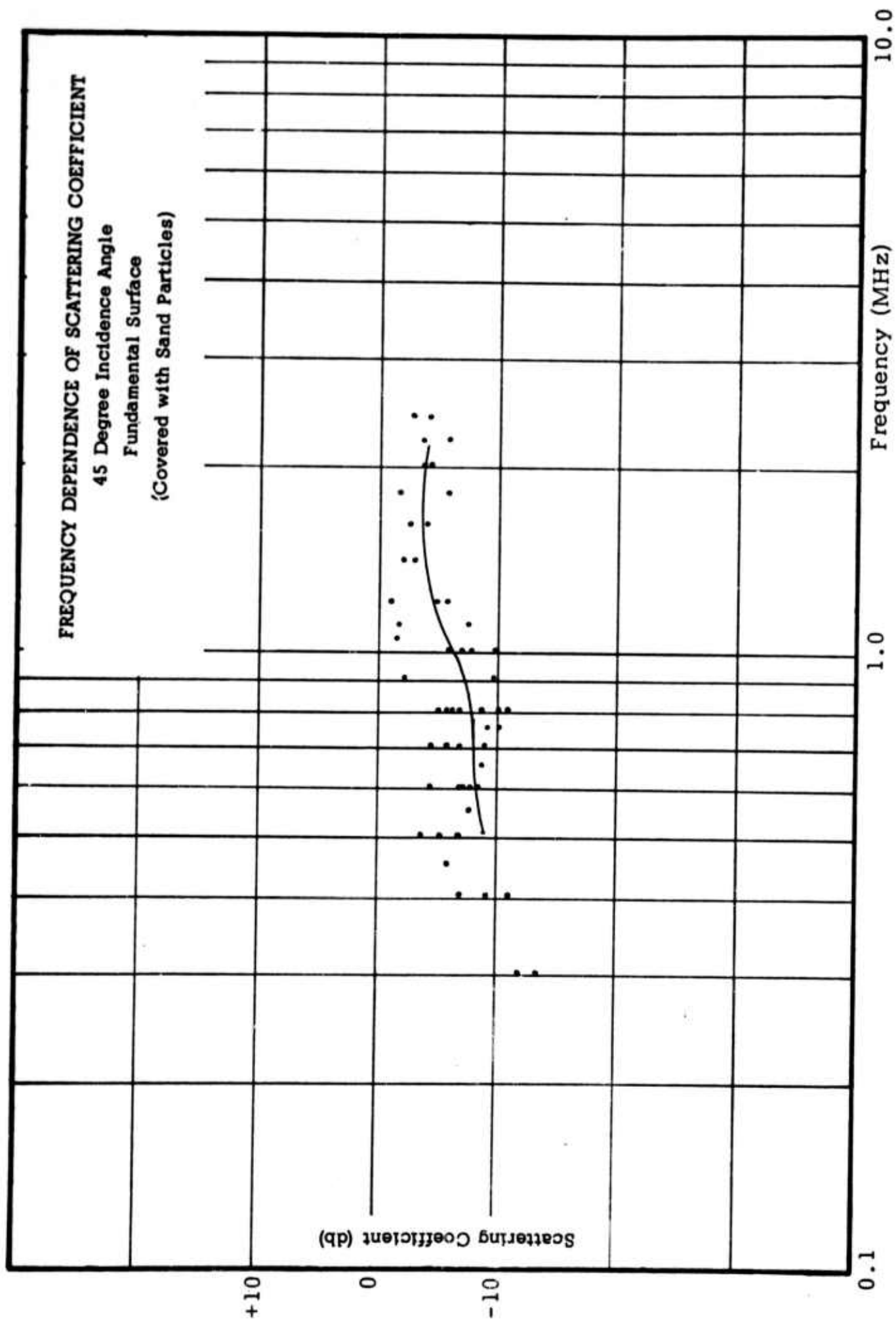


Figure 5.11

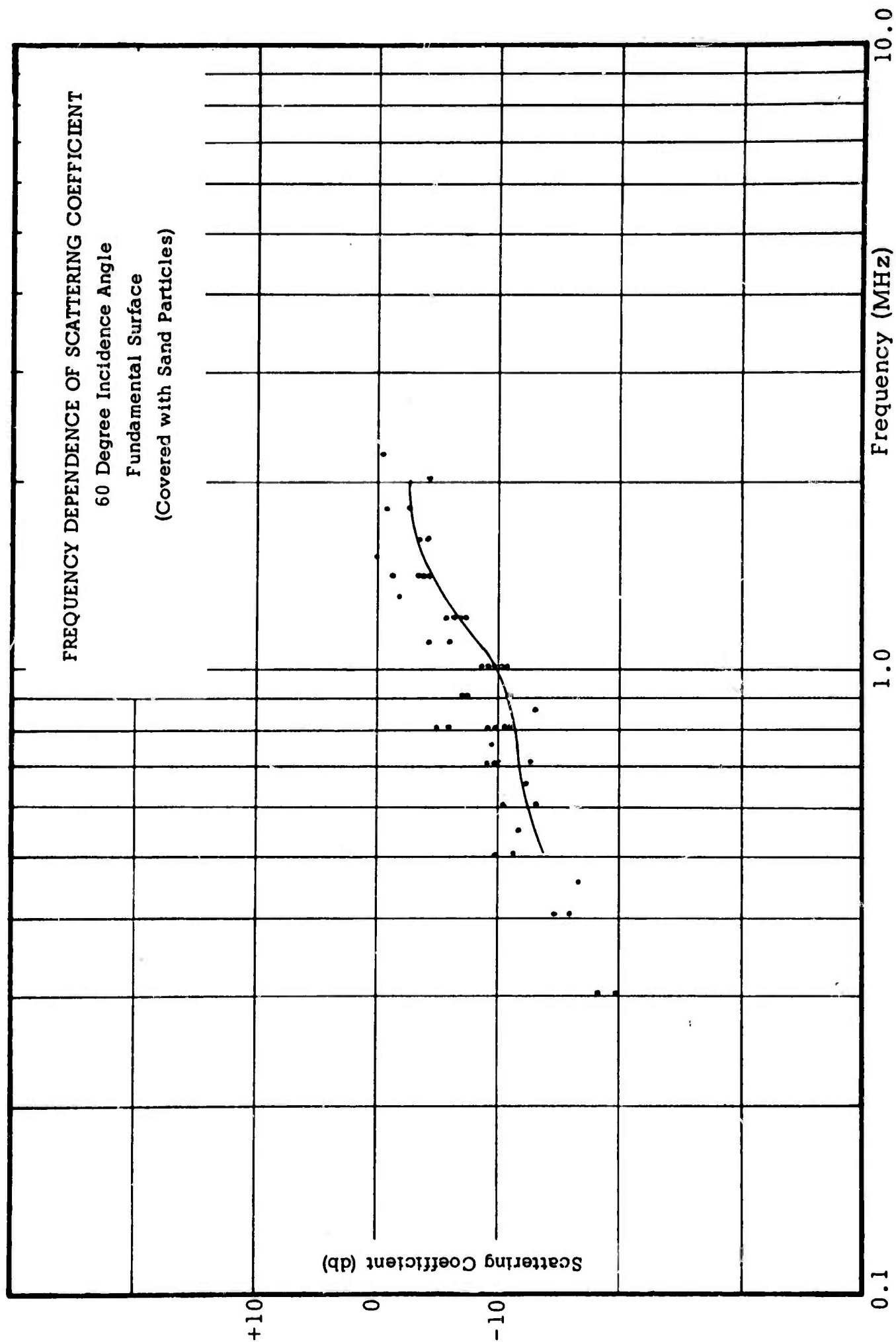


Figure 5.12

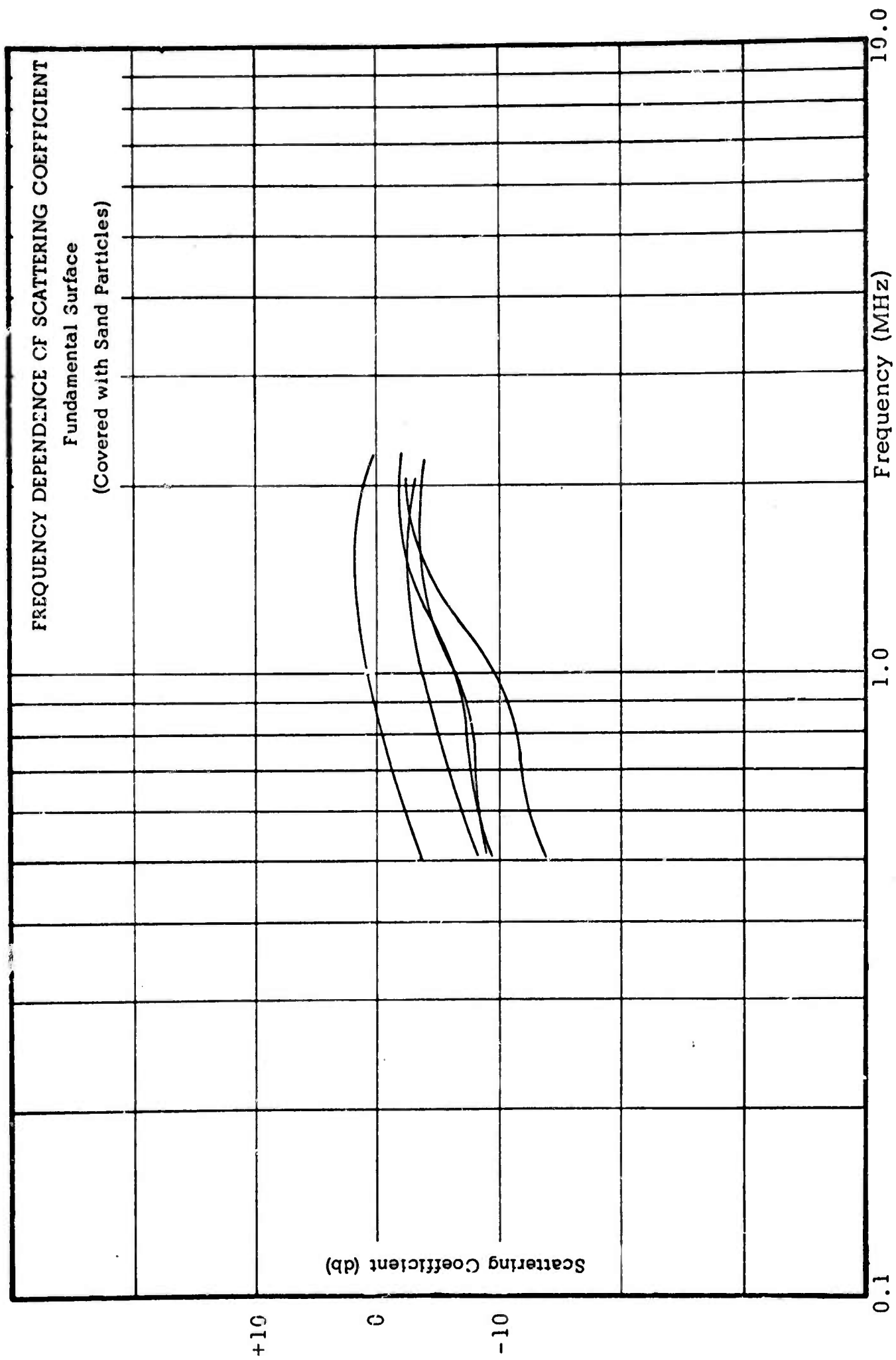


Figure 5.13

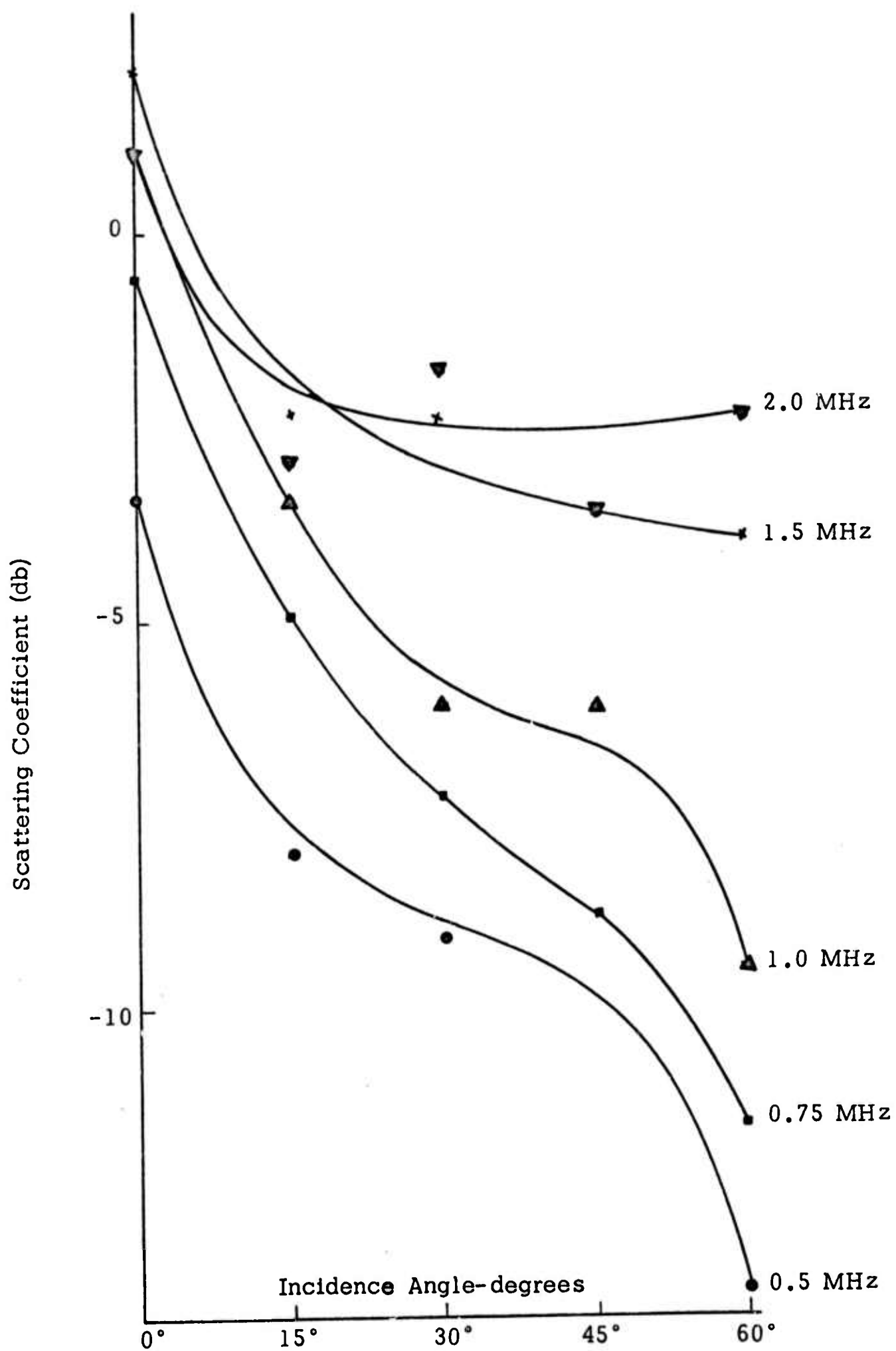


Figure 5.14. Variation of scattering coefficient with angle and frequency - sanded surface.

These data were also plotted as a function of angle for several discrete frequencies in figure 5.14. The plots indicate a greater negative slope near vertical for the low frequencies with a gradual flattening as the frequency increases out to about 1.25 MHz ($\lambda = 1.2$ mm) just as in the case of the fundamental surface. The measurements at 45° incidence confuse the interpretation of the data and an immediate explanation is not available for this phenomenon. The readings tend to conform to expectations as the frequency increases. Above 1.25 MHz the curves remain almost unchanged within the equipment accuracy tolerances.

5.3 Comparison of Results with Experiments

Following the analysis procedure used extensively by Katz (1966) the scattering coefficient frequency dependence curves were fit to a function: $\sigma^\circ = a\lambda^\alpha$. The fit was done by frequency regions and a determination of the best α was made for all data. In figures 5.15 and 5.16 the variation of the coefficient α is plotted as a function of incidence angle for the fundamental surface. In figures 5.17 and 5.18 the coefficients are plotted for the sanded surfaces.

In the next section an attempt will be made to explain the behavior of the curves using the guidelines offered by the Kirchhoff theoretical method of expressing the scattering processes, however as reference to other experimental results, the values of the coefficient α for angular backscatter measurements of sea clutter, cities, snow covered terrain, grass surfaces, the moon, and asphalt and concrete roads are shown in figure 5.19. These data were compiled by Katz (1966) using data from the Ohio State University and Naval Research Laboratory measurements programs. These data were obtained by polychromatic systems (refer to Chapter 2), hence the slope factors were obtained using widely spaced points. Such subtleties as were found in the measurements of the surfaces used in this program could not have been detected.

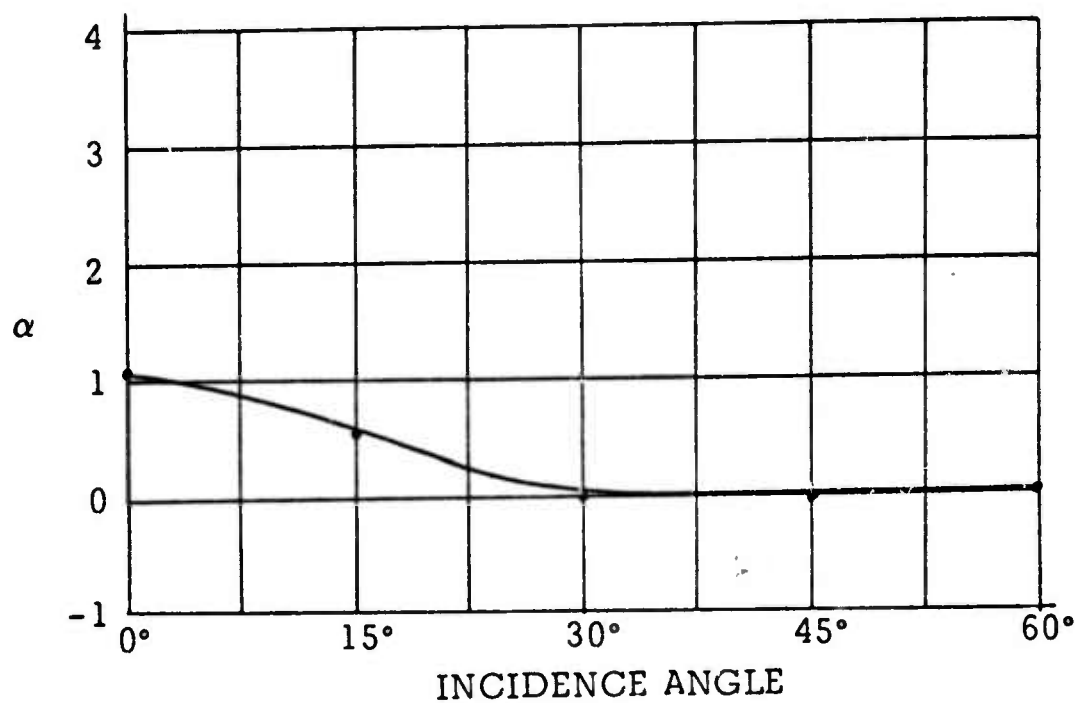


Figure 5.15 Variation of slope for fundamental surface data below 1.25 MHz

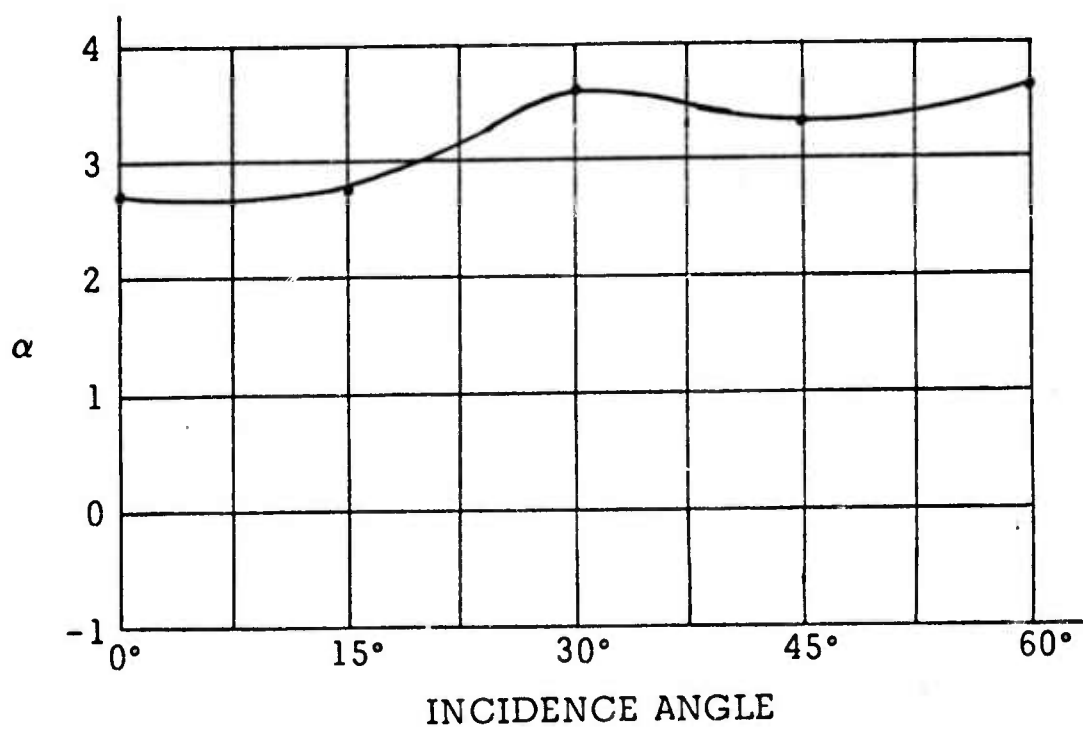


Figure 5.16 Variation of slope for fundamental surface data above 1.25 MHz

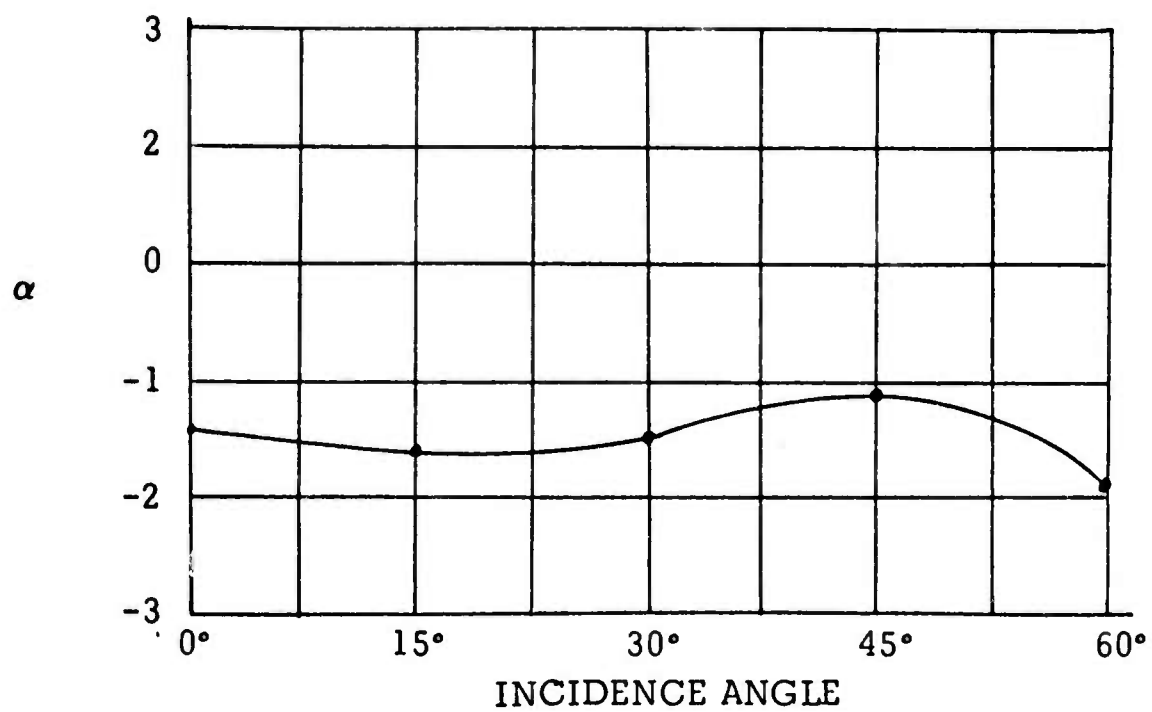


Figure 5.17 Variation of slope for sanded surface data below 1.25 MHz

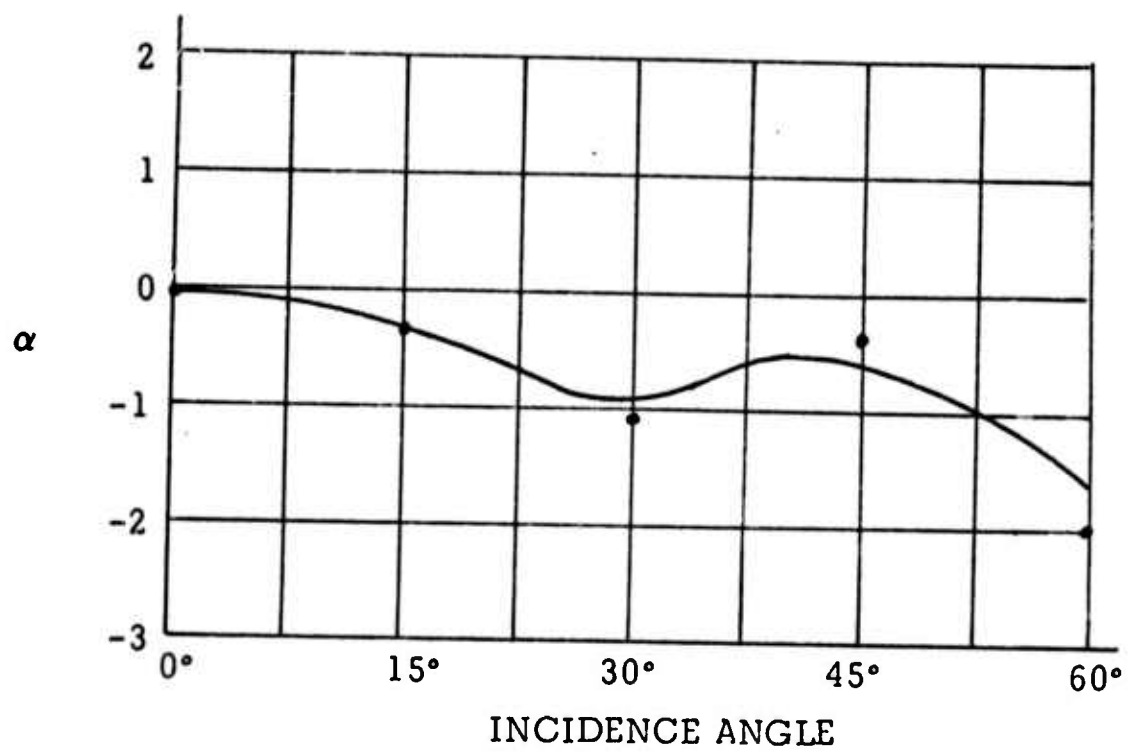
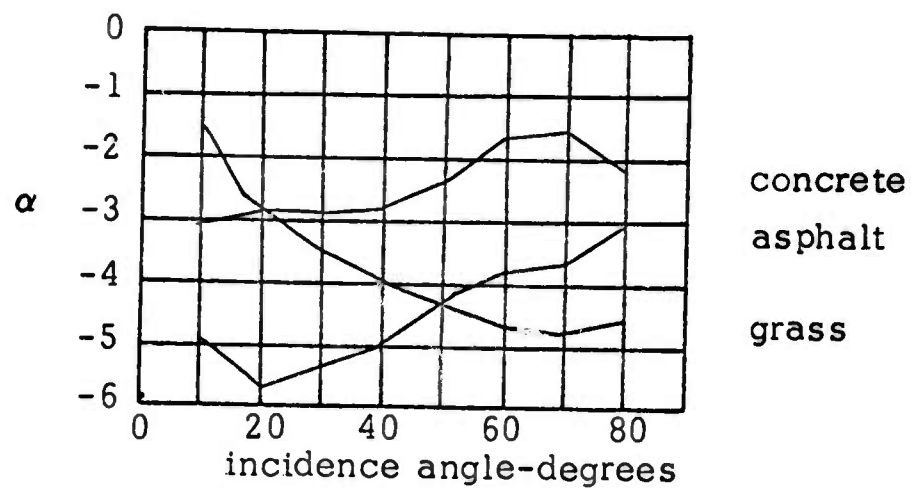
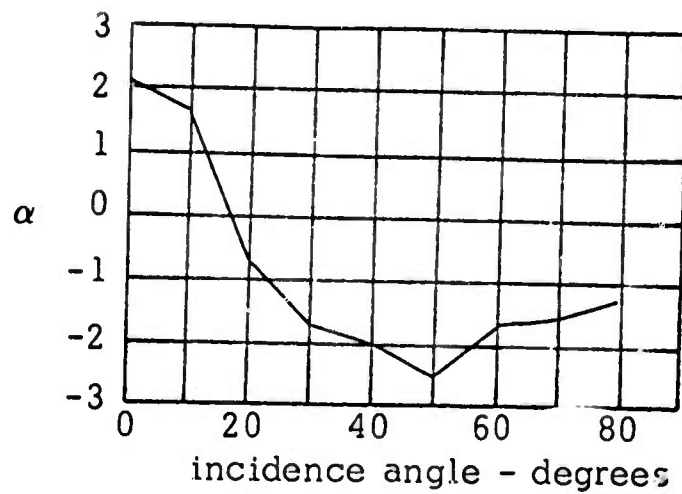


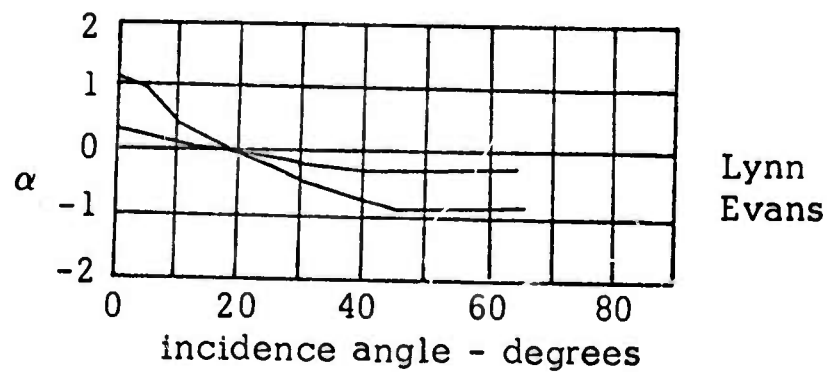
Figure 5.18 Variation of slope for sanded surface data above 1.25 MHz



(a) Wavelength dependence of grass, concrete, and asphalt surfaces.



(b) Wavelength dependence of sea clutter. This figure covers the microwave region from 0.86 to 71 cm and applies to rough sea conditions.



(c) Wavelength dependence of the moon's surface.

Figure 5.19 Variation of slopes for natural surfaces (after Katz 1966)

5.4 Comparison of Results with Theory

Several authors have observed that the scattering behavior of rough surfaces varies with wavelength, but a general expression for this variation is not available. Various theories have indicated a wavelength variation of λ^{+2} to λ^{-6} (Fung and Moore, 1964; Beckman, 1965). Terrain measurements have shown variations of λ^{+5} to λ^{-14} (Katz, 1966; Janza, 1963; Wiltse, et al. 1957). The results presented for the fundamental surface (Figure 5.15 and 5.16) show variations of $\lambda^{+3.7}$ to λ^0 , and λ^0 to λ^{-2} for the sanded surface (Figure 5.17 and 5.18).

Even though a general expression is not available, it is normally accepted that surfaces tend to be "rougher" as wavelength decreases, and the angular variations of the scattering coefficient tend to flatten so that, for an extremely "rough" surface, σ^0 is independent of angle and frequency.

The characteristics of the fundamental surface described in Section 4.3 are such as to assume the Kirchhoff method to be an applicable means of describing the backscatter. In Section 2.1 an expression for the average backscatter power based on the Kirchhoff method was presented as equation (2.10).

$$\langle E_2 E_2^* \rangle = 2\pi F_2 K \int_0^{\infty} J_0(\tau \nu_{xy}) \exp[-g(1-C(r))]/\tau d\tau \quad (2.10)$$

In Appendix A the Kirchhoff method is outlined and reduced to expressions for average backscatter power for "slightly rough" (equation A.39) and "very rough" (equation A.40) normally distributed surfaces having Gaussian autocorrelation. For the case where g is large relative to unity, the surface is termed "very rough" and the expression is (omitting a constant):

$$\langle E_2 E_2^* \rangle = \frac{T^2}{\sigma^2 \cos^4 \theta} \exp\left[-\frac{T^2}{\sigma^2} \tan^2 \theta\right] \quad (5.1)$$

where T = correlation distance
 σ^2 = variance of surface heights
 Θ = incidence angle

Equation (5.1) is independent of wavelength and, even though the measured autocorrelation of the fundamental surface appeared Gaussian, the expression cannot be used to describe the frequency dependence measurements.

In Section A.5 the Kirchhoff method is applied to obtain expressions for average backscatter power for "slightly rough" (equation A.47) and "very rough" (equation A.48) normally distributed surfaces having exponential autocorrelation. For g large relative to unity ("very rough" surface) the expression is (omitting a constant):

$$\langle E_2 E_2^* \rangle = Q \left[\cos^4 \theta + Q \sin^2 \theta \right]^{-3/2} \quad (5.2)$$

where

$$Q = \left[\frac{\lambda T}{4\pi \sigma^2} \right]^2$$

From profile measurements of the fundamental surface the standard deviation was 0.71 mm and the correlation distance was 17.8 mm (run # 2). Using these values, equation (5.2) plots as shown in Figure 5.20. These plots do not fit the measured results, especially for incidence angles greater than 30° . It was noted in Section 5.1 that the data are seemingly separated into different behavior regions below and above about 1.25 MHz. Since the maximum α predicted by any of the above expressions is +2, which is the slope of the zero degree incidence curve, the region above 1.25 MHz cannot be fit (refer Figure 5.16). However using the run # 1 profile measurements of $\sigma = .678$ mm and $T = 13.97$ mm the theoretical curves for 0° and 15° incidence angles are fit reasonably well in the region below 1.25 MHz, but the fit to 30° is poor (Figure 5.21). These values represent a (T/σ^2) value of 29.66.

It was noted that a (T/σ^2) value of 20.97 provided a reasonable fit to the 15° and 30° measurements in the region below 1.25 MHz, but the fit to 0° is poor (Figure 5.22). Attempts to fit the data above 30° incidence do not appear practical using equation (5.2), but the literature shows that there is no general agreement as to the validity of the theory for large angles of incidence.

The fact that different angular regions were fit by use of different standard deviations and correlation distances was also noted by Fung and Moore (1964) in attempting to fit lunar backscatter data using equation (5.2). The fact that these parameters appear to be angle dependent suggests that they may also be wavelength dependent. This has also been suggested by several authors (Fung 1965) who note an apparent "size filtering" effect due to the incident wavelength.

To examine this further, it will be assumed that the ratio (T/σ^2) is an effective parameter which is a function of angle and wavelength. Further, it is arbitrarily assumed that the dependence is of the following form:

$$R_e = R f(\theta) \left(\frac{\lambda}{\lambda_0} \right)^\rho \quad (5.3)$$

where: R_e = effective parameter, $(T/\sigma^2)_e$

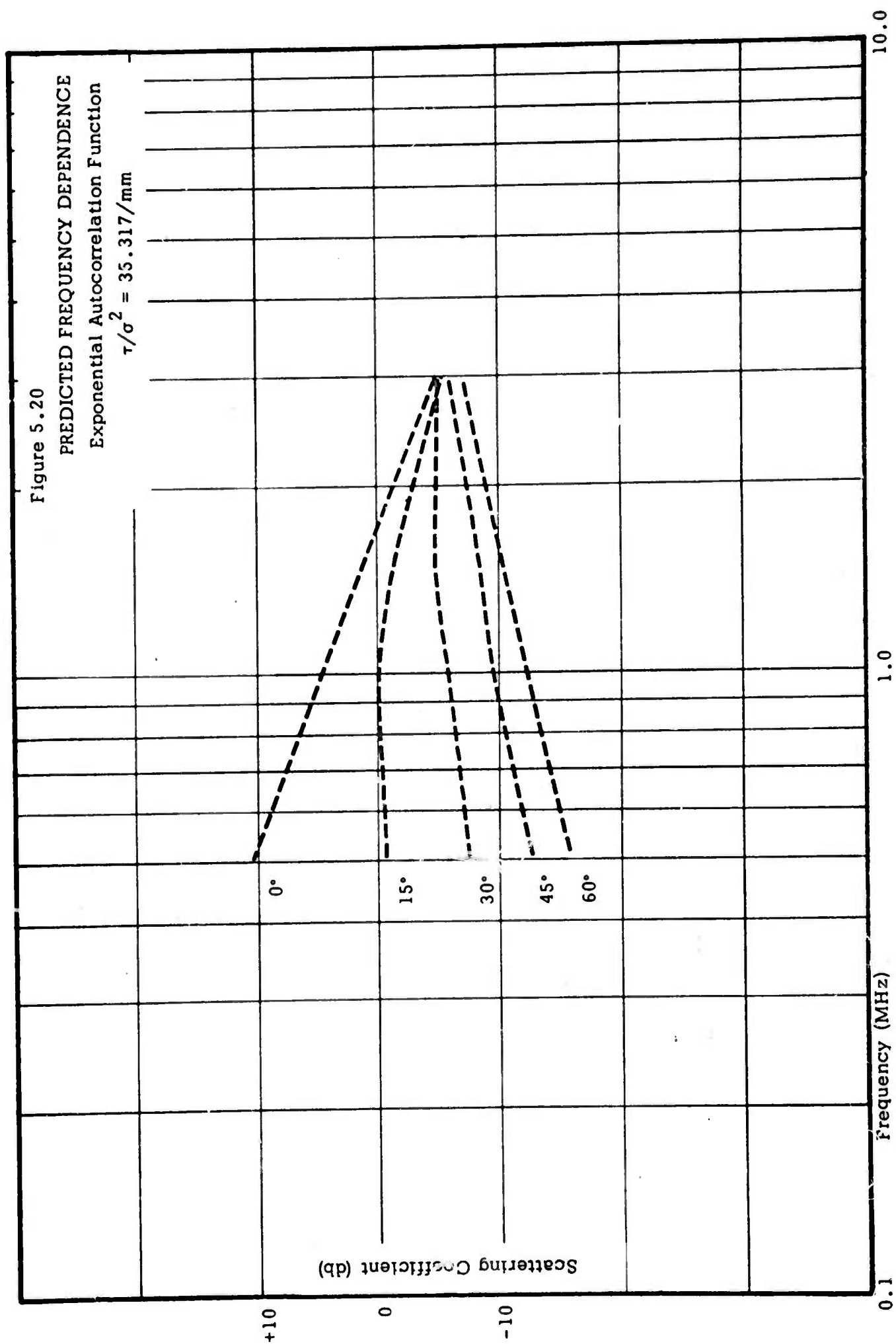
R = actual parameter, (T/σ^2)

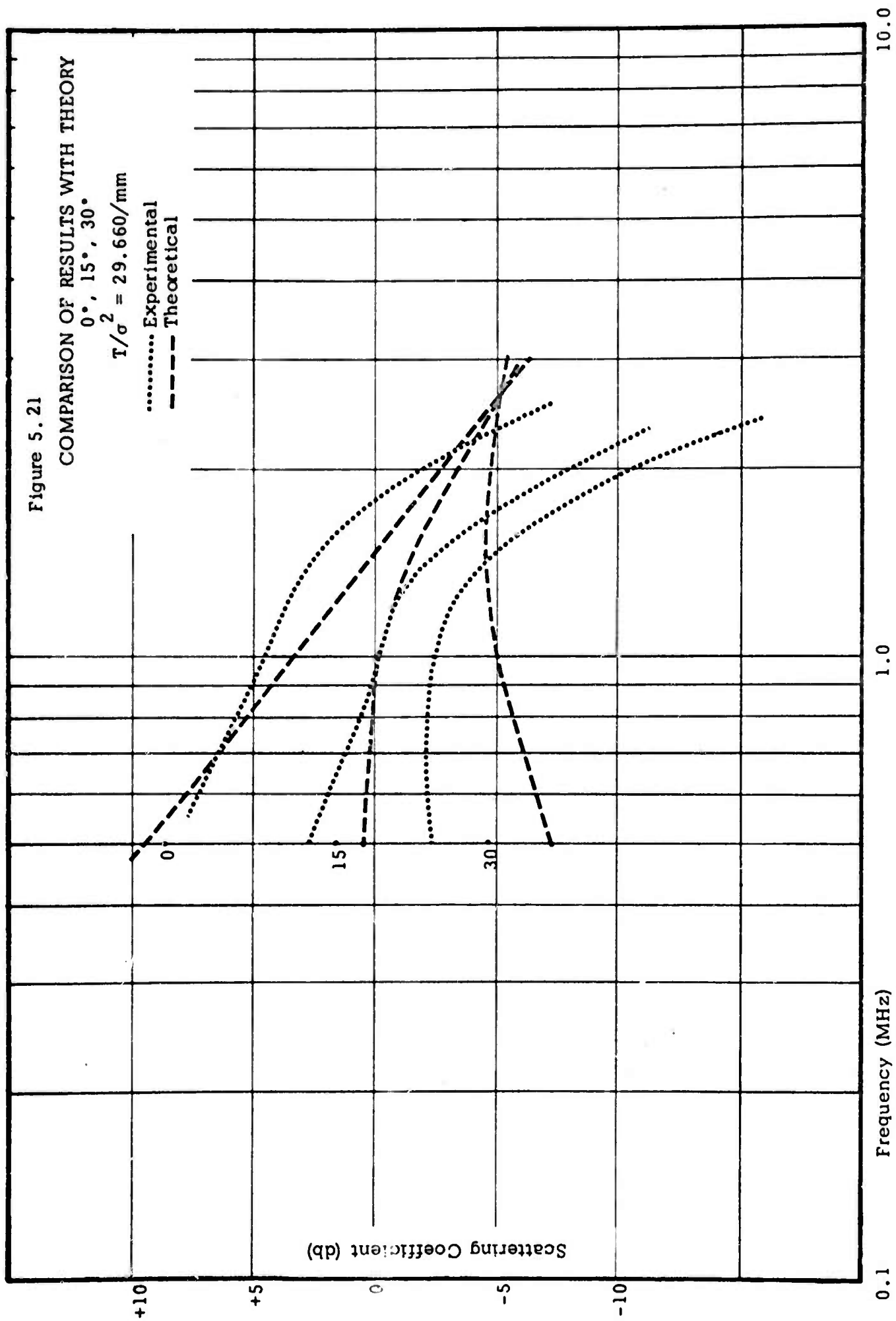
$f(\theta)$ = undefined function of incidence angle

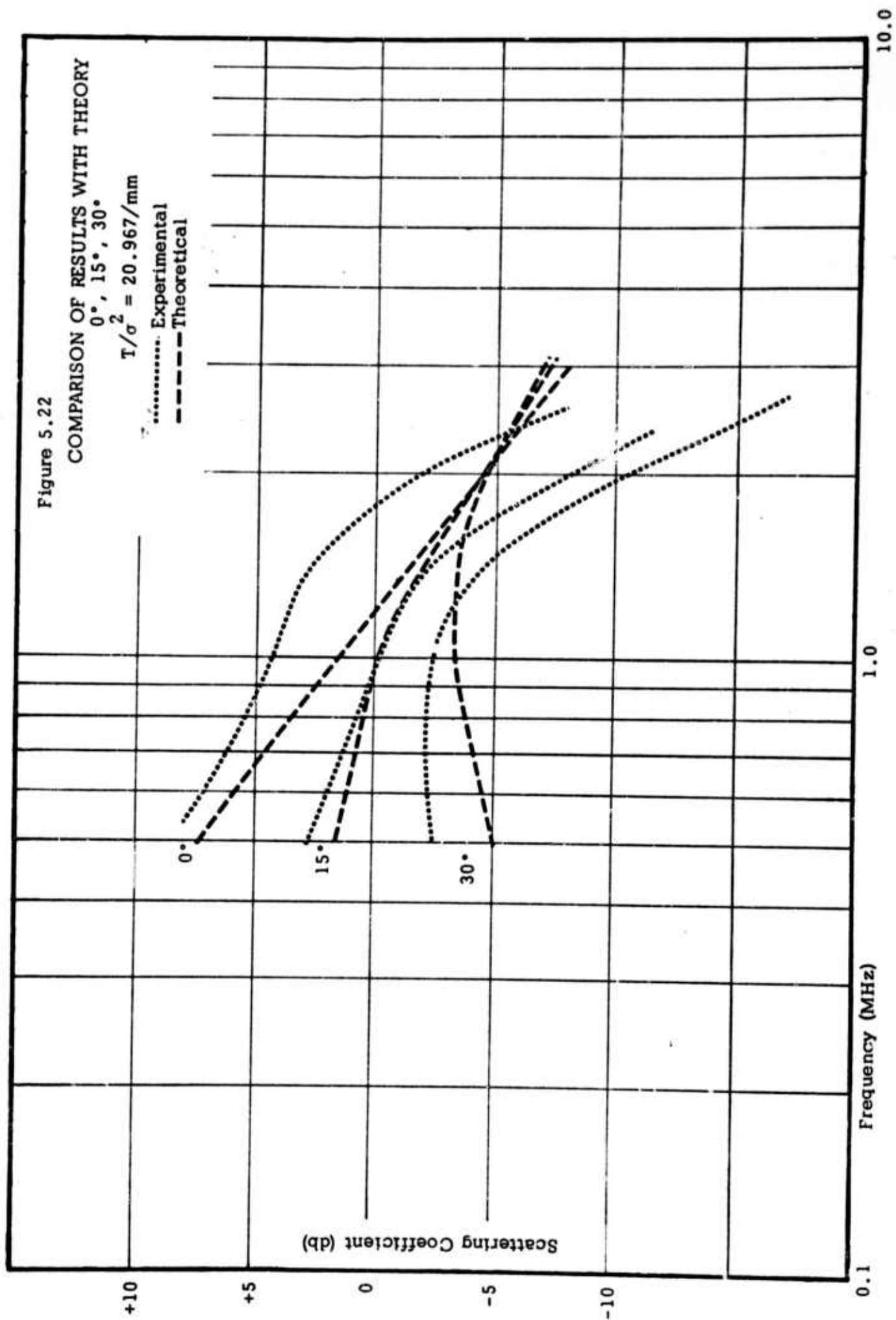
λ = incident wavelength

λ_0 = wavelength for which $R_e = R f(\theta)$

If ρ is positive, as intuitively it should be, then equation (5.2) predicts a slope coefficient, α , greater than +2, and hence the region above 1.25 MHz could be explained. In the region above 1.25 MHz, the 0° data vary as $\lambda^{+2.8}$. Using (5.3) in (5.2) leads to an expression which will fit the measurement results if $\rho = 0.4$. Figure 5.23 shows the comparison of the measured and predicted results using $\rho = 0.4$, $\lambda_0 = 1.25$ mm, $R = 35.317$,







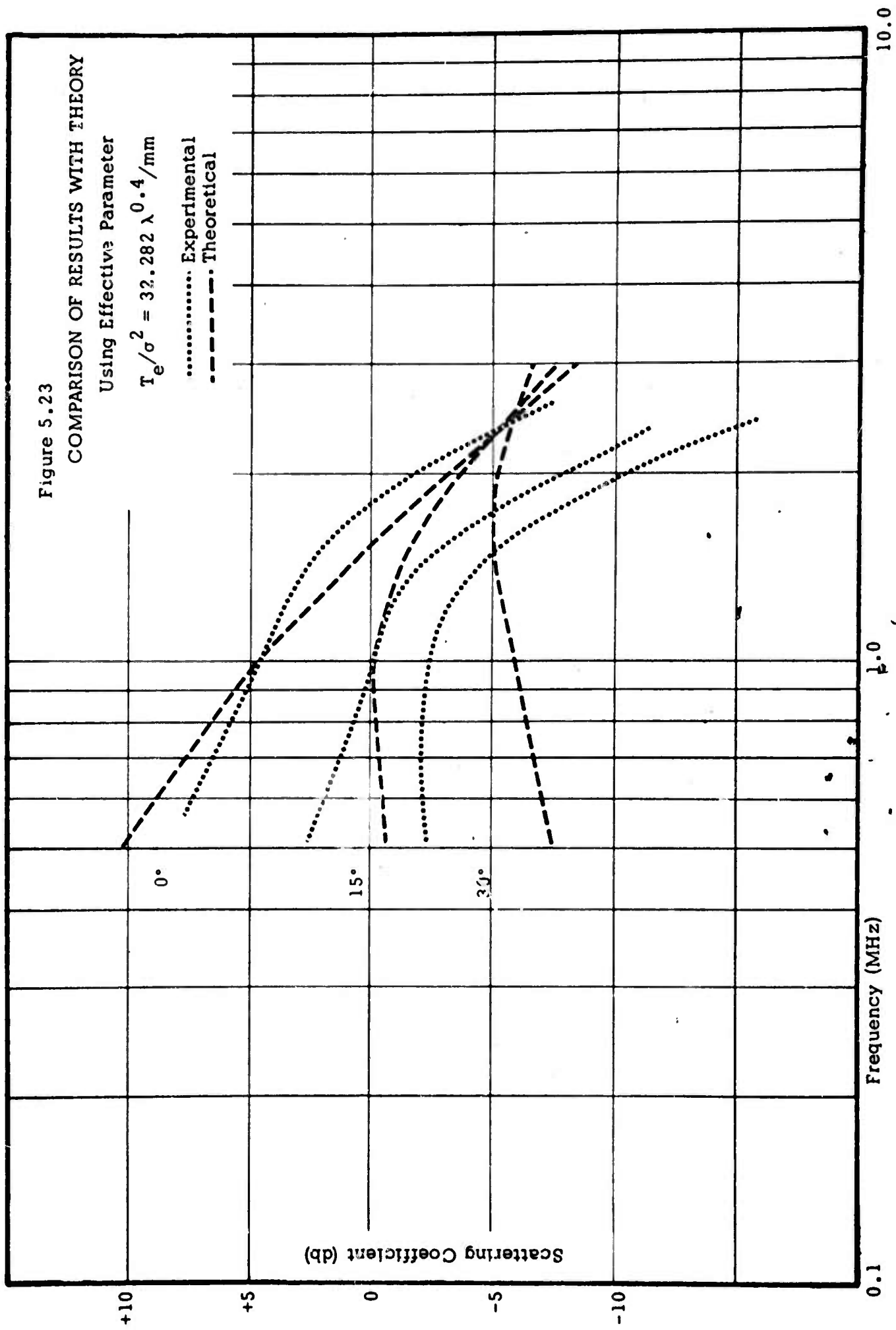
and $f(\Theta) = 1$ for the region above 1.25 MHz ($\lambda = 1.25$ mm). This approach improved the fit to the 0° data, however the 15° and 30° data fit remains poor.

5.4.1 Summary of Comparison with Theory

Although some degree of matching of the measured and theoretical results was obtained, considerable doubt exists as to the ability of the Kirchhoff method to predict the frequency dependence of backscatter, at least in cases where the actual surface autocorrelation is approximated by an autocorrelation function. A point of major concern is that the best fit occurs using the expressions derived for an exponential autocorrelation function, which clearly cannot fit the measured surface autocorrelation. This contradiction is somewhat overcome by the approach used by Fung and Leovaris (1968), which in essence maintains the form of equation (5.2), but allows incorporation of autocorrelation functions other than the exponential. This approach is discussed in Appendix B. Even with this approach the maximum wavelength variation is λ^{+2} (at $\Theta = 0^\circ$), and the coefficient must decrease as Θ increases. This characteristic is contradicted by the measurements of the fundamental surface (see Figure 5.6) and the results of Wiltse, et al. (see Section 2.2.5). Likewise the theory cannot predict results such as those compiled by Katz (see Section 5.3).

The effective parameter approach is supported by the physical reasoning that different subranges of structure sizes dominate the return at different incidence angles and/or wavelengths. These subranges have autocorrelations and variances which are not the same as the autocorrelation and variance of all subranges combined, i.e. the entire surface. Several attempts have been made to incorporate this character into the scattering expressions to describe the angle dependence (Beckman 1965; Fung and Moore 1964, 1966; Davies 1954). These attempts have been only moderately successful and the use of equation (5.3) is likewise only moderately successful.

In summary, the measurements obtained in this program, as well as



those of other programs, suggest, in agreement with Davies (1954), that use of the autocorrelation function approximation of the surface autocorrelation does not give sufficient statistical information to describe the scattering from the surface.

CHAPTER 6

IMAGE EXPERIMENT

In recent years the use of imaging radar systems for both military reconnaissance and geoscience investigations has expanded rapidly. Associated with this expanding demand has been the growing realization that the monochromatic nature of such systems handicaps their utility, especially in military reconnaissance applications. This chapter presents an experiment with a panchromatic imaging system. In this experiment monochromatic images of complex targets are compared with panchromatic images to show the effect of frequency averaging. The substantial improvement in target definition obtained is impressive, especially in view of the fact that less than a $\pm 10\%$ bandwidth is employed, and that little increase in system power or complexity is required to gain this improvement.

The theme of the chapter is illustrated in Figure 6.1 which shows an acoustic image of two spheres. The images actually show an expanded view of a small area of the sphere's surface near the apex. The return signal strength from regions away from the apex is below the noise level. In 6.1 (a) the spheres are imaged monochromatically and lobing is evident. In 6.1 (b) the frequency was swept $\pm 10\%$ from the center frequency. The frequency averaging of the lobes is obvious. The monochromatic lobes are investigated in detail in section 6.3 and the effect of frequency averaging is illustrated.

6.1 Measurement Technique

Acoustic images were obtained in a manner completely analogous to an airborne imaging radar system. The antennas (transmitting and receiving transducers) were moved past the targets at a fixed distance and uniform velocity. The transducers were mounted on a linear motion carriage that was capable of a wide range of movement velocities and

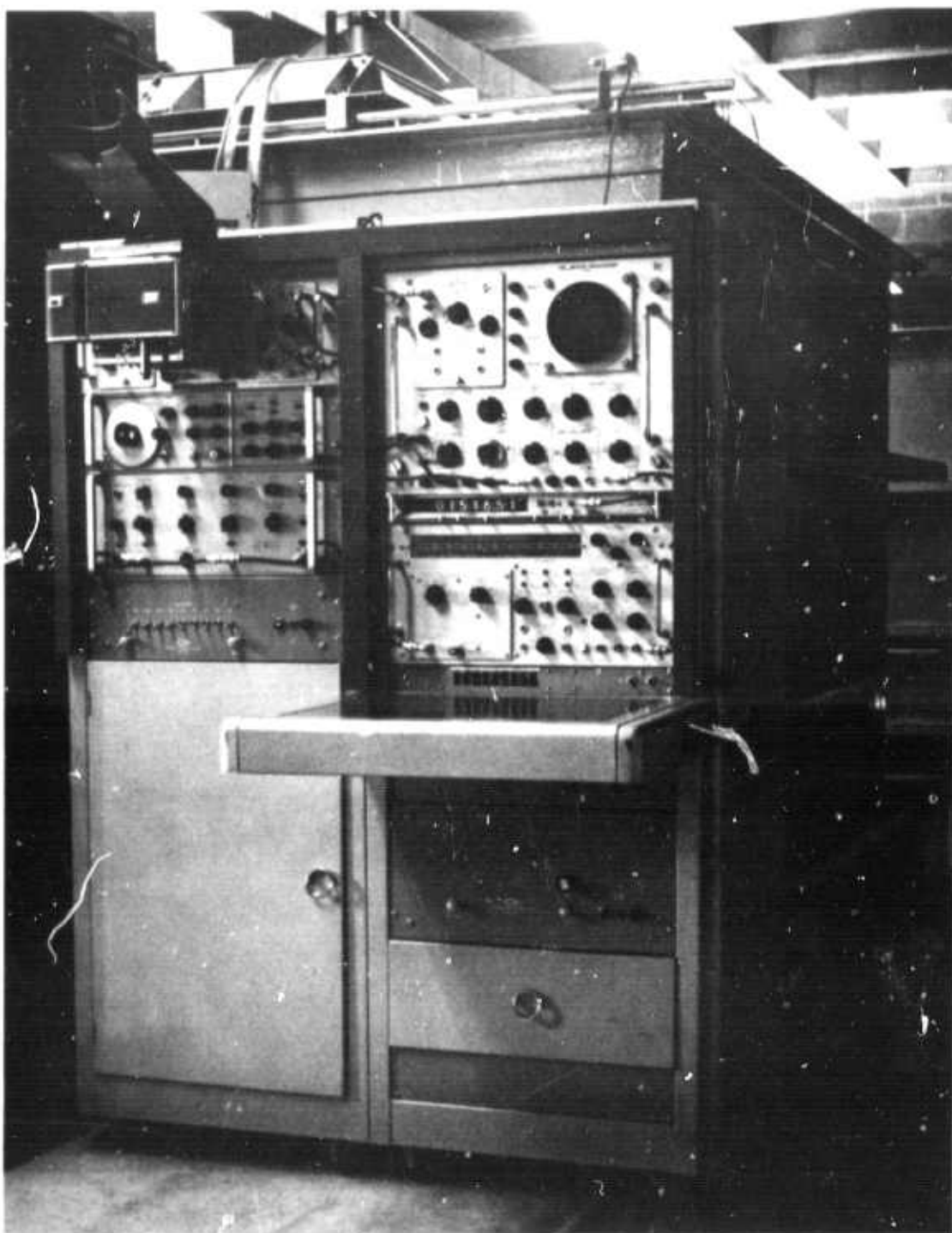
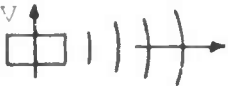
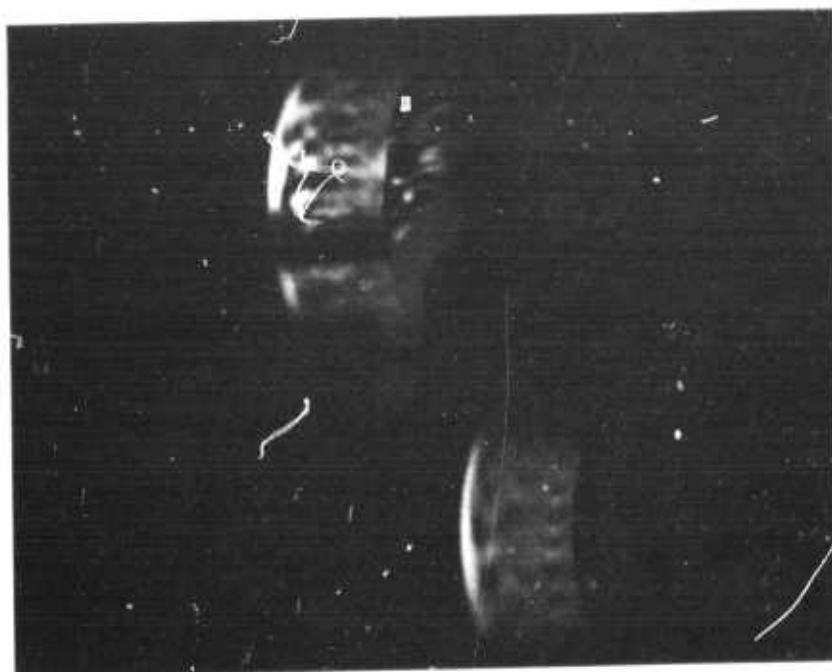
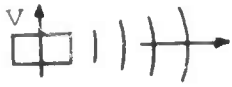


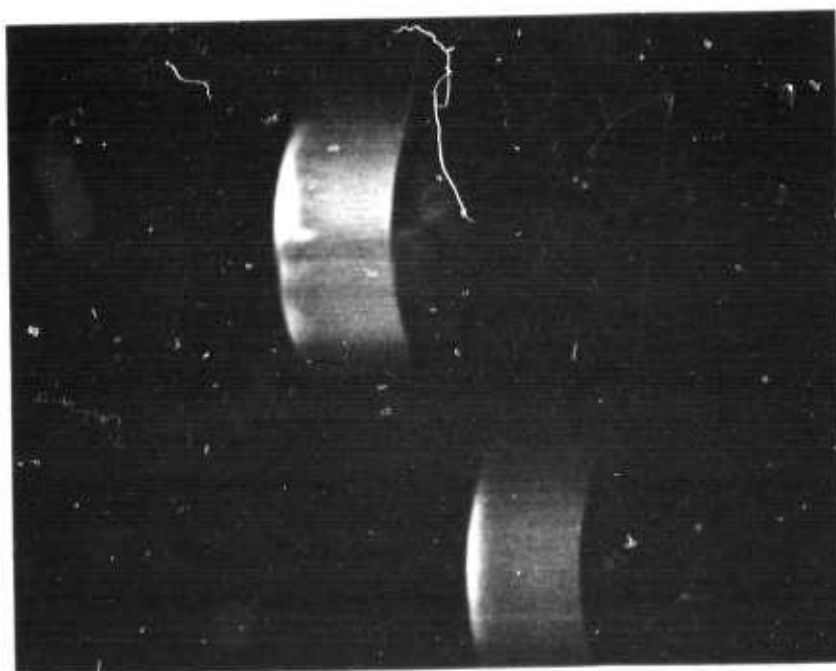
Illustration 6.1 ACOUSTIC TEST FACILITY IN IMAGING MODE


 transducer



(a) Monochromatic image of two spheres
($f = 1.5 \text{ MHz}$)


 transducer



(b) Swept frequency image of two spheres
($f = 1.5 \text{ MHz} \pm 10\%$)

Figure 6.1 Effect of frequency average on image of sphere targets

transducer position settings. The position geometry is shown in Figure 6.2 and a photograph of the arrangement is also shown.

The system operation associated with obtaining acoustic images was described in Section 3.5. In review, the signal return is envelope detected and applied to the grid of an imaging CRT. Each return, i.e. the return associated with each transmitted pulse, intensity modulates one horizontal line trace on the CRT. Sequential returns form sequential intensity-modulated line traces each vertically displaced from each other. The end result is an intensity modulated raster display. A photographic image is obtained by exposing the film during the entire vertical traverse time interval. The procedure is illustrated in Figure 6.3.

The imaging experiment was designed around the limitation presented by the transducers. That is, the available piston transducers provide only conical beams and have relatively high sidelobes. The use of spherical targets insured that the sidelobes of the antenna did not influence the return over the area of investigation of the reradiation pattern. Ideally the experiment would concentrate on imaging area-extensive targets such as those of concern to imaging radar systems, however the lack of a fan-beam antenna discouraged this approach. Fortunately, as will be shown in Section 6.2, the spherical targets provided the information needed to relate to the area extensive imaging problem, hence the limitation to a conical beam did not restrict the value of the experiment.

The parameters of the experiment were set with the following consideration. The objective of the experiment was to determine the effect of introducing a broad-spectrum signal in place of a monochromatic signal. The targets examined were complex and consequently provide a reradiation pattern consisting of a multiple of fine lobes. To determine the effect of frequency averaging required that the effect of sample averaging be excluded. That is, the image would be altered if the number of "looks" were changed by the fact that more or less lobes would be seen. To eliminate this variable, the sampling rate (PRF) was set sufficiently high that all lobes would be recorded and the rate was not altered when the swept frequency was introduced. The carriage velocity was set at 6.5 mm/sec and the PRF

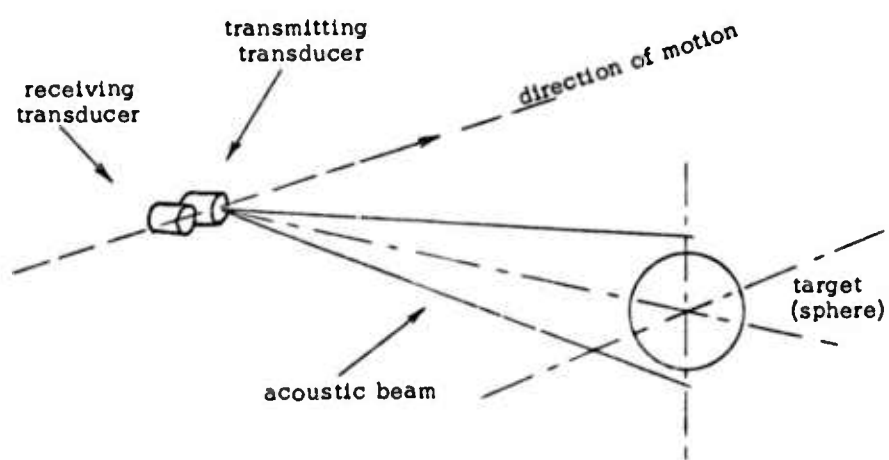


Figure 6.2 Positioning for acoustic imaging.

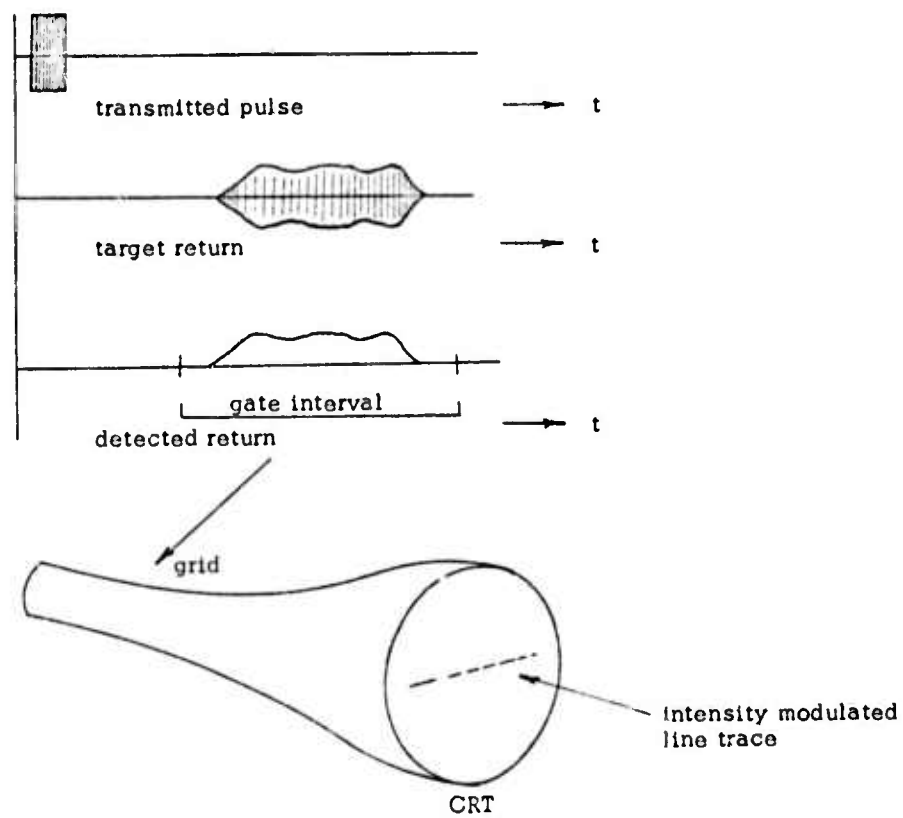


Figure 6.3 Image recording of target return.

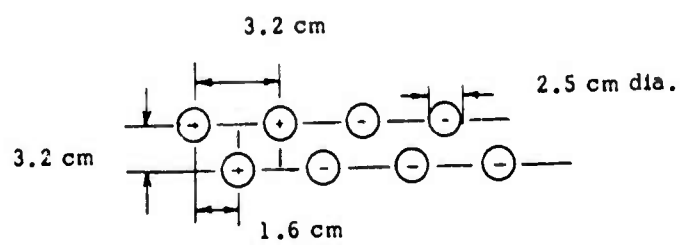


Figure 6.4 8-element array.

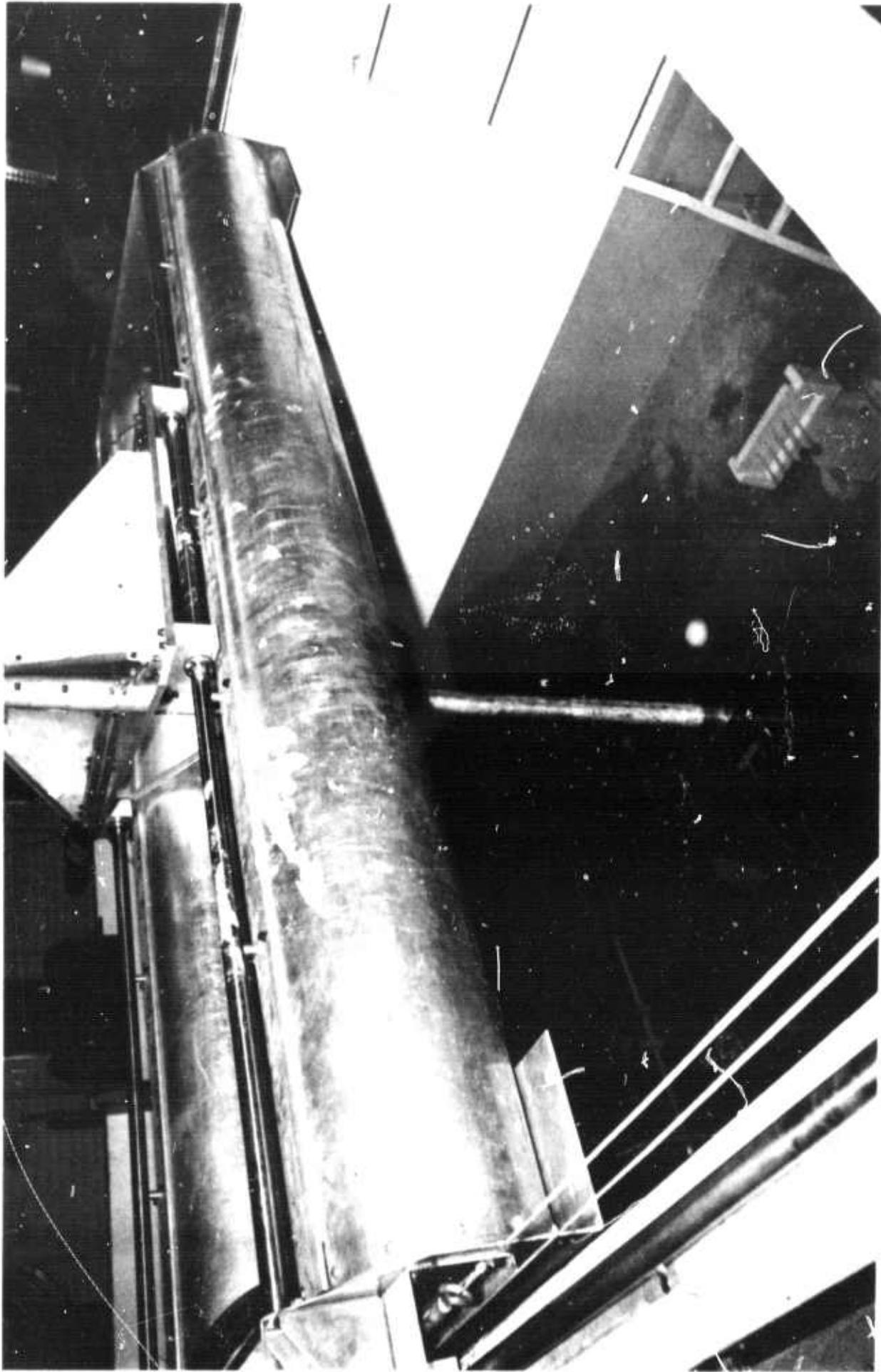


Illustration 6.2 LINEAR MOTION CARRIAGE

was set at approximately 130 Hz. This provided one sample for each .05 mm of carriage travel.

In Chapter 3 the system operation was described and the "slow-sweep" mode was outlined. This mode of operation consists of sampling the swept frequency at the pulse-rate frequency. Ideally broad-spectrum imaging would be done using a "fast-sweep" mode, that is the entire spectrum would be transmitted during each pulse. This could conceivably be simulated by increasing the PRF proportional to the sweep time. That is, if the PRF for monochromatic imaging is 100 Hz, set the sweep time at (1/100) sec and increase the PRF to 400 Hz to provide 4 samples per sweep. Unfortunately this reintroduces the effect of increasing the sampling rate and hence for this experiment the PRF for both monochromatic and swept frequency signals was the same, 130 Hz. The sweep time was adjusted to give 4 samples per sweep (about 23.5 m sec). The samples were not synchronized with the sweep, and hence the frequency sampling varies sweep-to-sweep. In this manner the full sweep is effective even though the sampling rate is very low.

The width of the pulse was set at .6 - .8 msec to provide a return segment which did not include the effect of the high frequency components in the leading and trailing edge of the transmitted pulse. It was determined that the spherical targets caused the return signal to be restricted to an area near the apex, hence the leading edge effect decayed rapidly. Therefore by extending the pulse width beyond this decay interval, the leading edge effect was excluded. This effect is evident in the images shown in Figure 6.1.

The useful bandwidth of the swept signal was restricted by the frequency response of the transducers. The response curves fall so rapidly that variations greater than about $\pm 10\%$ from resonance were impractical.

6.2 Targets

Three primary targets were used in this experiment: (1) a 4.5 cm diameter rubber sphere; (2) a 7.8 cm diameter styrofoam sphere; and (3) an 8-element planar array consisting of 2.5 cm diameter wooden spheres

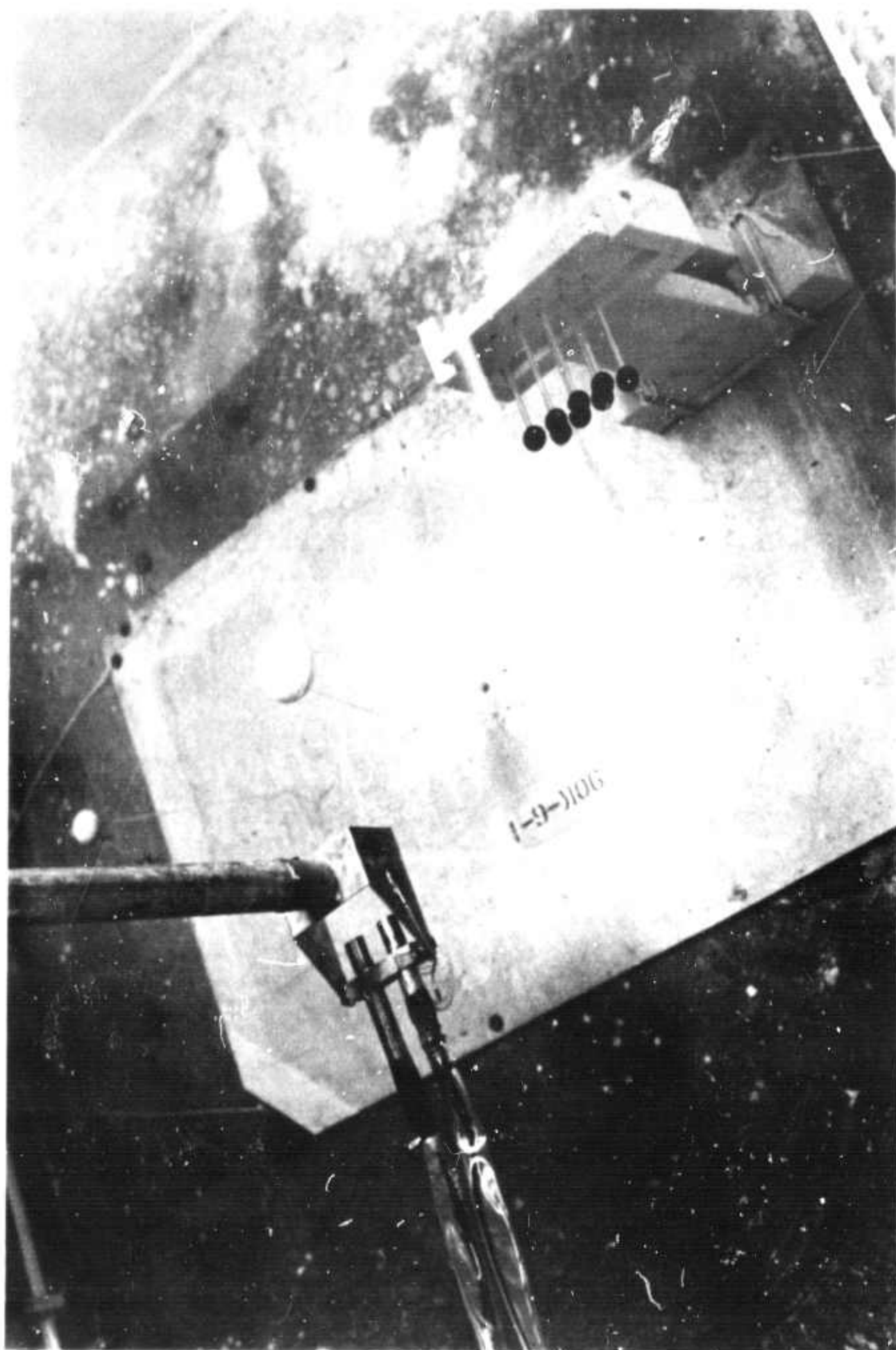


Illustration 6.3 IMAGING EXPERIMENT OBJECT TARGETS

located on 3.2 cm centers in two rows of 4-elements each. The targets are shown in the photograph as they were positioned in the tank. The rubber sphere is on the left.

6.2.1 Rubber Sphere

This target is a relatively smooth, soft rubber sphere selected to provide a broad, hopefully frequency-insensitive, lobe in the direction of backscatter. Although the exact composition of the sphere is unknown, it is reasonable to assume negligible shear waves and a reasonably high reflection coefficient. The diameter of the sphere is very large relative to the incident wavelength, but is smaller than the illuminated area of the beam. Under these conditions the scattering cross section should be almost independent of wavelength (Stratton, 1941) and the sphere would provide the necessary calibration reference for other measurements.

The measurements presented in Section 6.3 verify the presence of a strong, almost frequency insensitive, reflection in the backscatter direction, however the fact that the sphere is not perfectly smooth to the incident wavelength is evident.

6.2.2 Styrofoam Sphere

This target was selected to illustrate an effect very common to imaging systems but one that is difficult to simulate acoustically in a controlled manner; that is, an area extensive surface consisting of various size randomly oriented scatterers. The surface of the sphere is rough in the somewhat facet-like manner typical of styrofoam. Consequently some scatterers are sufficiently close together to form highly directional reradiation patterns similar to closely spaced arrays. In addition the multilobe pattern of widely spaced elements exists, and scatterer sizes both large and small relative to the incident wavelength are present. The spherical configuration reduces the illumination area edge effects and helps accent the behavior of the surface reradiation lobes by restricting the contributing area to a much smaller size than is otherwise possible using the available acoustic transducers.

6.2.3 Array

The array target consists of eight spheres arranged as shown in Figure 6.4. The purpose of this target is to provide a large number of narrow lobes of different amplitudes. The array is an extension of a 4-element array (one row of spheres) which provided the desired fine lobe structure, but the lobes were of almost equal amplitude. The effect of variations in incident wavelength is better illustrated by use of the more directional pattern of the 8-element array.

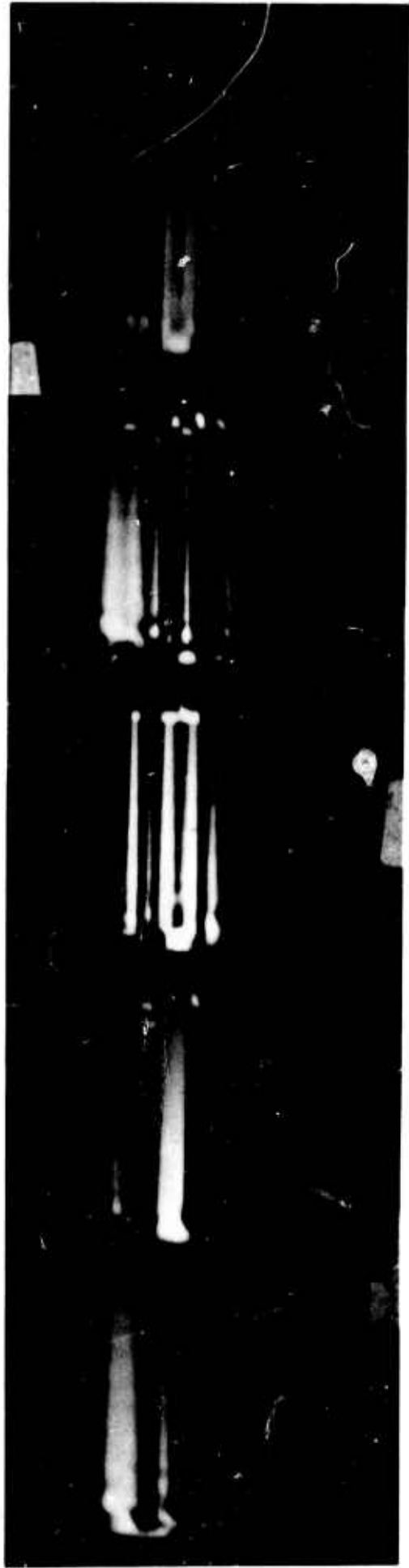
The reradiation pattern of an array of point scatterers spaced several wavelengths apart can be calculated, and the results show a number of lobes proportional to the number of elements. The width of each lobe is also proportional to the number of elements (Silver 1964). The spherical elements of the target array cannot be interpreted as point scatterers; however the area on the sphere contributing to the reradiation is sufficiently small that a very similar pattern to that calculated is created.

6.3 Results

The results clearly indicate that the addition of frequency averaging of the reradiation pattern of complex targets substantially improves the definition of the target. The reader should bear in mind that the results presented represent only the addition of a swept frequency during transmission, done in such a manner that each pulse modulated a different carrier frequency on a repetitive sweep basis. Several other techniques are possible, some perhaps more optimum than the method used here (Gustafson and As, 1964; Kosowsky, et al., 1963; Ray, 1966). However, the point is well made that the addition of frequency averaging warrants consideration in the design of imaging radar systems.

6.3.1 Rubber Sphere

Figure 6.5 shows the acoustic image of the rubber sphere for four separate frequencies and a swept frequency. The images were recorded from a distance of 51 cm., and consequently the illumination region of the transmitted beam was 6 cm in diameter. The target diameter was 4.5 cm.



$f = 1523 \text{ KHz}$	$f = 1637 \text{ KHz}$	$f = 1750 \text{ KHz}$	$f = 1819 \text{ KHz}$	$f = 1640 \pm 100 \text{ KHz}$
$G = 15 \text{ db}$	$G = 16 \text{ db}$	$G = 17 \text{ db}$	$G = 21 \text{ db}$	$G = 21 \text{ db}$

Figure 6.5. Acoustic images of rubber sphere target

The images of the styrofoam sphere and the array show the existence of, what may properly be termed, multiple lobes. The return from the rubber sphere consists of multiple "specular points". That is, the sphere is obviously not perfectly smooth to the incident wavelength, but the roughness does not produce an array effect such as the styrofoam sphere. The significance of this distinction is that for an array the lobes "move" with frequency and hence an averaging is obtained. This effect does not occur with the rubber sphere. The distinction evident between images at different single frequencies is that each "specular point" has a different amplitude from frequency-to-frequency. The swept frequency image clearly shows the target to have two major "specular points", where one is 6 db greater than the other. Other such points are indicated to exist at lower levels. No single frequency image clearly defines both points, and limited to any one single frequency image the definition of the target is misleading. In comparing figure 6.5 to figure 6.1, both of which show the rubber sphere, the reader should note that figure 6.1 was obtained by imaging a region of the sphere slightly off-center and hence the dynamic range of the "specular point" return was less than the returns shown in figure 6.5, which are from the apex.

6.3.2 Styrofoam Sphere

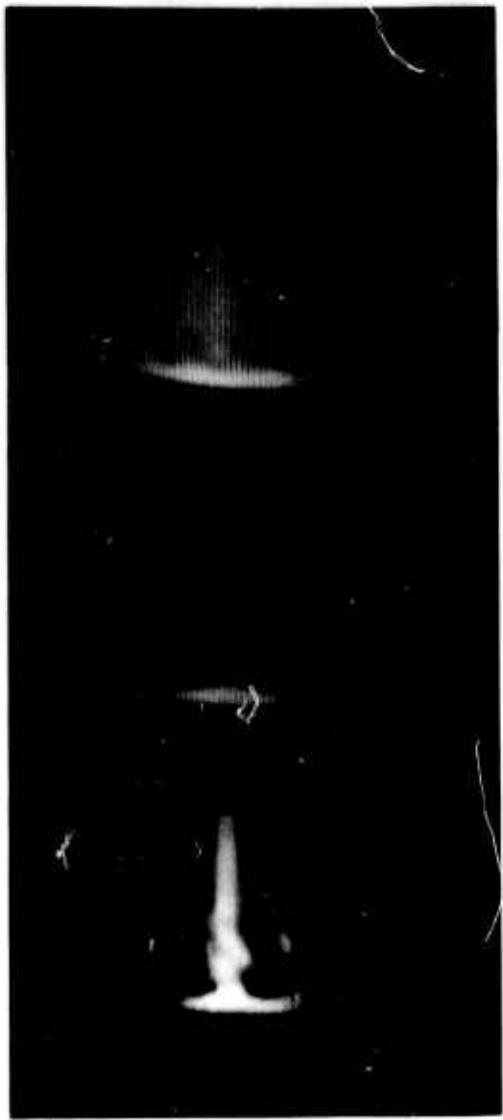
Figure 6.6 shows the acoustic image of the styrofoam sphere for several single frequencies. In Figure 6.7 one of the monochromatic images is compared to swept frequency images of $\pm 3\%$ and $\pm 6\%$ from center frequency. The images were recorded at a distance of approximately 1 m and a beam illumination region of 11.6 cm diameter. The reradiation lobe pattern is more complex than the simple rubber sphere and the effect of varying frequency is marked. Of special interest is the phase cancellation of the center main lobe (well defined at 1520 KHz and 1626 KHz) at 1427 KHz, 1744 KHz, and 1816 KHz. The effect occurred at numerous intermediate frequencies as well.

The application of swept frequency illumination (Figure 6.7) smoothed the monochromatic lobes and formed a uniform, broad backscatter lobe.



$f = 1.43 \text{ MHz}$ $f = 1.52 \text{ MHz}$ $f = 1.64 \text{ MHz}$ $f = 1.74 \text{ MHz}$ $f = 1.82 \text{ MHz}$

Figure 6.6 Comparison of different frequency images of styrofoam sphere target



$F = 1.64 \text{ MHz}$ $f = 1.64 \pm 0.05 \text{ MHz}$ $f = 1.64 \pm 0.1 \text{ MHz}$

Figure 6.7 Comparison of monochromatic and swept frequency images of styrofoam sphere target

The effect of increasing the bandwidth was to strengthen the off-center lobes found at the higher and lower frequencies and hence "fill" the sphere return. Unfortunately at sweeps above about $\pm 10\%$ the frequency response curve of the transducers has decreased such that only a small contribution is obtained from the extreme frequencies of the sweep, hence the full effect of frequency averaging could not be investigated. This is especially evident in the array target data.

6.3.3 Array

Figure 6.8 shows the acoustic images of the 8-element array at three monochromatic frequencies. The images were recorded for several gain settings to show the various amplitude levels of the multiple lobes. As the gain is increased the lower level lobes become evident. Because of the gain level sensitivity and the large number of lobes it is difficult to determine the difference in the lobe structure at different frequencies. Figure 6.9 compares three monochromatic images at approximately the same loop-gain levels, i.e. the receiver gain is set to compensate for the decrease in transducer gain.

Figure 6.10 shows the effect of adding a swept frequency signal of two different sweep widths: ± 100 KHz and ± 50 KHz. As in Figure 6.8, the lobe levels were interrogated by varying the receiver gain. The ± 50 KHz swept signal was inadequate to completely smooth the reradiation pattern, however the ± 100 KHz swept signal provided good smoothing at nearly all intensity levels. It is evident that a greater sweep width is required to completely "fill" the image.



$f = 1500 \text{ KHz}$ $f = 1640 \text{ KHz}$ $f = 1750 \text{ KHz}$
 $G = 36 \text{ db}$ $G = 26 \text{ db}$ $G = 30 \text{ db}$

Figure 6.9 Image of major lobes of 8-element array for three monochromatic frequencies.

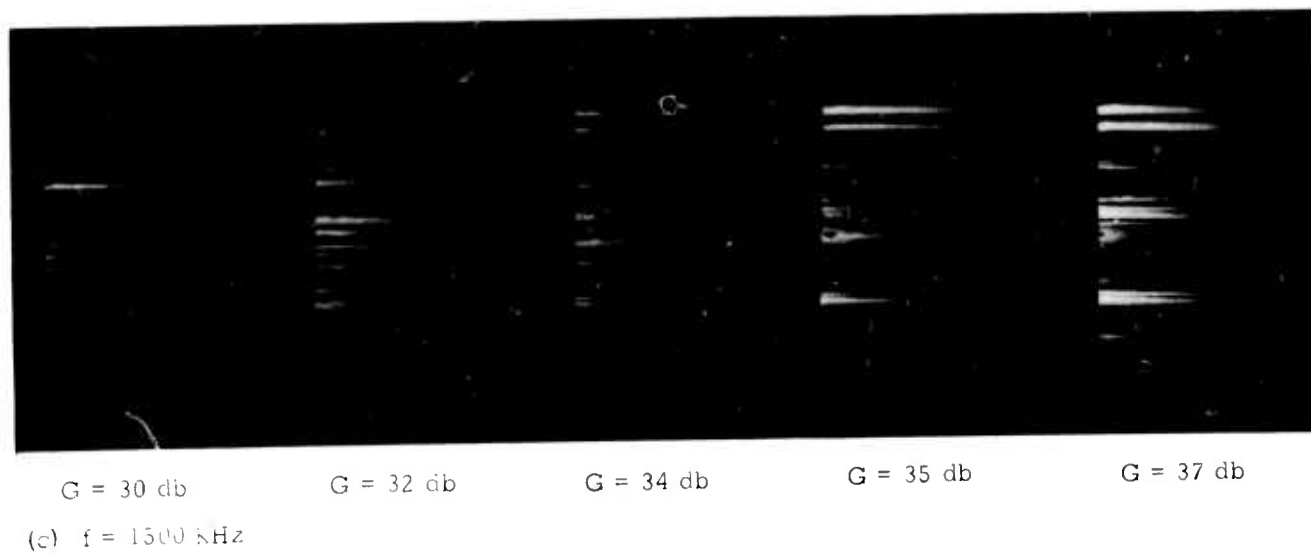
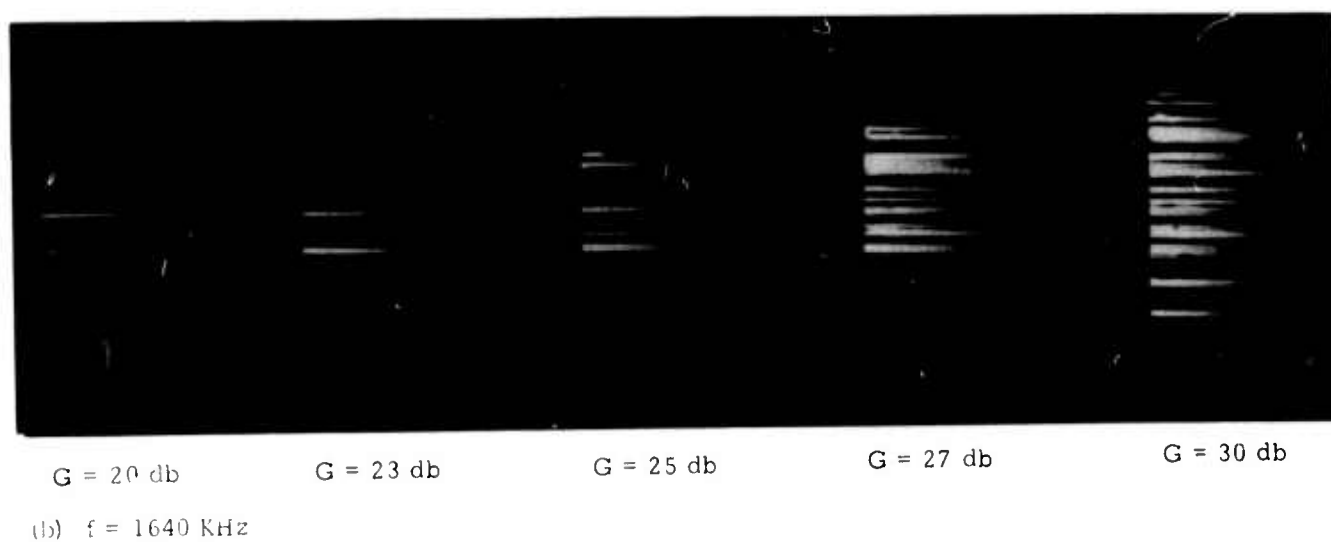
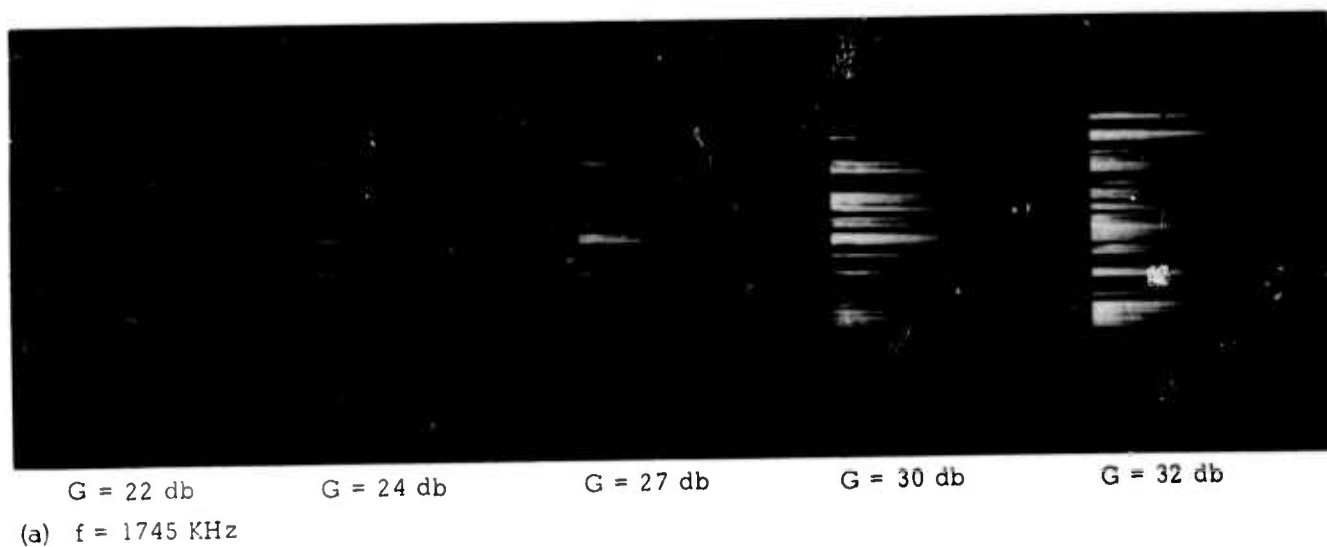


Figure 6.8 Effect of receiver gain variations on images of 8-element array at three monochromatic frequencies



G = 11 db

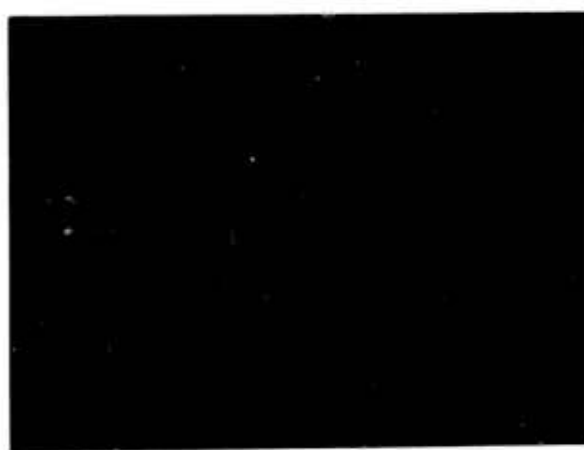
G = 14 db

G = 17 db

G = 20 db

G = 23 db

(a) Frequency = 1640 ± 100 KHz



G = 11 db

G = 14 db

(b) Frequency = 1640 ± 50 KHz

Figure 6.10 Effect of swept frequency on image of 8-element array

CHAPTER 7

CONCLUSIONS

The frequency dependence of a surface of known statistics was measured and compared with the theoretical predicted results of a theory based on the Kirchhoff-Huygen's Principle. The results agree over a limited frequency range, but in general it was concluded that this method does not adequately predict the frequency dependence of backscatter. In addition an imaging experiment was performed employing swept-frequency illumination. The experiment demonstrated the improved target definition obtained by the addition of frequency averaging. It was concluded that a panchromatic system should offer significant advantages over monochromatic systems in applications such as terrain imaging, altimetry, and tracking.

Measurements have been presented for the frequency dependence of the average backscatter power from a surface meeting the conditions of the Kirchhoff method. These results are complemented by measurements of the frequency dependence of the average backscatter power from an extremely rough surface for which the Kirchhoff method is not applicable, but which is indicative of many natural terrain conditions. When the frequency dependence is expressed in terms of the wavelength slope as λ^α , the coefficient α was found to vary between 0 and + 3.7 for the fundamental surface and -2 to 0 for the very rough surface. The measurement frequency range was approximately 6:1. A comparison of the measurements results with the results predicted by the Kirchhoff method was made and agreement was found for some frequency regions. The measurement results indicate a transitional region which cannot be explained by the Kirchhoff method. In addition, the measurements support previous suggestions that the effective statistical parameters of the surface are both angle and frequency dependent, however the nature of this dependence was not determined.

Equipment was designed and constructed to implement transmission

and reception of a broad-spectrum acoustic signal. This equipment incorporates sufficient flexibility to facilitate examination of typical radar system problems, and to determine the effect of broad-spectrum illumination on the reradiation patterns of complex targets. The system was used to measure the decrease in positional fading and the averaging of complex reradiation patterns possible with the incorporation of swept frequency illumination. The technique employed to obtain panchromatic illumination was to transmit frequency samples of a continuous frequency spectrum. Basic backscatter measurements were recorded using a high frequency sampling rate, however to obtain panchromatic images a sample rate of only four samples per sweep was employed. However the sampling was random and hence the full effect of panchromatic illumination was achieved. The use of panchromatic illumination substantially improved the image definition of complex targets.

7.1 Recommendation for Further Work

The experiment resulted in defining problems requiring further work. The most important of these are the following:

- A. The initial concept of measuring backscattered power over a continuous range of frequencies was hampered by the nature of the acoustic transducers available. In addition the frequency dependence of the target did not warrant so fine a frequency sampling. It is obvious that much effort is required before acceptable transducers are available for such experiments, however it does not appear mandatory that they operate broadband. A multiple discrete frequency experiment could provide adequate definition of the frequency dependence of most targets except for conditions to be discussed next.
- B. The measurements effectively covered a frequency range of about 6:1. This range was inadequate to enable an extension of the theory to fit the results. The analysis of the results does confirm the close connection between angle dependence and

frequency dependence of the backscattered power, and each appears to indicate that the effective-parameters concept is appropriate. To determine the validity of the suspected effective-parameter approach or the "size filtering" concept, the frequency range must encompass several transition regions of structure sizes. This may well require deliberately including structure sizes, such as the small sand particles, that violate the conditions of the theory. This is due to the need of including the regions for which the scatterers are approximately the size of the incident wavelength. To illustrate this, note that the frequency dependence curves obtained from the sanded surface did not appear to have reached a transition region which showed the existence of the undulating surface (fundamental surface). The sand particles dominated the return throughout the measured range. To determine the transition regions may require a very close frequency sampling. This realization was the basis of the equipment design, however the restricted frequency range covered did not warrant the capability of the instrument. The eventual availability of a wider range of better transducers may again justify the initial design.

- C. The examination of the Kirchhoff method showed that additional information about the surface statistics needs to be included or at least a new interpretation is required if an accurate prediction of frequency dependence is to be obtained. The present situation, which in essence says that the greater the variance of surface heights the more dominant the small lag distance region of the autocorrelation, is contrary to physical reasoning. Regardless of the correlation distance associated with the surface, the region near the origin of the autocorrelation is dominated by the small structure on the surface. Obviously the small structure does not contribute to the fact that the surface has a large variance, unless the surface is extremely abnormal. Therefore the theory forces the contradiction that the greater the variance (a large structure descriptor) the more im-

portant the small structure becomes in determining the scatter. It is little wonder that authors are lead to contend that the high frequency components of the surface have more influence than the low frequency components. It is suggested that future work on this problem follow the work of Fung and Moore (1964), which was a composite autocorrelation function, but also include variance terms associated with the appropriate subranges of structure sizes.

- D. The use of swept-frequency illumination in image recording of complex object targets and area-extensive targets has tremendous potential both for military and civilian applications. This is subject matter for an extensive research program. The acoustic test facility developed through this dissertation effort offers an ideal means of exploring this research area. However, as has been mentioned repeatedly, the full potential of the system cannot be realized until improved acoustic transducers are developed.

APPENDIX A

GENERAL KIRCHHOFF METHOD

This is a summary review of a general scattering theory based on the physical optics method. The treatment follows that of Beckmann and Spizzichino (1963), and is for scalar waves. The objective is to determine the predicted frequency dependence of backscatter for rough surfaces.

The physical optics, or Kirchhoff, approach has been employed by several authors to determine scattering from both "rough" and "smooth" surfaces. The general approach will be outlined and the backscatter expressions will be obtained for two surfaces with different autocorrelation functions; Gaussian and exponential.

A.1 General Development

The scattering geometry with which we will be concerned is shown in figures 1 and 2.

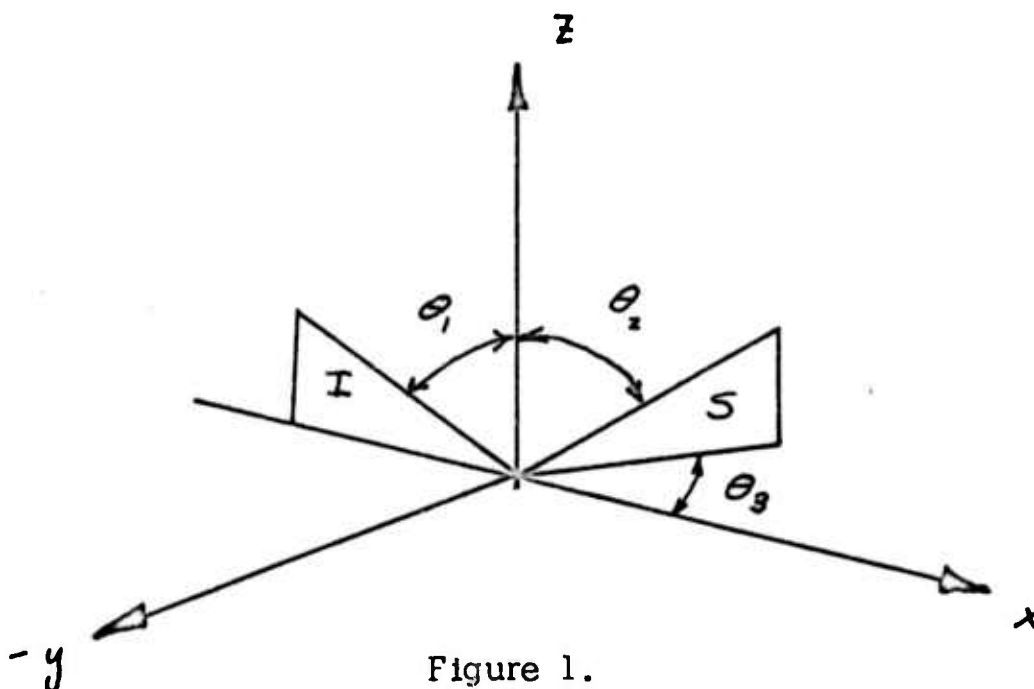


Figure 1.

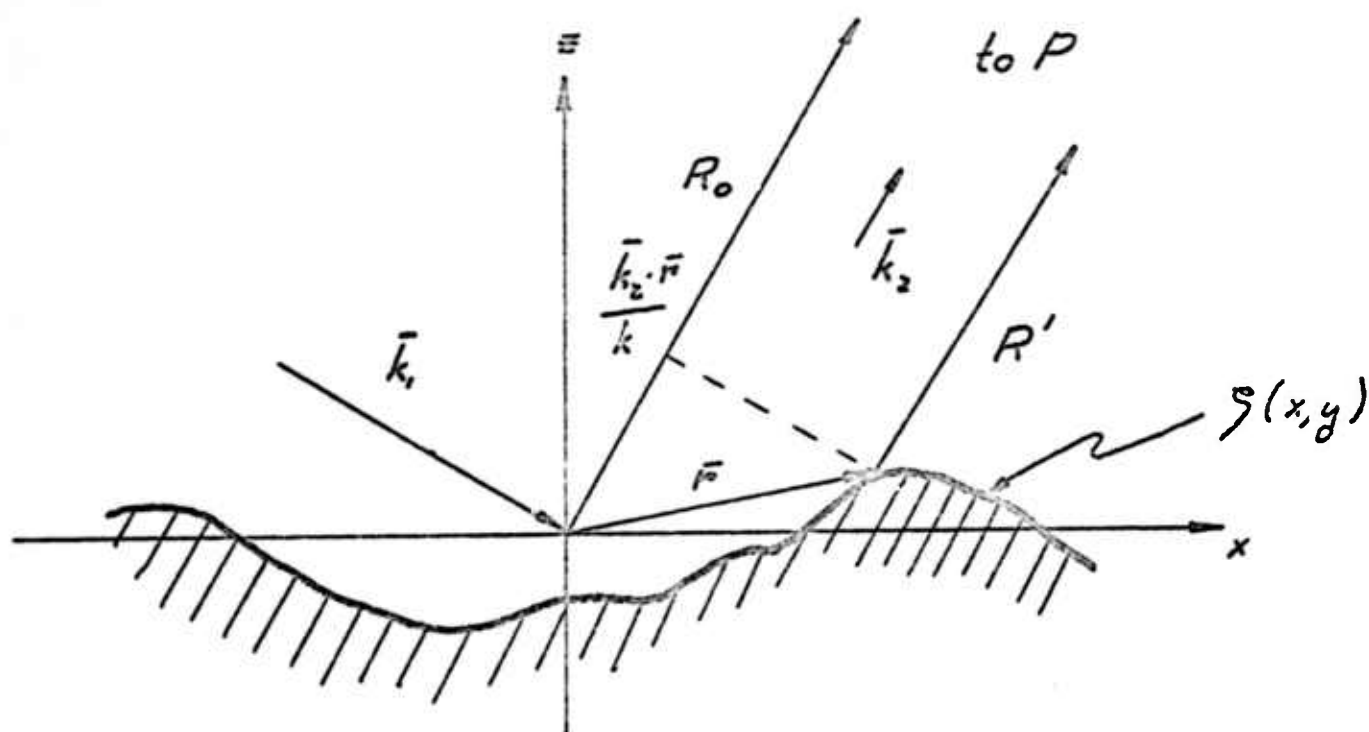


Figure 2.

The scattered field at the observation point P (figure 2) is given by the Helmholtz integral.

$$E_2(P) = \frac{1}{4\pi} \oint \left[E \frac{\partial \psi}{\partial n} - \psi \frac{\partial E}{\partial n} \right] ds \quad (1)$$

where

$$\psi = \frac{e^{jk_2 R'}}{R'}$$

By placing P in the Fraunhofer zone of diffraction, $R' \rightarrow \infty$, then we may rewrite

$$\psi = \frac{e^{jk_z R_0 - j\bar{k}_z \cdot \vec{r}}}{R_0}$$

where R_0 is the distance from P to the origin.

In (1) we are concerned with the values of E and $\partial E/\partial n$ which represent the field and its derivative normal to S . The Kirchhoff or physical optics method consists essentially of approximately the values of E and $\partial E/\partial n$ on S and evaluating (1).

We will now make an assumption which is fundamental to this approach. It is assumed that the field at any point on the surface can be approximated by the field that would be present on the tangent plane at that point.

With this approximation the field on S will be

$$E_s = (1 + R)E, \quad (2)$$

and

$$\left(\frac{\partial E}{\partial n} \right)_s = j(1 - R)E, \bar{k}_1 \cdot \bar{n} \quad (3)$$

where R is the Fresnel reflection coefficient of a smooth plane. Equation (3) follows from (2) by differentiating the incident and reflected waves.

$$E_1 = e^{j\bar{k}_1 \cdot \bar{r} - j\omega t} ; E_2 = R e^{j\bar{k}_2 \cdot \bar{r} - j\omega t}$$

$$E = E_1 + E_2$$

$$\nabla E = j\bar{k}_1 e^{j\bar{k}_1 \cdot \bar{r}} + R j\bar{k}_2 e^{j\bar{k}_2 \cdot \bar{r}}$$

$$\nabla E \cdot \bar{n} = j \left[(\bar{k}_1 \cdot \bar{n}) e^{j\bar{k}_1 \cdot \bar{r}} + R (\bar{k}_2 \cdot \bar{n}) e^{j\bar{k}_2 \cdot \bar{r}} \right]$$

$$\left(\nabla E \cdot \bar{n} \right) = \left(\frac{\partial E}{\partial n} \right)_s = j(1-R) e^{j\bar{k}_1 \cdot \bar{r}} (\bar{k}_1 \cdot \bar{n})$$

note:

$$\bar{k}_1 \cdot \bar{n} = -\bar{k}_2 \cdot \bar{n} \quad (4a) \quad \bar{k}_1 \cdot \bar{r} = \bar{k}_2 \cdot \bar{r} \quad (4b)$$

Employing the notation H_0, E_0 = incident field, H_1, E_1 = transmitted field and H_2, E_2 = reflected field and the boundary conditions:

$$\bar{n} \times (\bar{E}_0 + \bar{E}_2) = \bar{n} \times \bar{E}_1$$

$$\bar{n} \times (\bar{H}_0 + \bar{H}_2) = \bar{n} \times \bar{H}_1$$

then:

$$E_{2\perp} = \frac{\mu_1 k_2 \cos \theta_0 - \mu_2 \sqrt{k_1^2 - k_2^2 \sin^2 \theta_0}}{\mu_1 k_2 \cos \theta_0 + \mu_2 \sqrt{k_1^2 - k_2^2 \sin^2 \theta_0}} E_{0\perp} \quad (5)$$

and

$$H_{2\parallel} = \frac{\mu_2 k_1^2 \cos \theta_0 - \mu_1 k_2 \sqrt{k_1^2 - k_2^2 \sin^2 \theta_0}}{\mu_2 k_1^2 \cos \theta_0 + \mu_1 k_2 \sqrt{k_1^2 - k_2^2 \sin^2 \theta_0}} H_{0\parallel} \quad (6)$$

where θ_0 = angle of incidence of incident wave. Assuming $\mu_1 = \mu_2$, then from (5)

$$R_1 = \frac{\cos \theta_0 - \sqrt{(k_1/k_2)^2 - \sin^2 \theta_0}}{\cos \theta_0 + \sqrt{(k_1/k_2)^2 - \sin^2 \theta_0}}$$

$$k_1 = \frac{2\pi}{\lambda} = \omega \sqrt{\frac{\epsilon_1}{\mu_1}} \quad ; \quad k_2 = \omega \sqrt{\frac{\epsilon_2}{\mu_2}}$$

$$\frac{k_1}{k_2} = \sqrt{\frac{\epsilon_1/\epsilon_2}{\mu_1/\mu_2}} = Y$$

where $\epsilon_2, \mu_2 = \epsilon_0, \mu_0$ i.e. region 2 is free space

$$R_{\perp} = \frac{\cos \theta_0 - \sqrt{Y^2 - \sin^2 \theta_0}}{\cos \theta_0 + \sqrt{Y^2 - \sin^2 \theta_0}} \quad (7)$$

and similarly from (6)

$$R_{\parallel} = \frac{Y^2 \cos \theta_0 - \sqrt{Y^2 - \sin^2 \theta_0}}{Y^2 \cos \theta_0 + \sqrt{Y^2 - \sin^2 \theta_0}} \quad (8)$$

Now returning to figure 2 and using (1), (2) and (3) we compute the scattered field at a point P in the far field.

$$\begin{aligned} E_2(P) &= \frac{1}{4\pi} \oint \left[E \frac{\partial \psi}{\partial n} - \psi \frac{\partial E}{\partial n} \right] ds \\ &= \frac{1}{4\pi} \oint [E \nabla \psi - \psi \nabla E] \cdot \bar{n} ds \\ &= \frac{e^{jkR_0}}{4\pi R_0} \oint [E(-jk_2) - \nabla E] e^{-jk_2 \cdot \bar{r}} \cdot \bar{n} ds \end{aligned}$$

$$E_2(P) = j \frac{e^{jkR_0}}{4\pi R_0} \oint \left[R(\bar{k}_1 - \bar{k}_2) - (\bar{k}_1 + \bar{k}_2) \right] \cdot \bar{n} e^{j(\bar{k}_1 - \bar{k}_2) \cdot \bar{r}} ds$$

$$E_2(P) = j \frac{e^{jkR_0}}{4\pi R_0} \oint \left[R\bar{v} - \bar{p} \right] \cdot \bar{n} e^{j\bar{v} \cdot \bar{r}} ds$$

(9)

from the geometry, figure 3, we can write the unit vector, \bar{n} , as

$$\bar{n} = \frac{-Z_x \bar{a}_x - Z_y \bar{a}_y + \bar{a}_z}{\sqrt{Z_x^2 + Z_y^2 + 1}} \quad (10)$$

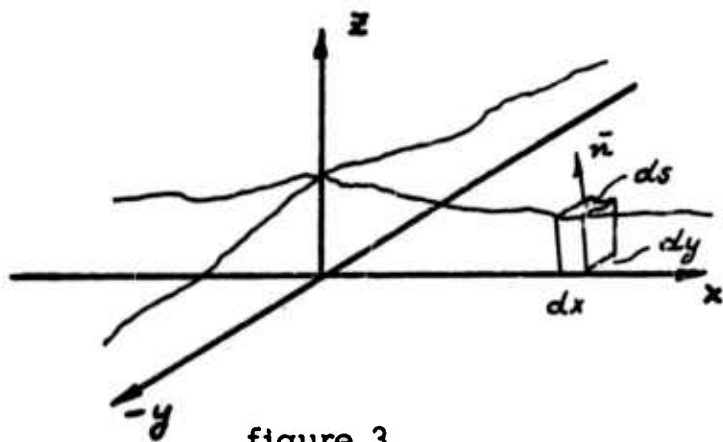


figure 3

where $Z_x = \frac{\partial \zeta(x, y)}{\partial x}$

$Z_y = \frac{\partial \zeta(x, y)}{\partial y}$

The area, ds , can be written as

$$ds = \left[Z_x^2 + Z_y^2 + 1 \right]^{1/2} dx dy \quad (11)$$

The quantity $\left[Z_x^2 + Z_y^2 + 1 \right]^{1/2}$ accounts for the projection of ds into the xy plane. Another, more illustrative, way of writing \bar{n} and ds is as follows:

$$\begin{aligned}\bar{n} &= \bar{a}_x \sin \alpha \cos \beta + \bar{a}_y \sin \beta \cos \alpha + \bar{a}_z \cos \beta \cos \alpha \\ &= \cos \beta \cos \alpha \left[\bar{a}_x \tan \alpha + \bar{a}_y \tan \beta + \bar{a}_z \right]\end{aligned}$$

$$ds = \frac{dx}{\cos \alpha} \frac{dy}{\cos \beta} = \sec \alpha \sec \beta dx dy$$

so

$$\bar{n} ds = \left[\bar{a}_x Z_x + \bar{a}_y Z_y + \bar{a}_z \right] dx dy \quad (12)$$

Substituting (12) into (9)

$$E_2(P) = K \int_A (R\bar{v} - \bar{p}) \cdot (Z_x \bar{a}_x + Z_y \bar{a}_y + \bar{a}_z) e^{j\bar{v} \cdot \bar{r}} dx dy \quad (13)$$

$$\bar{k}_1 = k \sin \theta_1 \bar{a}_x - k \cos \theta_1 \bar{a}_z$$

$$\bar{k}_2 = k \cos \theta_3 \sin \theta_2 \bar{a}_x + k \sin \theta_3 \sin \theta_2 \bar{a}_y + k \cos \theta_2 \bar{a}_z$$

$$\begin{aligned}\bar{v} = \bar{k}_1 - \bar{k}_2 &= k \left[(\sin \theta_1 - \cos \theta_3 \sin \theta_2) \bar{a}_x \right. \\ &\quad \left. - (\sin \theta_3 \sin \theta_2) \bar{a}_y + (-\cos \theta_1 - \cos \theta_2) \bar{a}_z \right]\end{aligned}$$

$$\bar{\rho} = \bar{k}_1 + \bar{k}_2 = k \left[(\sin \theta_1 + \cos \theta_3 \sin \theta_2) \bar{a}_x + (\sin \theta_3 \sin \theta_2) \bar{a}_y + (-\cos \theta_1 + \cos \theta_2) \bar{a}_z \right]$$

$$\begin{aligned} (R\bar{v} - \bar{\rho}) \cdot (\bar{Z}_x \bar{a}_x + \bar{Z}_y \bar{a}_y + \bar{a}_z) = & (R-1) \bar{Z}_x \sin \theta_1 - (R+1) \cos \theta_3 \sin \theta_2 \\ & - (R+1) \sin \theta_3 \sin \theta_2 \bar{Z}_y \\ & - (R-1) \cos \theta_2 - (R+1) \cos \theta_1 \end{aligned}$$

$$E_z(P) = K \int_a (a \bar{Z}_x + b \bar{Z}_y + c) e^{j(\bar{k}_1 - \bar{k}_2) \cdot \bar{r}} dx dy \quad (14)$$

where:

$$\begin{aligned} a &= (R-1) \sin \theta_1 - (R+1) \cos \theta_3 \sin \theta_2 \\ b &= -(R+1) \sin \theta_3 \sin \theta_2 \\ c &= -(R-1) \cos \theta_2 - (R+1) \cos \theta_1 \end{aligned}$$

Assume vertical polarization where $R = +1$ (directly applicable to acoustic waves).

$$\begin{aligned} E_z(P) = j \frac{e^{jkR_0}}{4\pi R_0} \iint_{x,y} \left[-2 \cos \theta_3 \sin \theta_2 \bar{Z}_x \right. \\ \left. - 2 \sin \theta_3 \sin \theta_2 \bar{Z}_y - 2 \cos \theta_1 \right] e^{j(\bar{k}_1 - \bar{k}_2) \cdot \bar{r}} dx dy \quad (15) \end{aligned}$$

Now we will attempt to eliminate the terms \bar{Z}_x and \bar{Z}_y from the integration, (15). Consider the term

$$E_z(P) = K_x \iint \bar{Z}_x e^{j(\bar{k}_1 - \bar{k}_2) \cdot \bar{r}} dx dy$$

write

$$(\bar{k}_1 - \bar{k}_2) \cdot \bar{r} = \bar{v} \cdot \bar{r} = v_x x + v_y y + v_z z$$

where

$$z = Z(x, y) = \zeta(x, y)$$

let

$$u = \int e^{j\nu_x x + j\nu_y y} dy ; du = \int j\nu_y e^{j\nu_x x + j\nu_y y} dy$$

and

$$dv = Z_x e^{j\nu_z z} dx ; v = \frac{e^{j\nu_z Z(x, y)}}{j\nu_z}$$

and integrate by parts

$$E_2(P) = K_x \left\{ \left[\int \frac{e^{j\nu_z Z(x, y)}}{j\nu_z} e^{j\nu_x x + j\nu_y y} dy \right]_{-X}^X - \iint \frac{\nu_x}{\nu_z} e^{j\nu_x x + j\nu_y y + j\nu_z z} dx dy \right\} \quad (16)$$

Consider:

$$\begin{aligned} dv &= Z_x e^{j\nu_z Z(x, y)} dx \\ &= \frac{\partial Z}{\partial x} e^{j\nu_z Z(x, y)} dx \\ v &= \int \frac{\partial Z}{\partial x} e^{j\nu_z Z(x, y)} dx \end{aligned}$$

from the calculus

$$\begin{aligned} \int f da &= \int f(x) a'(x) dx \\ v &= \int e^{j\nu_z z} a'(x) dx = \int e^{j\nu_z Z(x, y)} \frac{\partial Z(x, y)}{\partial x} dx \\ v &= \frac{e^{j\nu_z Z(x, y)}}{j\nu_z} \Big|_X \end{aligned}$$

We now assume that the value of $Z(x,y)$ along the boundary of the area ds is equal to the mean, i.e. zero. This assumption says that the effect of roughness at the "edges" is zero and is reasonable valid if the area is large relative to the illumination area. Using this assumption, the first term on the right in (16) reduces to

$$\begin{aligned} & \frac{K_x}{j\nu_z} \int_{-Y}^Y e^{j\nu_y y} \left[e^{j\nu_x X} - e^{j\nu_x X} \right] dy \\ &= \frac{4}{\nu_x \nu_y} \sin \nu_x X \sin \nu_y Y \end{aligned} \quad (17)$$

Equation (17) is referred to as the "edge effect term" and is generally small enough to be neglected in the subsequent development.

In the same manner that we eliminated Z_x , Z_y can be eliminated and as before a small "edge effect" term is found. The total edge effect is the sum of these two. Now (15) can be written as

$$\begin{aligned} E_2(P) = & -j \frac{e^{jkR_0}}{2\pi R_0} \iint_{XY} \left[-\cos \theta_3 \sin \theta_2 \frac{\nu_x}{\nu_z} \right. \\ & \left. - \sin \theta_3 \sin \theta_2 \frac{\nu_y}{\nu_z} - \cos \theta_2 \right] e^{j(\bar{k}_1 - \bar{k}_2) \cdot \bar{r}} dx dy \end{aligned} \quad (18)$$

where $\nu_x = k(\sin \theta_1 - \cos \theta_3 \sin \theta_2)$

$$\nu_y = -k(\sin \theta_3 \sin \theta_2)$$

$$\nu_z = -k(\cos \theta_1 + \cos \theta_2)$$

so

$$E_2(P) = j \frac{e^{jkR_0}}{2\pi R_0} k \int \frac{(\sin \theta_1 - \cos \theta_3 \sin \theta_2)(\cos \theta_3 \sin \theta_2)}{\cos \theta_1 + \cos \theta_2}$$

$$\begin{aligned}
& + \left[\frac{(\sin \theta_3 \sin \theta_2)(\sin \theta_3 \sin \theta_2)}{\cos \theta_1 + \cos \theta_2} + \cos \theta_2 \right] \\
& \iint_{x, y} e^{j(\bar{k}_1 - \bar{k}_2) \cdot \bar{r}} dx dy \\
E_2(P) = j \frac{e^{jkR_0}}{2\pi R_0} & \left[\frac{1 + \cos \theta_2 \cos \theta_1 - \sin \theta_1 \cos \theta_2 \sin \theta_2}{\cos \theta_1 + \cos \theta_2} \right] \\
& \iint_{x, y} e^{j(\bar{k}_1 - \bar{k}_2) \cdot \bar{r}} dx dy
\end{aligned} \tag{19}$$

for backscatter, $\theta_1 = \theta_2$; $\theta_3 = \pi$, (19) becomes ($R=+1$):

$$E_2(P) = j \frac{e^{jkR_0}}{R_0 \lambda} \iint_{x, y} \frac{e^{j(\bar{k}_1 - \bar{k}_2) \cdot \bar{r}}}{\cos \theta_1} dx dy \tag{20}$$

for $R = -1$, (14) becomes

$$\begin{aligned}
E_2(P) = j \frac{e^{jkR_0}}{4\pi R_0} & \iint \left[-2 \sin \theta_1 z_x + 2 \cos \theta_1 \right] \\
& e^{j(\bar{k}_1 - \bar{k}_2) \cdot \bar{r}} dx dy
\end{aligned} \tag{21}$$

Proceeding with (21) as before

$$E_2(P) = j \frac{e^{jkR_0}}{4\pi R_0} \iint \left[\frac{2 \sin \theta_1 v_x}{v_z} + 2 \cos \theta_1 \right] e^{j(\bar{k}_1 - \bar{k}_2) \cdot \bar{r}} dx dy$$

$$E_2(P) = -j \frac{e^{jkR_0}}{\lambda R_0} \iint_{\bar{x} \bar{y}} \left[\frac{1 + \cos \theta_1 \cos \theta_2 - \cos \theta_3 \sin \theta_2 \sin \theta_1}{\cos \theta_1 + \cos \theta_2} \right] e^{j(\bar{k}_1 - \bar{k}_2) \cdot \bar{r}} dx dy \quad (22)$$

for backscatter, $\theta_1 = \theta_2$; $\theta_3 = \pi$ (22) becomes ($R = -1$):

$$E_2(P) = j \frac{e^{jkR_0}}{\lambda R_0} \iint_{\bar{x} \bar{y}} \frac{e^{j(\bar{k}_1 - \bar{k}_2) \cdot \bar{r}}}{\cos \theta_1} dx dy \quad (23)$$

Regardless of the selection of $R = +1$ or -1 the power calculation will be identical. Therefore the proceeding development does not represent the vector character of the electromagnetic field, but is an appropriate representation of the acoustic waves being considered.

A.2 Random Rough Surface

We will now consider the proceeding as applied to a random rough surface. From (19) we can compute the mean power using the Poynting vector

$$\langle P_2 \rangle = \frac{1}{2} Y_0 \langle E_2 E_2^* \rangle$$

where Y_0 = admittance of free space. The brackets represent the ensemble average of the terms enclosed. The quantity $E_2 E_2^*$ is

$$E_2 E_2^* = F_2 K \iiint_{\bar{x} \bar{y} \bar{x}' \bar{y}'} e^{jv_x(x-x') + jv_y(y-y') + jv_z(z-z')} dx dy dx' dy' \quad (24)$$

where $\bar{v} \cdot \bar{r} = (\bar{k}_1 - \bar{k}_2) \cdot \bar{r}$ has been expressed as

$$\bar{v} \cdot \bar{r} = v_x x + v_y y + v_z z$$

and $z = \zeta(x, y)$.

Recall that it was assumed that $\langle \zeta(x, y) \rangle = 0$. The surface term ζ is the random variable of concern. Equation (24) can now be written in this form of an average as follows.

$$\langle E_2 E_2^* \rangle = F_2 K \iiint_{x, y, \zeta, x', y', \zeta'} e^{j v_x (x-x') + j v_y (y-y') + j v_z (\zeta-\zeta')} \langle e^{j v_z (\zeta-\zeta')} \rangle dx dy dx' dy' \quad (25)$$

We define the distance between the points (x, y) and (x', y') as τ and write (25) in polar coordinates.

$$\langle E_2 E_2^* \rangle = F_2 K \int_0^{2\pi} \int_0^\infty e^{j v_x \tau \cos \phi + j v_y \tau \sin \phi} \langle e^{j v_z (\zeta-\zeta')} \rangle \tau d\tau d\phi \quad (26)$$

Disregarding the limits on τ for now, we note that the integration over ϕ is the zero order Bessel function, so (26) becomes:

$$\langle E_2 E_2^* \rangle = 2\pi F_2 K \int_0^\infty J_0(\tau \sqrt{v_x^2 + v_y^2}) \langle e^{j v_z (\zeta-\zeta')} \rangle \tau d\tau \quad (27)$$

Consider the term $\langle e^{j v_z (\zeta-\zeta')} \rangle$. This average of the function $e^{j v_z (\zeta-\zeta')}$ is

$$\langle e^{j v_z (\zeta-\zeta')} \rangle = \iint_{-\infty}^{\infty} e^{j v_z (\zeta-\zeta')} \rho(\zeta, \zeta') d\zeta d\zeta'$$

which is, by definition (Davenport and Root, p. 52), the joint characteristic function $\chi(jv_z, -jv_z)$. The term $\rho(\zeta, \zeta')$ is the joint probability distribution of the random variables ζ and ζ' . Using the

characteristic function notation, (27) becomes

$$\langle E_2 E_2^* \rangle = 2\pi F_2 K \int_0^\infty J_0(r\sqrt{v_x^2 + v_y^2}) \chi(jv_z, -jv_z) r dr \quad (28)$$

A.3 Normally Distributed Surface

We will consider the normal distribution of surface heights and develop the backscatter power expression to determine the predicted frequency dependence.

The characteristic function associated with the normal distribution is:

$$\chi(v_z) = \exp\left(-\frac{1}{2} \sigma^2 v_z^2\right) \quad (30)$$

where σ^2 = variance of surface heights. The characteristic function associated with the two dimensional distribution is:

$$\chi(v_z, -v_z) = \exp\left[-v_z^2 \sigma^2 (1 - C)\right] \quad (31)$$

where C = autocorrelation function,

T = correlation distance.

Assuming C of a general form e^{-r^2/T^2} and expressing (31) as a series expansion results in the following.

$$\chi(v_z, -v_z) = e^{-v_z^2 \sigma^2} \sum_{m=0}^{\infty} \frac{v_z^{2m} \sigma^{2m}}{m!} e^{-m r^2/T^2} \quad (32)$$

Following Beckmann's notation, we introduce the term $g = (v_z \sigma)^{1/2}$ for convenience.

Substituting (32) into (28) leads to

$$\langle E_2 E_2^* \rangle = 2\pi F_2 K \int_0^\infty J_0(r v_{xy}) \left[e^{-2} \sum_{m=0}^{\infty} \frac{g^m e^{-m r^2/T^2}}{m!} \right] r dr \quad (33)$$

or

$$\langle E_2 E_2^* \rangle = 2\pi F_2 K e^{-g} \sum_{m=1}^{\infty} \frac{g^m}{m!} \int_0^{\infty} J_0(r v_{xy}) e^{-m r^2 / T^2} r dr \quad (34)$$

where

$$v_{xy} = \sqrt{v_x^2 + v_y^2}$$

After integration (34) becomes

$$\langle E_2 E_2^* \rangle = \pi F_2 K e^{-g} T^2 \sum_{m=1}^{\infty} \frac{g^m}{m!} e^{-v_{xy}^2 T^2 / 4m} \quad (35)$$

This result is valid for g less than unity. For $g \gg 1$ (very rough surface) we must use saddle point integration to reduce equation (34). This operation is facilitated by expanding the autocorrelation function $C = e^{-r^2/T^2}$ into a MaClaurin series and truncating the series at two terms, so that (34) reduces to

$$\langle E_2 E_2^* \rangle = \frac{\pi F_2 K T^2}{g} \exp\left(-\frac{v_{xy}^2 T^2}{4g}\right) \quad (36)$$

Summarizing and rewriting (35) and (36) to show the role of the wavelength, λ , we obtain:

Case 1: $g \ll 1$ (slightly rough surface)

$$\begin{aligned} \langle E_2 E_2^* \rangle = & \pi T^2 F_2 K_2 (R_0 \lambda)^{-2} g \exp\left[-2\pi \sigma \lambda^{-1} (\cos \theta_1 + \cos \theta_2)\right]^2 \\ & \times \exp\left[-\pi^2 T^2 \lambda^{-2} (\sin^2 \theta_1 - 2 \sin \theta_1 \sin \theta_2 \cos \theta_3 + \sin^2 \theta_2)\right] \quad (37) \end{aligned}$$

Case 2: $g \gg 1$ (very rough surface)

$$\langle E_2 E_2^* \rangle = \frac{F_2 K_2 T^2}{R_0 4\pi \sigma^2 (\cos \theta_1 + \cos \theta_2)^2} \times \exp \left[\frac{-T^2 (\sin^2 \theta_1 - 2 \sin \theta_1 \sin \theta_2 \cos \theta_3 + \sin^2 \theta_2)}{4 \sigma^2 (\cos \theta_1 + \cos \theta_2)^2} \right] \quad (38)$$

for the case of backscatter, $\theta_1 = \theta_2$; $\theta_3 = \pi$, (37) and (38) become respectively

$$g \ll 1$$

$$\langle E_2 E_2^* \rangle = \frac{32\pi^3 K_2 T^2 \sigma^2}{\lambda^4 R_0^2} \exp \left[-16\pi^2 \sigma^2 \lambda^{-2} \cos^2 \theta_1 \right] \exp \left[-4\pi^2 T^2 \lambda^{-2} \sin^2 \theta_1 \right] \quad (39)$$

$$g \gg 1$$

$$\langle E_2 E_2^* \rangle = \frac{T^2 K_2}{4\pi R_0^2 \sigma^2 \cos^4 \theta_1} \exp \left[-\frac{T^2}{2\sigma^2} \tan^2 \theta_1 \right] \quad (40)$$

A.4 Exponentially Distributed Surface

In this section the treatment of A.3 will be repeated except that the autocorrelation function will be assumed exponential, i.e.

$$C = \exp(-|\tau|/\tau)$$

The characteristic function associated with the two dimensional exponential distribution is:

$$\chi(v_z, -v_z) = \exp \left[-v_z^2 \sigma^2 (1 - e^{-|\tau|/\tau}) \right] \quad (41)$$

which may be written as follows

$$\chi(v_z, -v_z) = e^{-v_z^2 \sigma^2} \sum_{m=0}^{\infty} \frac{v_z^{2m} \sigma^{2m} e^{-m|\tau|/\tau}}{m!} \quad (42)$$

Again incorporating $g = v_z^2 \sigma^2$ and substituting (42) into (28) we obtain

$$\langle E_2 E_2^* \rangle = 2\pi F_2 K \int_0^\infty J_0(\tau v_{xy}) \left[e^{-g} \sum_{m=1}^{\infty} \frac{g^m}{m!} e^{-m|\tau|/T} \right] \tau d\tau \quad (43)$$

or

$$\langle E_2 E_2^* \rangle = 2\pi F_2 K e^{-g} \sum_{m=1}^{\infty} \frac{g^m}{m!} \int_0^\infty J_0(\tau v_{xy}) e^{-m|\tau|/T} \tau d\tau \quad (44)$$

After integration (44) becomes

$$\langle E_2 E_2^* \rangle = 2\pi F_2 K e^{-g} \sum_{m=1}^{\infty} \frac{g^m}{m!} \frac{m T^2}{[m^2 + (T v_{xy})^2]^{3/2}} \quad (45)$$

This result is valid for g less than unity, for $g \gg 1$ (very rough surface) we must again use saddle point integration to reduce equation (44).

Proceeding as in A.3 equation (44) reduces to (Beckmann 1965)

$$\langle E_2 E_2^* \rangle = \frac{2\pi F_2 K g T^2}{[g^2 + (T v_{xy})^2]^{3/2}} \quad (46)$$

Summarizing and rewriting (45) and (46) for the case of backscatter to show the role of the wavelength, λ , we obtain

Case 1: $g \ll 1$ (slightly rough surface)

$$\langle E_2 E_2^* \rangle = \frac{32\pi^3 F_2 K_2 T^2 \sigma^2 \cos^2 \theta_1}{R_0^2 \lambda [\lambda^2 + T^2 / 16\pi^2 \sin^2 \theta_1]^{3/2}} \exp \left[\frac{16\pi^2 \sigma^2 \cos^2 \theta_1}{\lambda^2} \right] \quad (47)$$

Case 2: $g \gg 1$ (very rough surface)

$$\langle E_2 E_2^* \rangle = \frac{F_2 K Q \cos^2 \theta_1}{8\pi R_s^2 [\cos^4 \theta_1 + Q \sin^2 \theta_1]}^{3/2} \quad (48)$$

where

$$Q = \left[\frac{\lambda T}{4\pi\sigma^2} \right]^2$$

APPENDIX B

GENERAL AUTOCORRELATION FUNCTIONS

This is a continuation of the discussions presented in section A.3 and A.4 of Appendix A with an elaboration relevant to the comparison of measured and predicted results presented in section 5.4.

In section 4.3 it was shown that the autocorrelation of the fundamental surface was fit by the Gaussian function for the region away from the origin, and by the following function for the region near the origin.

$$C(\tau) = \exp \left\{ - \left(\frac{\tau}{\tau_1} \right)^{3/2} \right\} \quad (\text{B.1})$$

Substitution of this autocorrelation function into the Kirchhoff expression (equation 2.10) poses considerable difficulty when attempting the integration, therefore the following approach is employed (Fung and Leovaris, 1968). Recall that to obtain (A.39) and (A.40) the autocorrelation function $C(\tau)$ was expanded about $\tau = 0$ and the series was approximated by the first two terms. The first derivative $C'(\tau)$ is necessarily zero since $C(\tau)$ is analytic, hence the autocorrelation function is approximated by

$$C(\tau) = 1 + \frac{C''(0)\tau^2}{2}$$

Consider that instead of expanding about $\tau = 0$, the expansion is made about $\tau = \tau_1$, where τ_1 is the value for which the integrand (equation 2.10) is a maximum. Then for small τ the approximation is

$$C(\tau) = 1 + C'(\tau_1)\tau$$

where $C'(\tau_1)$ is the slope of the autocorrelation function at τ_1 .

Using this approach the equivalent expression to (A.40) is (omitting a constant):

$$\langle P \rangle = Q \left[\cos^4 \theta + Q \sin^2 \theta \right]^{-3/2} \quad (\text{B.2})$$

where

$$Q = \left[\frac{\lambda}{4\pi\sigma^2 C'(\tau_1)} \right]^2$$

Equation (B.2) is identical in form to equation (A.48) obtained for the exponential autocorrelation. However, using (B.2) allows the use of many autocorrelation functions for which equation (2.10) cannot otherwise be readily integrated.

The first derivative of the autocorrelation function in equation (B.1) is

$$C'(\tau_1) = -\frac{3}{2} \left(\frac{\tau_1}{T_s} \right)^{1/2} e^{-\left(\frac{\tau_1}{T} \right)^{3/2}} \quad (\text{B.3})$$

If τ_1 is selected to be a constant, the frequency and angular dependence of (B.2) is identical with that of the exponential autocorrelation shown in section 5.4. Letting τ_1 be the point for which $\tau \exp[-g(1 - C(\tau))]$ in equation (2.10) is maximum leads to values for equation (B.3) as listed in Table B.1, using the profile measurements of the fundamental surface. Figure B.1 shows σ^* versus wavelength using equation (B.2) and the values of $C'(\tau_1)$ shown in Table B.1.

Using this approach, Fung and Leovaris (1968) determined values of Q which provided a reasonable fit to experiment results of angle dependence at five wavelengths. From these values of Q , the slope term, $C'(\tau_1)$ was calculated and was found to compare favorably to the measured slope of the surface autocorrelation. Their work shows that the variation of angular dependence with wavelength is reasonably well predicted by equation B.2. This method is analagous to employing an effective parameter, T/σ^2 , which varies with wavelength. Using the expression assumed in equation 5.3

$$R_e = R f(\theta) \left(\frac{\lambda}{\lambda_0} \right)^{\rho} \quad (5.3)$$

where R_e = effective parameter, $(T/\sigma^2)_e$

R = actual parameter, (T/σ^2)

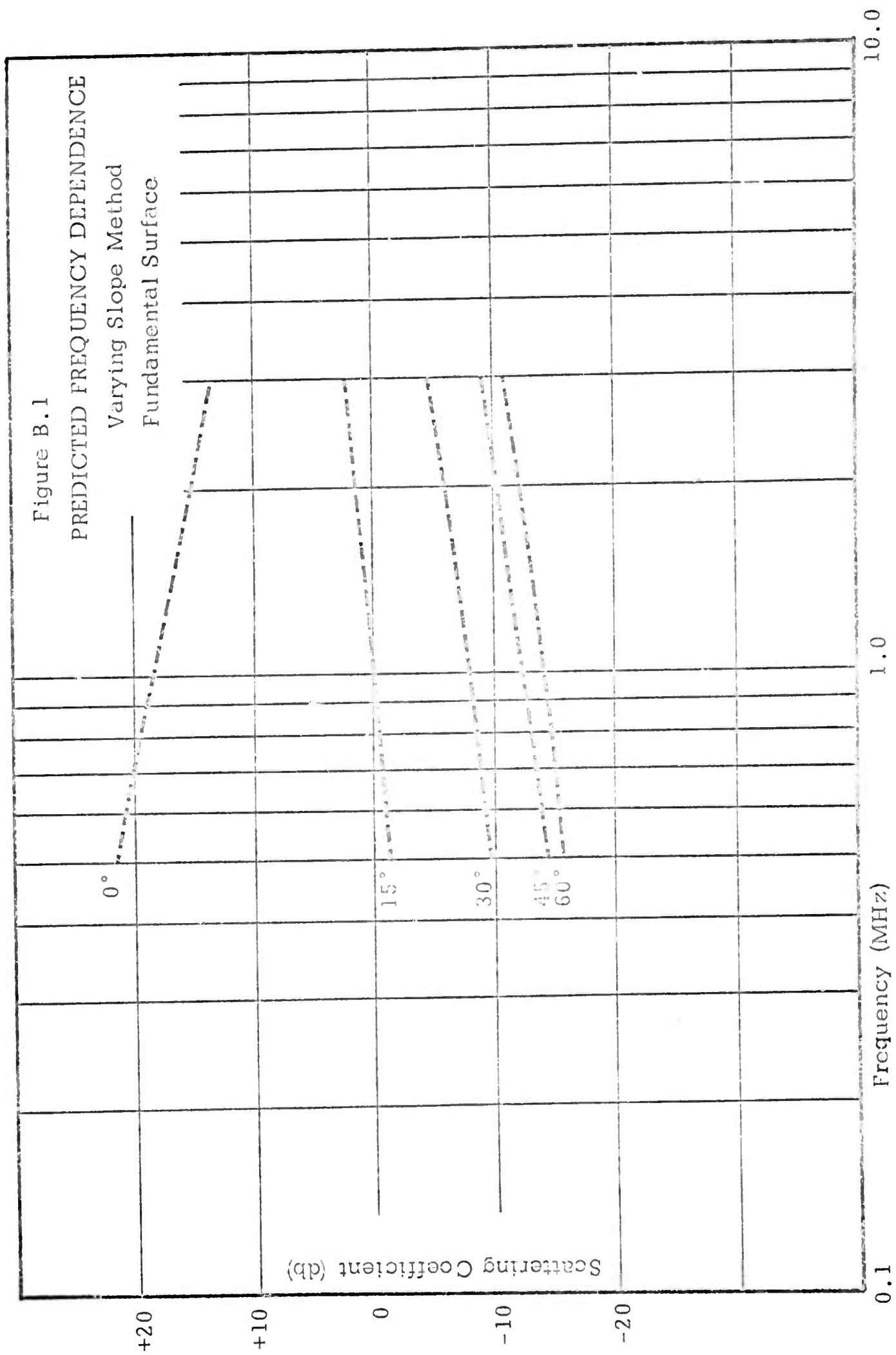
then from Table B.1 the value of ρ is approximately -0.5. This results in a predicted α for 0° incidence of 1.0 which compares with the measured $\alpha = 1.03$ (below 1.25 MHz) and $\alpha = 2.78$ (above 1.25 MHz). The predicted α for 15° and 30° incidence is also in good agreement with the measurements of α below 1.25 MHz. However, the data above 1.25 MHz is not fit by the theory.

TABLE B.1

λ (mm)	Θ (degrees)	τ_1^* (mm)	$C'(\tau_1)$
0.5	0	0.508	-.0080
	15	0.508	-.0080
	30	0.508	-.0080
	45	1.016	-.0113
	60	1.016	-.0113
1.0	0	1.016	-.0113
	15	1.016	-.0113
	30	1.524	-.0138
	45	1.524	-.0138
	60	2.540	-.0175
1.5	0	1.524	-.0138
	15	1.524	-.0138
	30	2.032	-.0158
	45	2.540	-.0175
	60	3.556	-.0203
3.0	0	3.556	-.0203
	15	3.556	-.0203
	30	4.064	-.0215
	45	5.588	-.0243
	60	**	---
4.74	0	6.604	-.0256
	15	7.112	-.0262
	30	9.655	-.0281
	45	**	---
	60	**	---

* These values correspond to the nearest point for which a measurement was recorded.

** The calculated value of τ_1 exceeded a meaningful value.



BIBLIOGRAPHY

- Aksenov, V. I. "Applications of the Kirchhoff Approximation to the Problem of the Scattering from Periodically Rough Surfaces of Finite Conductivity", Radio Eng. & Electronic Phys., Vol. 6, pp. 307-314, 1961.
- Ament, W. S., MacDonald, F. C., and Schewbridge, R. D. "Radar Terrain Reflections for Several Polarizations and Frequencies", Naval Research Laboratory, Unpublished Report, 1959.
- Ayiku, M. N. B., and Moore, R. K. "Acoustic Simulation of Knife Edge Diffraction", Spring Meeting International Scientific Radio Union, 1965.
- Barton, D. K. Radar System Analysis, Prentic-Hall, New Jersey, 1964.
- Bass, F. G. "On the Theory of Combinational Scattering of Waves by a Rough Surface", Izu. Vyssh. Zav. Radiofiz., Vol. 4, pp. 4, 58-66, 1961.
- Beard, C. I. and Katz, I. "The Dependence of Microwave Radio Signal Spectra on Ocean Roughness and Wave Spectra", IRE Trans. AP-5, No. 2, April 1957, p. 183.
- Beckmann, P. "The Depolarization of Electromagnetic Waves by Inclined Planes", Prace Ustavu Radiotech. Elektroniky (Zechoslovakia) no. 19, 17 pp., 1961.
- Beckmann, P. "The Depolarization of Electromagnetic Waves Scattered from Rough Surfaces", Proc. Symp. Electromagnetic Theory and Antennas, E. C. Jordan, Ed., New York, Pergamon, 1963, pp. 717-726.
- Beckmann, P. and Spizzichino, A. The Scattering of Electromagnetic Waves from Rough Surfaces, The MacMillan Co., New York, 1963.
- Beckmann, P. "Scattering by Composite Rough Surfaces", Univ. of Colorado Elec. Engr. Report No. 4, Nov. 1964.
- Beckmann, P. "Scattering by Composite Rough Surfaces", Proc. IEEE, Vol. 53, no. 8, pp. 1012-1015, 1965.
- Beckmann, P. "Shadowing of Random Rough Surfaces", IEEE Trans. Ant. Prop., AP-13, no. 3, pp. 384-388, 1965.

- Beckmann, P. and Lkemperer, W. E. "Interpretation of the Angular Dependence of Backscattering from the Moon and Venus", Radio Sci., Vol. 69D, pp. 1669-1676, December 1965.
- Brande, S. Ya. and F. G. Bass "On the Possibility of Determining the Function of Distribution of Scattering Elements on a Rough Sea Surface by Radar Methods", Izvestiya Vysshikh Uchebnykh Zavedeniy, Radiofizika (USSR), Vol. 1, no. 3, 1610162, 1958. (Trans: LC or SLA 59-206089; OTS 59-13547).
- Birkemier, W. P. and N. W. Wallace "Radar Tracking Accuracy Improvement by Means of Pulse to Pulse Frequency Modulation", IEEE Trans. Communications and Electronics, Jan. 1963, Published in AIEE Trans. (Communications and Electronics), Vol. 18, pp. 571-575, 1962.
- Blackman, R. B. and Tukey, J. W. The Measurement of Power Spectra, Dover Publications, Inc., New York, 1958.
- Brekhovskikh, L. M. "The Diffraction of Waves by a Rough Surface", Part I and II, Zh. Eksper. Teor. Fiz., Vol. 23, pp. 275-304, 1952.
- Brockelman, R. A. and Hagfors, T. "Note on the Effect of Shadowing on the Backscattering of Waves from a Random Rough Surface", IEEE Trans. on Ant. & Prop., Vol. AP-14, no. 5, Sept. 1966.
- Chapman, R. P. and Scott, H. D. "Surface Backscattering Strengths Measured Over an Extended Range of Frequencies and Grazing Angles", J. Acoust. Soc. Amer., Vol. 36, no. 9, pp. 1735-37, Sept. 1964.
- Cosgriff, R. L., Peake, W. H. and Taylor R. C. "Electromagnetic Reflection Properties of Natural Surfaces with Application to Design and Other Sensors", The Ohio State University Antenna Lab., Feb. 1, 1959.
- Cosgriff, R. L., Peake, W. H., and Taylor, R. C. "Terrain Scattering Properties for Sensor System Design", Ohio State Univ. Eng. Expt. Sta. Bull. 29 (3), May 1960.
- Cox, C. "Measurements of Slopes of High-Frequency Wind Waves", J. Marine Research, Vol. 16, no. 3, pp. 199-225, 1958.
- Daniels, F. B. "Radar Determination of the Scattering Properties of the Moon", Nature (6E), Vol. 187, no. 4735, p. 399, July 1960.
- Daniels, F. B. "A Theory of Radar Refraction from the Planets", J. Geophys. Res., Vol. 66(6), 1781-1788, 1961.

- Daniels, F. B. "Radar Determination of the Root Mean Square Slope of the Lunar Surface", J. Geophys. Res., Vol. 68, p. 449, 1963.
- Daniels, F. B. "Radar Determination of the Lunar Slopes: Correction for the Diffuse Component", J. Geophys. Res., Vol. 68, p. 2864, 1963.
- Daniels, F. B. "Radar Reflections from a Rough Moon Described by a Composite Correlation Function", J. Geophys. Res., Vol. 68, no. 23, pp. 6251-54, Dec. 1963.
- Davenport, W. B. and Root, W. L. An Introduction to the Theory of Random Signals and Noise, McGraw-Hill Book Co., Inc., 1958.
- Davies, H. "The Reflection of Electromagnetic Waves from a Rough Surface", Proc. IEEE, Part IV, Vol. 101, pp. 209-214, 1954.
- Davies, H. "The Reflection of Electromagnetic Waves from a Rough Surface", J. Elec. Eng. London, Part 4, Vol. 101, pp. 209-215, 1954.
- Davies, H. "The Reflection of Electromagnetic Waves from a Rough Surface", Proc. IEEE, Part III, Vol. 102, p. 148, 1955.
- Delano, R. "A Theory of Target Glint or Angular Scintillation in Radar Tracking", Proc. IRE, pp. 1778-1784, Dec. 1953.
- De Lorenzo, J. D. and Cassedy, E. S. "A Study of the Mechanism of Sea Surface Scattering", IEEE Trans. on Ant. & Prop., Vol. AP-14, no. 5, Sept. 1966.
- Dellwig, L. F. and Moore, R. K. "The Geologic Value of Simultaneously Produced Like- and Cross-Polarized Imagery", J. Geophys. Research, Vol. 71, pp. 3597, 3601, July 1966.
- Earing, D. G., and Smith, J. A. "Target Signatures Analysis Center: Data Compilation", Institute of Science and Technology, The University of Michigan, July 1966.
- Edison, A. R. "An Acoustic Simulator for Modeling Backscatter of Electromagnetic Waves", Univ. of New Mexico Engr. Exp. Sta. Tech. Report No. EE62, 1961.
- Edison, A. R., Moore, R. K., and Warner, B. D. "Radar Terrain Return Measured at Near-Vertical Incidence", Trans. IRE, Vol. AP-8, pp. 246-254, 1960.

- Edison, A. R. "An Acoustic Simulator for Modeling Backscatter of Electromagnetic Waves", Univ. of New Mexico Engr. Exp. Sta. Tech. Report EE62, April 1961.
- Edison, A. R., Moore, R. K. and Warner, B. D. "High Altitude Radar Simulation Study", Univ. of New Mexico, Engr. Exp. Sta. Tech. Report EE53, April 1961.
- Ellermeier, R. D., Fung, A. K., and Simonett, D. S. "Some Emphirical and Theoretical Interpretations of Multiple Polarization Radar Data", Proc. of the Fourth Symposium on Remote Sensing of the Environment, Univ. of Mich., April 11-14, 1966, Ann Arbor, Mich.
- Evans, J. V. "The Scattering of Radio Waves by the Moon", Proc. Phys. Soc. London, Vol. 70, pp. 1105-1112, 1957.
- Evans, J. V. "Radio-Echo Observations of the Moon at 3.6 cm. Wavelength", Lincoln Lab. MIT, TR-256, 1962.
- Evans, J. V. "Radio Echo Observations of the Moon at 68 cm. Wavelength", Lincoln Lab. MIT, TR-272, 1962.
- Evans, J. V. and Pettengill, G. H. "The Radar Cross-Section of the Moon", J. Geophys. Res., Vol. 68, no. 17, pp. 5098-99, Sept. 1963.
- Evans, J. V. and Pettengill, G. H. "The Scattering Properties of the Lunar Surface at Radio Wave Lengths", Ch. 5 of The Moon, Meteorites and Coments, eidted by Middlehurst and Kuiper, pp. 129-164, University of Chicago Press, 1963.
- Evans, J. V. and Pettengill, G. H. "The Scattering Behavior of the Moon at Wavelengths of 3.6, 68 and 784 centimeters", J. Geophys. Res., Vol. 68 (2), pp. 423-447, 1963.
- Fung, A. K. "Theory of Radar Scatter from Rough Surfaces, Bistatic and Monostatic, with Application to Lunar Radar Return", J. Geophys. Res., Vol. 69, no. 6, pp. 1063-1073, March 1964.
- Fung, A. K. and Moore, R. K. "Effects of Structure Size on Moon and Earth Radar Returns at Various Angles", J. Geophys. Res., Vol. 69 (6), pp. 1075-1081, 1964.
- Fung, A. K. "Scattering and Depolarization of EM Waves from a Rough Surface", Proc. IEEE (Communications), Vol. 54, pp. 395-396, March 1966.

- Fung, A. K. "Scattering Theories and Radar Returns", (Ph. D. Thesis) CRES Report 48-3, University of Kansas, May 1966.
- Fung, A. K. and Moore, R. K. "The Correlation Function in Kirchhoff's Method of Solution of Scattering of Waves from Statistically Rough Surfaces", Journal of Geophys. Res., Vol. 71, no. 12, June 15, 1966.
- Fung, A. K. "Rough Surface Scattering and Its Application to Earth and Moon Radar Returns", CRES Tech. Report 105-1, University of Kansas, Jan. 1967.
- Fung, A. K. and Leovaris A. "Frequency Dependence of Ultrasonic Scatter from Statistically Known Rough Surfaces", WESCON 1968.
- Fung, A. K. "Frequency Dependence of Waves Scattered from Rough Surfaces", CRES Report No. 48-6, University of Kansas, December 1965.
- Goldstein, H. "The Frequency Dependence of Radar Echoes from the Surface of the Sea", Phys. Rev., Vol. 70, pp. 838-846, 1946.
- Grant, C. R., Yaplee, B. S. "Back Scattering from Water and Land at Centimeter and Millimeter Wavelengths", Proc. IRE, Vol. 45, July 1957, pp. 976-982.
- Gustafson, B. G. and Ås, B-O. "System Properties of Jumping Frequency Radar", Phillips Telecommun. Rev., Vol. 25, no. 1, pp. 70-76, July 1964.
- Hagfors, T. "Some Properties of Radio Waves Reflected from the Moon and Their Relation to the Lunar Surface", J. Geophys. Res., Vol. 66, no. 3, pp. 777-85, March 1961.
- Hagfors, T. "Backscatter from an Undulating Surface with Applications to Radar Returns from the Moon", J. Geophys. Res., Vol. 69, pp. 3779-784, 1964.
- Hagfors, T. "Relationship of Geometric Optics and Autocorrelation Approaches to the Analysis of Lunar and Planetary Radar Echoes", J. Geophys. Res., Vol. 71 (2), pp. 3790-383, 1966.
- Hayre, H. S. and Moore, R. K. "Theoretical Scattering Coefficient for Near Vertical Incidence from Contour Maps", J. Res. NBS, Vol. 65D, pp. 427-432, 1961.
- Hayre, H. S. "Lunar Backscatter Theories", Ph.D. Thesis, University of New Mexico, 1962.

- Hayre, H. S. "Surface Roughness of the Moon", Brit. Interplanetary Soc. J., Vol. 18, pp. 389-91, July-Aug. 1962.
- Hayre, H. S. "Statistical Radar Estimate of the Lunar Surface Roughness", J. Franklin Inst., Vol. 277, pp. 197-205, March 1964.
- Janza, F. J., Moore, R. K. and Warner, B. D. "Radar Cross Section of Terrain Near Vertical Incidence at 415 Mc, 3800 Mc and Extension of Analysis to X-band", Trans. 1959 Symposium on Radar Return at Univ. of New Mexico.
- Janza, F. J. "The Analysis of a Pulse Radar Acquisition System and a Comparison of Analytical Models for Describing Sand and Water Radar Return Phenomena", Sandia Corp., SCR 533, Jan. 1963.
- Katz, I. and Spetner, L. M. "Polarization and Depression-Angle Dependence of Radar Terrain Return", Journal of Research of the Nat. Bur. Stand. D. Radio Propagation, Vol. 64D, no. 5, Sept.-Oct. 1960.
- Katz, I. and Spetner, L. M. "A Polychromatic Radar", The Johns Hopkins University, Applied Physics Laboratory, CF 2898, Oct. 24, 1960.
- Katz, I. and Spetner, L. M. "Two Statistical Models for Radar Terrain Return", IEEE Trans. on Antennas and Propagation, Vol. AP-8, no. 3, May 1960.
- Katz, I. "Radar Reflectivity of the Earth's Surface", APL Technical Digest, Jan.-Feb. 1963.
- Katz, I. "Ocean Wave Measurements", APL Technical Digest, Vol. 4, no. 1, Sept.-Oct. 1964.
- Katz, I. "Wavelength Dependence of the Radar Reflectivity of the Earth and the Moon", J. Geo. Res., Vol. 71, no. 2, Jan. 15, 1966.
- Katzin, M. "On the Mechanisms of Sea Clutter", Proc. IRE, Vol. 45, pp. 45-54, 1957.
- Katzin, M. "Sea Clutter at High Depression Angles with Application to the Ground Clutter Problem", 1959 Radar Return Symposium, U.S. Naval Ord. Test Sta. and Univ. of New Mexico Engr. Test Sta., May 1959.
- Kerr, D. E. Propagation of Short Radio Waves, M.I.T. Radiation Laboratory Series (McGraw-Hill, New York), 1951.

- Koepsel, W. W. and Ahmed, N. "Radar Cross Section of a Geometric Shape Using Acoustic Simulation", U. of New Mexico Engr. Exp. Sta. Tech. Report EE80, 1962.
- Kosowsky, L. H., Brody, S. S., Chanzit, L. and Saslovsky, S. "The Reduction of Angle-of-Arival Scintillation by a Frequency Shifting Technique", Presented at the 1963 Natl. Electronics Conf., New York.
- Lapin, A. D. "Sound Scattering at a Rough Solid Surface", Soviet Physics-Acoustics, Vol. 10, no. 1, p. 58, July 1954.
- Long, M. W., Wetherington, R. D., Edwards, J. L., and Abeling, A. B. "Wavelength Dependence of Sea Echo", Georgia Institute of Technology, Atlanta, Final Report, Project A-840, Contract N622693019, July 15, 1965.
- Long, M. W. "On the Polarization and the Wavelength Dependence of Sea Echo", IEEE Trans. Antennas and Propagation, Vol. AP-13, pp. 749-754, Sept. 1965.
- Lundien, J. R. "Terrain Analysis by Electromagnetic Means", U.S. Army Engineer Waterways Experiment Station Technical Report No. 3-693, September 1966.
- Lynn, V. L., Sohigian, M. D. and Crocker, E. A. "Radar Observations of the Moon at a Wavelength of 8.6 millimeters", J. Geophys. Res., 1964.
- MacDonald, H. C., Brennan, P. A. and Dellwig, L. F. "Geologic Evaluation by Radar of NASA Sedimentary Test Site", IEEE Trans. Geoscience Electronics, Vol. GE-5, no. 3, pp. 72-78, December 1967.
- Middleton, D. Statistical Communication Theory, McGraw-Hill Book Co., New York and London, 1960.
- Moore, R. K. and Williams, C. S., Jr. "Radar Return at Near-Vertical Incidence", Proc. IRE, Vol. 45, pp. 228-238, Feb. 1957.
- Moore, R. K. "Resolution of Vertical Incidence Radar Return into Random and Specular Components", Univ. of New Mexico, Albuquerque, Engr. Exp. Sta. Tech. Report EE6, July 1957.
- Moore, R. K. "Acoustic Simulation of Radar Return", Microwaves, Vol. 1, pp. 20-25, 1962.

- Moore, R. K. and Pierson, W. J. "Measuring Sea State and Estimating Surface Winds from a Polar Orbiting Satellite", Intl. Symp. on Electromagnetic Sensing of the Earth from Satellites, Nov. 1965.
- Moore, R. K. "Radar as a Remote Sensor", CRES Tech. Report 61-7, University of Kansas, Jan. 1966.
- Moore, R. K. "Radar Scatterometry--An Active Remote Sensing Tool", Proc. of the Fourth Symp. on Remote Sensing of the Environment, Univ. of Mich., April 11-14, 1966, Ann Arbor, Mich.
- Moore, R. K. and Parkins, B. E. "Omnidirectional Scattering of Acoustic Waves from Rough Surfaces of Known Statistics", J. of Acoustic Soc. of America, no. 1, pp. 170-175, July 1966.
- Morain, S. A. and Simonett, D. S. "K-Band Radar in Vegetation Mapping", Photogrammetric Eng., Vol. 33, no. 7, pp. 730-740, July 1967.
- Muchmore, R. B. "Aircraft Scintillation Spectra", IRE Trans. Antennas and Propagation, Vol. AP-8, pp. 201-212, March 1960.
- Parkins, B. E. "The Omnidirectional Scattering of Acoustic Waves from Rough Surfaces with Application to Electromagnetic Scattering", (Ph.D. Thesis), CRES Report 48-4, University of Kansas, July 1966.
- Peake, W. H. "Interaction of Electromagnetic Radiation with Some Natural Surfaces", Ohio State Univ. Report No. 898-2, May 30, 1958.
- Peake, W. H. "Theory of Radar Return from Terrain", IRE National Convention Record, Pt. 1, on Antennas and Propagation, 1959.
- Peake, W. H. "Interaction of Electromagnetic Waves with Some Natural Surfaces", IRE Trans. on Antennas and Propagation (Special Supplement), Vol. AP-7, pp. 5324-5329, Dec. 1959.
- Pierson, W. J., Scheps, B. B. and Simonett, D. S. "Some Applications of Radar Return Data to the Study of Terrestrial and Oceanic Phenomena", (CRES Tech. Report 61-3) Proc. of the Third Goddard Mem. Symp. on Scientific Exp. for Manned Orbital Flights, Mar. 18-19, 1965, Washington, D. C.
- Ray, M. "Improving Radar Range and Angle Detection with Frequency Agility", Microwave J., pp. 63-68, May 1966.
- Rayleigh, L. D. The Theory of Sound, 3rd Ed., MacMillan, London, 1968.

- Rice, S. O. "Reflection of Electromagnetic Waves from Slightly Rough Surfaces", Comm. Pure and Appl. Math., Vol. 4, p. 351, 1951.
- Rouse, J. W., Jr., Waite, W. P. and Walters, R. L. "Use of Orbital Radars for Geoscience Investigations", Proc. of the Third Space Congress, March 7-9, 1966, Cocoa Beach, Fla.
- Schooly, A. H. "Evaluation of Sea Clutter", Tele-Tech., Vol. 14, no. 3, p. 70, March 1955.
- Semyonov, B. I. "Approximate Computation of Scattering of Electromagnetic Waves by Rough Surface Contours", (trans.) Radio Engrg. and Electronic Physics, Vol. 11, no. 8, pp. 1179-1187, 1966.
- Silver, S. Microwave Antenna Theory and Design, Boston Technical Publisher, 1964.
- Simonett, D. S. "Future and Present Needs of Remote Sensing in Geography", Proc. of the Fourth Symp. on Remote Sensing of the Environment, Univ. of Mich., April 11-14, 1966, Ann Arbor, Mich.
- Skolnik, M. I. Introduction to Radar Systems, McGraw-Hill, New York, 1962.
- Spetner, L. M. "Further Analysis of Radar Terrain Return", Johns Hopkins University #AD-654 333, Nov. 10, 1959, Processed for Defense Documentation Center, Defense Supply Agency.
- Spetner, L. M. "A Statistical Model for Forward Scattering of Waves of a Rough Surface", Trans. IRE AP-6, pp. 88-94, 1958.
- Spetner, L. M. "Radar Terrain Return: A Theoretical Approach", Johns Hopkins University Report No. AD-654 408, May 20, 1959, Processed for Defense Documentation Center, Defense Supply Agency.
- Stratton, J. A. Electromagnetic Theory, McGraw-Hill, New York, 1941.
- Taylor, R. C. "Terrain Return Measurements at X, K_u , and K_a Band", IRE Convention Record Part I, Vol. 7, 1959.
- Taylor, R. C. "The Terrain Scattering Problem", Radar Reflectivity Meas. Symp., Rome Air Develop. Ctr. Report RADC-TDR-64-24, April 1964.

- Valenzuela, Gaspar R. "Depolarization of EM Waves by Slightly Rough Surfaces", IEEE Trans. on Ant. and Prop., Vol. AP-15, no. 4, July 1967.
- Van de Pol, B. "Some Observation on Rayleigh Fading", Tijdschr. Ned. Radiogenoot., Vol. 19, Sept. 1954, pp. 223-229. In English.
- Warner, B. D., Moore, R. K. and Edison, A. R. "Acoustic Simulation of Radar Altimeter Signals from Cities", Univ. of New Mexico Eng. Exp. Sta. Tech. Report EE77, 1962.
- Watson, W. H. "The Scattering of Electromagnetic Waves by Conductors of Linear Extent Comparable with the Wavelength", IEEE Trans. on Antennas and Propagation (Communications), Vol. AP-12, pp. 374-75, May 1964.
- Wiltse, J. C., Schlesinger, S. P. and Johnson, C. M. "Backscattering Characteristics of the Sea in the Region from 10 to 50 K mc/s", Proc. IRE, Vol. 45, pp. 220-228, Feb. 1957.
- Wright, J. W. "Backscattering from Capillary Waves with Application to Sea Clutter", IEEE Trans. Antennas and Propagation, Vol. AP-14, pp. 749-754, Nov. 1966.
- Yaplee, B. S., Bruton, R. H., Craig, K. J. and Roman, N. G. "Radar Echoes from the Moon at the Wavelength of 10 cm", Proc. IRE, Vol. 46, pp. 293-297, 1958.
- Yaplee, B. S., Roman, N. B., Craig, K. S. and Scanlan, T. F. "A Lunar Radar Study at 10 cm. Wavelength", Paris Symposium on Radio Astronomy, Stanford Univ. Press, 1959.

Unclassified

Security Classification

DOCUMENT CONTROL DATA - R & D

(Security classification of title, body of abstract and indexing annotation must be entered when the overall report is classified)

1. ORIGINATING ACTIVITY (Corporate author)

Center for Research, Inc.
The University of Kansas

2a. REPORT SECURITY CLASSIFICATION

Unclassified

2b. GROUP

3. REPORT TITLE

The Frequency Dependence of Backscatter from Rough Surfaces - An Experiment with Broad-Spectrum Acoustic Waves

4. DESCRIPTIVE NOTES (Type of report and inclusive dates)

Type II Special Interim Technical Report

5. AUTHOR(S) (First name, middle initial, last name)

John W. Pouse, Jr.

6. REPORT DATE

September 1, 1968

7a. TOTAL NO. OF PAGES

147

7b. NO. OF REFS

8a. CONTRACT OR GRANT NO.

DAAK02-68-C-0089

9a. ORIGINATOR'S REPORT NUMBER(S)

133-4

b. ARPA Order No. 1079

9b. OTHER REPORT NO(S) (Any other numbers that may be assigned this report)

Supported in part by NASA Contract NAS 9-7175 and NSF Grant GK 1153.

10. DISTRIBUTION STATEMENT

No limitation

11. SUPPLEMENTARY NOTES

Funded by DOD Project Themis
under ARPA Order No. 1079

12. SPONSORING MILITARY ACTIVITY

Monitoring
U.S. Army Engineering Topographic Labs.
Geographic Information Systems Branch
Geographic System Division
Ft. Belvoir, Virginia

13. ABSTRACT

The report describes use of a broad-spectrum acoustic simulation system to predict the behavior of broad-spectrum radar systems. Analysis of the rough-surface backscatter data verifies the predicted dependence of the frequency response of backscatter on the statistics of the illuminated surface. The measurement of the backscatter from object targets confirms the ability of broad-spectrum illumination to smooth the complex reradiation patterns characteristic of object targets. These data are collected in image form (B-scan), and this system capability offers considerable promise for further investigation of imaging radar applications of the broad-spectrum technique.

DD FORM 1473
1 NOV 65REPLACES DD FORM 1473, 1 JAN 64, WHICH IS
OBSOLETE FOR ARMY USE.

Unclassified

Security Classification